THE DECOMPOSITION OF DUSTY GALAXY SPECTRAL ENERGY DISTRIBUTIONS

A Dissertation

Presented to the Faculty of the Graduate School

of Cornell University

in Partial Fulfillment of the Requirements for the Degree of

Doctor of Philosophy

by

Jason A. Marshall

August 2007

THE DECOMPOSITION OF DUSTY GALAXY

SPECTRAL ENERGY DISTRIBUTIONS

Jason A. Marshall, Ph.D.

Cornell University 2007

This thesis presents a new multi-component spectral energy distribution (SED) decomposition method for analyzing the ultraviolet to millimeter wavelength SEDs of dusty infrared-luminous galaxies. SEDs are constructed from spectroscopic and photometric data obtained with the *Spitzer Space Telescope* in conjunction with photometry from the literature. Each SED is decomposed into emission from populations of stars, an AGN accretion disk, PAH molecules, atomic and molecular lines, and distributions of graphite and silicate grains. Decompositions of the SEDs of ∼20 template starburst galaxies and ∼10 template AGNs provide baseline properties to aid in quantifying the star-formation and accretion contributions in composite sources. As case studies, we show that obscured radiation from stars is capable of powering the total dust emission from the composite galaxy NGC 6240, while the decomposition of Mrk 1014 is consistent with ∼65% of its power emerging from an AGN and ∼35% from star-formation. The properties of our template starburst galaxies and AGNs are used to estimate the AGN-strengths for some of our ∼75 ULIRGs, although many are so obscured that uncovering their principal energy source is not possible in the infrared, and instead will require dust penetrating X-ray observations. We suggest that many of the variations in the SEDs of starburst galaxies may be explained in terms of the different mean optical depths through the clouds of dust surrounding the young stars within each. We also suggest that the divergent far-IR properties of AGNs may result from

differences in the relative orientation of their host galaxy and AGN accretion disks, resulting in different amounts of AGN-heated cold dust emission emerging from their host galaxies. We estimate that 30–50% of the far-IR and PAH emission from Mrk 1014 may originate from such AGN-heated material in its host galaxy disk, demonstrating that caution must be used when estimating the strength of star-formation based solely upon the far-IR or PAH properties of a source.

BIOGRAPHICAL SKETCH

Jason Marshall grew up along the scenic beaches of the central coast of California. He began attending the University of California, Los Angeles in the Fall of 1995, and received his B.S. in Astrophysics in December of 1999. Along the way, Jason met Shannon, whom he married in September of 2000. In July of 2001, they moved to Ithaca, New York, where Jason began graduate school at Cornell University in September of that year. Jason completed his M.S. in Astronomy in January of 2006, and his Ph.D. in August of 2007.

ACKNOWLEDGEMENTS

I would like to thank the collaborators I've had over the past several years who have provided invaluable guidance, both scientific and otherwise, and financial assistance during the completion of this dissertation. Of particular note, my gratitude is extended to Lee Armus, Henrik Spoon, Vassilis Charmandaris, Vandana Desai, Jeronimo Bernard-Salas, Jim Houck, my adviser Terry Herter, and the IRS team at Cornell. This work is based [in part] on observations made with the Spitzer Space Telescope, which is operated by the Jet Propulsion Laboratory, California Institute of Technology under NASA contract 1407. Support for this work was provided by NASA through Contract Number 1257184 issued by JPL/Caltech. This research has made use of the NASA/IPAC Extragalactic Database (NED) which is operated by the Jet Propulsion Laboratory, California Institute of Technology, under contract with the National Aeronautics and Space Administration.

TABLE OF CONTENTS

LIST OF TABLES

LIST OF FIGURES

PREFACE

In the Dutch tradition of the "nederlandse samenvatting" *to end a dissertation with a chapter describing the work for the general public, I here begin my dissertation with such a "Summary in English," adapted from a piece I wrote for the Summer 2007 Cornell Astronomy Department Newsletter:*

The universe is a very dusty place.

In reality, this statement is a bit disingenuous since most of it is actually near-vacuum. In fact, if you traveled to a random spot between typical galaxies and collected all the matter in an Earth-sized volume, you would have enough hydrogen atoms to produce about a quarter teaspoon of water. So I should have probably began by stating that the universe is a very empty place. But emptiness is rather boring to talk about, so we'll instead ask: How dusty are the dusty parts of the universe? If you took a box and filled it with the typical mixture of gas and dust found in interstellar space, the gas in the box would outweigh the dust by something like 124 to 1. In other words, if the box weighed as much as $31 in quarters, the dust in the box would weigh only as much as a single quarter. That's not a lot of dust, but it's enough to have a profound effect on the universe.

Before we get to these profundities, you may be wondering if all this dust is similar to the stuff gathering on top of your refrigerator? The answer is yes...and no. Household "dust" is made up of many things like pollen, mold, pet hair, decomposing insects, mite excrement, human skin, and of course dirt. Obviously most of these don't appear in astronomical dust, but a few things found in terrestrial dirt actually do. Typical dirt contains lots of silicates, which are minerals composed mainly of oxygen and silicon. Silicates are abundant throughout the

universe and are observed to make up around 50% of all astronomical dust grains. The other 50% of grains are carbonaceous—composed primarily of carbon and hydrogen—and are similar to particles found in soot and car exhaust. The origin of astronomical dust is not all that well understood, but it's believed that grains form in the cool atmospheres of giant stars.

Until fairly recently, dust was much more of a nuisance to astronomers than anything else. Although there's a lot less dust than gas, dust is so efficient at absorbing visible light that many stars and galaxies are completely obscured by it—similar to the opaque walls of dust in terrestrial sandstorms. This obscuration is called "extinction" by astronomers, and has been the origin of much frustration and confusion. In the late 18th century, William Herschel attempted to ascertain our position in the cosmos by dividing the sky into regions and counting the number of stars in each. After completing his survey, he reasoned that the region with the highest concentration of stars must be in the direction towards the center of the cosmos. Seeing no such concentration, Herschel concluded that we must therefore be located at the center! This was assumed to be true until the discovery of extinction by Robert Trumpler in the 1930s. Just as someone near the edge of a sandstorm who can't see out of it might erroneously conclude that they are at its center, an earth-bound observer might also conclude that they are at the center of the cosmos since extinction completely obscures the center of the galaxy.

Over the past several decades, dramatic improvements in infrared observatories have led to a renaissance in studies of all things dusty. Since dust absorbs infrared light very weakly compared to optical and ultraviolet photons, some sources that are completely obscured at shorter wavelengths can be seen when observed in the infrared. Additionally, obscuring dust is heated to temperatures near room tem-

perature by the absorption of photons, and subsequently emits radiation of its own in the infrared. A particularly powerful new facility has been presented to the world with the *Spitzer Space Telescope*, which includes as part of its instrument package the Infrared Spectrograph (IRS) built at Cornell. The IRS allows astronomers not only to peer into the hearts of enshrouded sources, but also to spectroscopically measure the strength of spectral lines from various atoms, and to discern the chemical composition, temperature, luminosity, and mass of dust within these sources.

I have spent the past several years using the IRS to study dusty galaxies. These galaxies are formed when two individual galaxies merge, and large quantities of gas and dust from each are driven towards the merged nascent nucleus. Since gas is the fuel from which new stars are created, the very dense concentrations of gas within the hearts of dusty galaxies give rise to massive bursts of star-formation called "starbursts." Additionally, most galaxies harbor supermassive black holes (typically one-million to one-billion times as massive as the Sun) at their centers. Much of the copious gas and dust funneled into the nucleus of a merged galaxy may accrete onto its supermassive black hole, giving rise to an active galactic nucleus (or AGN). Complicating matters considerably is the fact that in many of these galaxies, the dust mixed with the fueling gas completely obscures the optical light from newly formed stars and supermassive black hole accretion disks, making it incredibly difficult to figure out what is going on within their hearts.

A major quest in extragalactic astronomy has therefore been to determine whether the majority of the power emitted by dusty galaxies is fueled by starbursts or by AGNs. Towards this goal, I've written software to analyze the spectra obtained with the IRS in an effort to figure out what types of dust are present in

the spectra of pure starburst galaxies and AGNs. We then look to see if similar types of dust are also present in the spectra of the dusty galaxies whose nature we're trying to determine. If an unclassified dusty galaxy has properties similar to those of a pure starburst galaxy, then we can be fairly confident it is powered by star-formation. Similarly, if the dusty galaxy has properties similar to AGNs, then we can infer that it is powered mostly by accretion onto a supermassive black hole. In the end what I'm really doing is putting together a big jigsaw puzzle. The spectra of emission from dust grains near starbursts and AGNs are my puzzle pieces, and the border of the puzzle is given by the IRS spectra. My job is to figure out where all the pieces go and, hopefully, to help figure out what the complete picture of these very dusty places in the universe looks like.

Chapter 1

Introduction

1.1 Dusty Galaxies in the Universe

Optical and near-IR imaging has revealed that most Luminous and Ultra-Luminous Infrared Galaxies (LIRGs and ULIRGs—see Sanders & Mirabel 1996), as well as many lower luminosity dusty galaxies including some starbursts and active galactic nuclei (AGNs), are interacting systems which have recently merged or are in the process of merging (Armus et al. 1987; Sanders et al. 1988b; Murphy et al. 1996). As a consequence, large quantities of gas and dust are driven into the nascent nuclei of these systems, catalyzing massive bursts of star formation (i.e. starbursts), and/or fueling accretion onto supermassive black hole accretion disks (i.e. AGNs) (Mihos & Hernquist 1996; Struck 1999).

Ultraviolet and optical emission from many of these dusty galaxies is significantly obscured by the same gas and dust that provides their infrared power—a fact which greatly complicates the process of diagnosing the star-formation and accretion contributions to their bolometric luminosities. Since LIRGs and ULIRGs are believed to be the largest contributors to the far-IR background and star-formation energy density at redshifts of $z \approx 1$–3 (Blain et al. 2002; Elbaz & Cesarsky 2003), and local ULIRGs are frequently used as analogues to the luminous sub-mm galaxy population, the development of a proper understanding of the histories of star-formation and galaxy evolution in the universe requires the construction of robust and reliable methods for diagnosing the dominant luminosity source powering obscured dusty galactic nuclei.

The need to tackle this problem grew following the discovery that infrared emission from dust contributes significantly to the bolometric luminosities of many galaxies. This large infrared contribution was first established through ground-based observations (Low & Kleinmann 1968; Kleinmann & Low 1970a,b), and subsequently by the all-sky survey performed with the *Infrared Astronomical Satellite* (*IRAS*—see e.g. Neugebauer et al. 1984). From these observations, it was found that the infrared luminosities of many late type galaxies—many of which were known through work at other wavelengths to be hosting an AGN or experiencing starburst episodes—were comparable to or in excess of their optical luminosities (Soifer et al. 1984b; Helou 1986).

Also discovered by *IRAS* were several classes of even more extreme objects (Houck et al. 1984; Soifer et al. 1984a): the previously mentioned LIRGs and ULIRGs, defined as galaxies having wavelength integrated luminosities $L_{\rm IR} \equiv L(8-1000\,\mu{\rm m}) \geq 10^{11}$ and 10^{12} $L_{\odot}$, respectively, as well as their more luminous siblings the Hyper-Luminous Infrared Galaxies (HyLIRGs), defined as galaxies having $L_{\rm IR} \geq 10^{13}$ $L_{\odot}$. These infrared-luminous classes of galaxies are characterized by $L_{\rm IR}/L_{\rm optical} \geq 0.5$ for LIRGs (Sanders et al. 1988a; Kim et al. 1995), and $L_{\rm IR}/L_{\rm optical} \geq$ 1–50 for ULIRGs and HyLIRGs (Sanders & Mirabel 1996). With $L_{\rm IR}/L_{\rm bol} \geq 0.5$, the bolometric luminosities of ULIRGs and HyLIRGs are dominated by emission at infrared wavelengths.

1.2 AGN and Starburst Diagnostics

Great progress towards the goal of diagnosing the nature of dusty galaxies was made using data from the *Infrared Space Observatory* (*ISO*—see e.g. Kessler 1999).

Diagrams based upon AGN-indicating high-ionization mid-IR lines (e.g. [O IV] and [Ne V]), the slope of the mid-IR continuum (which typically differs for starbursts and AGNs), as well as the star-formation-indicating strengths of the 6.2 and 7.7 μm polycyclic aromatic hydrocarbon (PAH; Leger & Puget 1984; Allamandola et al. 1985, 1987) emission features were constructed to quantify the relative contributions from accretion and starburst activity in many sources (e.g. Genzel et al. 1998; Lutz et al. 1998; Laurent et al. 2000; Tran et al. 2001). These observations provided evidence that ULIRGs are powered primarily by star-formation, with the fraction of AGN activity increasing with bolometric luminosity. However, due to the limited wavelength coverage and sensitivity of the *ISO* spectrometers, this analysis was limited to a relatively small number of bright nearby sources.

These observational challenges have largely been abated with the improved wavelength baseline and sensitivity of the Infrared Spectrograph[1] (IRS—see Houck et al. 2004) on the *Spitzer Space Telescope* (Werner et al. 2004). Large samples of starburst galaxies (Brandl et al. 2006), AGNs (Hao et al. 2005a; Weedman et al. 2005; Schweitzer et al. 2006), local ULIRGs (Armus et al. 2007), and their high-redshift counterparts (e.g. Houck et al. 2005; Yan et al. 2005; Lutz et al. 2005) have been observed with the IRS. As with the previous generation of studies with *ISO*, diagnostic diagrams have been constructed using the properties of high-ionization lines (with much improved sensitivity to place strict limits on [Ne V] emission), mid-IR spectral slopes (with a much broader mid-IR wavelength baseline), and PAH feature emission (now detected to $z \gtrsim 2$).

In addition to these observational diagnostics, many tools have been developed to model the spectral energy distributions (SEDs) of dusty galaxies. Models

[1]The IRS was a collaborative venture between Cornell University and Ball Aerospace Corporation funded by NASA through the Jet Propulsion Laboratory and the Ames Research Center.

containing a variety of grains-sizes and chemical compositions have been used to calculate the spectrum of emission from astronomical dust embedded in single (e.g. Desert et al. 1990; Li & Draine 2001; Draine et al. 2007) and multiple (e.g. Dale et al. 2001; Li & Draine 2002) incident radiation fields. Additionally, numerous radiative-transfer models have been published, including several to calculate the emission from an AGN and its obscuring torus (e.g. Nenkova et al. 2002; Dullemond & van Bemmel 2005). Finally, methods intended to decompose the SEDs of galaxies into a number of components have also been developed. For example, Klaas et al. (2001) present such a method and use it to decompose the far-IR SEDs of a sample of ULIRGs into contributions from several dust-modified blackbodies at different characteristic temperatures.

1.3 Spectral Energy Distribution Modeling

Like most areas of modern astrophysics, the theoretical modeling of the electromagnetic emission emerging from extragalactic sources has benefited greatly from the wealth of data acquired in recent years. Large surveys have provided important empirical constraints, putting theoretical models on an increasingly assured observational footing. However, the treatment of the physics of dusty molecular clouds and photodissociation regions (PDRs), and the subsequent application of this physics to modeling their contributions to the observed SEDs of galaxies, is a challenging and complex problem (see e.g. Hollenbach & Tielens 1997; Draine 2003) which is still largely unresolved.

The integrated ultraviolet to millimeter wavelength SEDs of galaxies are composed of continuum emission from stars, dust, and AGN accretion disks, as well

as line and feature emission from atoms, ions, and molecules. Considering just the emission from dust alone is a formidable task. The integrated spectrum of emission from all dust within a galaxy is obtained by summing over the emission from the many individual dust clouds within a galaxy, which themselves are each composite spectra of the emission from the many individual grains within a cloud. A "complete" model of the spectrum of dust emission from a galaxy therefore requires detailed knowledge of the dust composition and grain-size distribution function, as well as the geometric distribution of the emitting dust clouds with respect to the primary illuminating sources of radiation (i.e. populations of stars and an AGN) and any extinguishing dust clouds.

In principle, multi-dimensional radiative transfer calculations (e.g. Krugel & Siebenmorgen 1994; Nenkova et al. 2002; Dullemond & van Bemmel 2005) incorporating a realistic astronomical dust model (e.g. Draine & Li 2001; Li & Draine 2001) provide the optimal method with which to fully address these issues. However, many galaxies have very non-uniform morphologies, and detailed spatial information is available for only a handful of nearby sources. Lacking a complete description of the physical composition and structure of most galaxies, the parameter space within which to search for initial conditions that produce models in reasonable agreement with observations is both sizable and degenerate—especially for composite systems such as many LIRGs and ULIRGs. This degenerate set of initial conditions, as well as the computationally expensive and time-consuming nature of multi-dimensional radiative transfer modeling, makes the use of such methods impractical for the purposes of performing a systematic analysis of a large sample of sources.

1.4 A New Decomposition Method for Dusty Galaxies

We present in this dissertation a new method for use in decomposing the SEDs of galaxies into emission from populations of stars, an AGN accretion disk, PAH molecules, atomic and molecular lines, and distributions of thermally heated graphite and silicate grains at different fitted characteristic temperatures. Given the many observational and theoretical techniques to study dusty galactic nuclei described in §1.2, it is fair to question our decision to introduce yet another. We are motivated to do so for two principal reasons. First, as described in §1.3, while radiative-transfer methods incorporating realistic dust models provide the most physically complete method for modeling the SEDs of dusty galaxies, these methods are also the most dependent on the assumed geometry of the source. Second, the methods for calculating the theoretical emission from dusty galaxies described in §1.2 are primarily intended to model either starburst galaxies *or* AGNs. None of them, however, is particularly well-suited to calculating the emission from sources containing both a starburst *and* an AGN, each of which may be extinguished by different levels of obscuration (see §5.4 for an expanded discussion).

Our primary goals for this dissertation are therefore to present our decomposition method, to convince the reader that it is well-suited to analyzing the SEDs of composite sources, and to address the questions which motivated its development; in particular

1. *What energy source is primarily responsible for powering the emission from dusty galaxies?*
2. *How homogeneous are the SEDs of dusty galaxies which have similar AGN and starburst fractions?*

3. *What geometries can explain any inhomogeneities in the SEDs of similarly powered dusty galaxies?*

To meet these goals, we apply our decomposition method to a large sample of starburst galaxies and AGNs. The results of these decompositions provide templates with which to interpret and understand the properties of pure starburst galaxies and AGNs—i.e. the constituents of composite sources such as many LIRGs and ULIRGs. Additionally, as examples of such composite sources, we present fits to a large sample of ULIRGs obtained as part of the *Spitzer* GTO program, and describe in detail our study of the galaxies NGC 6240 and Mrk 1014.

Among our key results, we find in response to question (1) above, that we are able to use our decompositions to directly quantify the starburst and AGN strengths within some composite systems, and we use these results to construct a diagnostic diagram that is less sensitive to extinction than those used previously. We also find, however, that some sources (in particular some ULIRGs) are so heavily extinguished that they will require X-ray observations to detect the presence of an AGN. In response to question (2) above, we find that dusty galaxies are a very heterogeneous group. Furthermore, we find that starburst and AGN sub-samples of our complete dusty galaxy sample also display heterogeneous SEDs, showing that there is a significant amount of diversity even among like-classified sources. Finally, in response to question (3) above, we find that the variations in the SEDs of our starburst galaxies are largely consistent with a simple picture in which their principal differences result from variations in the optical depth through the dusty cocoons surrounding their newly formed stars. Additionally, we find that the differences in the far-IR SEDs of our AGNs may be largely explained by variations in the orientation of their AGN accretion disks with respect to the disks of the

galaxies hosting them. We use these latter inferences to caution against conclusions that may be drawn by assuming that SEDs of classes of galaxies are more homogeneous than they actually are (see §11).

We begin in §2 with an overview of the spectral decomposition method. In §3 we detail the method used to calculate the spectrum of emission from the various source components. In §4 and §5 we describe the adopted dust model and the method used to calculate the thermal emission from dust. In §6 and §7 we describe PAH feature and atomic and molecular line emission, respectively. In §8 we describe the sample of galaxies analyzed in this dissertation, in §9 we present our decompositions, and in §10 and §11 we analyze the results. Readers interested in the results of the decompositions, but not necessarily in the details of the decomposition method, may wish to read the general introduction to the method presented in §2.1, and then proceed directly to §8 for the results.

Chapter 2

Spectral Decomposition Method

2.1 Decomposition Components

The principal assumption in our decomposition method is that the ultraviolet to millimeter wavelength (10 Å–1000 μm) SED of a dusty galaxy may be completely described in terms of emission from evolved stars in the disk of the host galaxy (*ISRF*[1]—i.e. interstellar radiation field), populations of young stars in starbursts (*SB*), an AGN accretion disk (*AGN*), PAH molecules (*PAHs*), atomic and molecular lines (*lines*), and a maximum of four distributions of thermally heated graphite and silicate grains (*hot*, *warm*, *cool*, and *cold*). In this dissertation the *ISRF*, *SB*, and *AGN* components are collectively referred to as "source" emission components since they represent the primary illuminating sources heating dust within a galaxy. Similarly, the *hot*, *warm*, *cool*, and *cold* components are collectively referred to as "dust" emission components. Assuming these components form a complete basis describing the emission from dusty galaxies, the observed flux density may be expressed as[2,3]

$$f_\nu^{\rm total} = \frac{L_{\rm source}}{4\pi D_{\rm L}^2} \sum_{\rm source} \tilde{\alpha}_i \hat{f}_\nu^i + \frac{L_{\rm dust}}{4\pi D_{\rm L}^2} \sum_{\rm dust} \tilde{\alpha}_j \hat{f}_\nu^j + f_\nu^{\rm PAHs} + f_\nu^{\rm lines}, \qquad (2.1)$$

where $L_{\rm source}$ and $L_{\rm dust}$ are the total apparent luminosities of the source and dust components derived from the fit, $D_{\rm L}$ is the luminosity distance to the galaxy, $\tilde{\alpha}_i \equiv L_i/L_{\rm source}$ and $\tilde{\alpha}_j \equiv L_j/L_{\rm dust}$ are the fitted contributions to the total source and

[1]All names of decomposition components are printed in italic type throughout this dissertation.

[2]Variables accented with tildes are free parameters in the fitting.

[3]Note that f_λ units (e.g. erg s^{-1} cm^{-2} μm^{-1}) may be substituted for f_ν units (e.g. Jy or erg s^{-1} cm^{-2} Hz^{-1}) throughout this dissertation.

dust luminosities from each component, the $\hat{f}_\nu^i \equiv f_\nu^i / \int f_\nu^i \, d\nu$ are the normalized flux densities from each source or dust component, and $f_\nu^{\rm PAHs}$ and $f_\nu^{\rm lines}$ are the fitted PAH and emission line flux densities. We include a maximum of four dust components, which are typically heated to characteristic temperatures of $\bar{T}_{\rm hot} \approx 1400\,{\rm K}$, $\bar{T}_{\rm warm} \approx 200\,{\rm K}$, $\bar{T}_{\rm cool} \approx 80\,{\rm K}$, and $\bar{T}_{\rm cold} \approx 35\,{\rm K}$, although as described in §4.3, the actual temperature of each is determined from the fitted magnitude of the illuminating radiation field energy density. See §9.2 for a complete summary of the free parameters in the model.

Figure 2.1 presents an illustration of one possible geometric structure of a dusty galaxy within which to interpret the roles played by each of the decomposition components in equation (2.1). Panel (a) depicts the optically-thin (at mid-IR wavelengths) host galaxy from which evolved photospheric (*ISRF*) and *cold* dust emission emerges. Panel (b) shows an enlarged view of the central region of the galaxy, which consists of an AGN and a starburst, surrounded by extinguishing screens of *cool* and *cold* dust. Panel (c) depicts the composite nucleus of the dusty galaxy, and the details of each nuclear component are shown in panel (d). The starburst is composed of *SB* emission from young stars, *warm* dust in the shells surrounding the young stars, and possibly *cool* and/or *cold* dust in spherical screens around each individual star-forming cloud. The AGN consists of emission from the *AGN* accretion disk, *hot* and *warm* dust on the illuminated and shaded sides of the dust clouds creating the obscuring torus (or dust in illuminated and shielded regions of a "classic" torus with a smooth dust distribution—see Fig. 5.1), and *warm* and *cool* dust in narrow-line-region clouds (again from dust in illuminated and shaded regions). We emphasize that our method does not require the definition of *any* specific geometry (i.e. we derive the contributions from each emission component without the need to define its proximity to any other component),

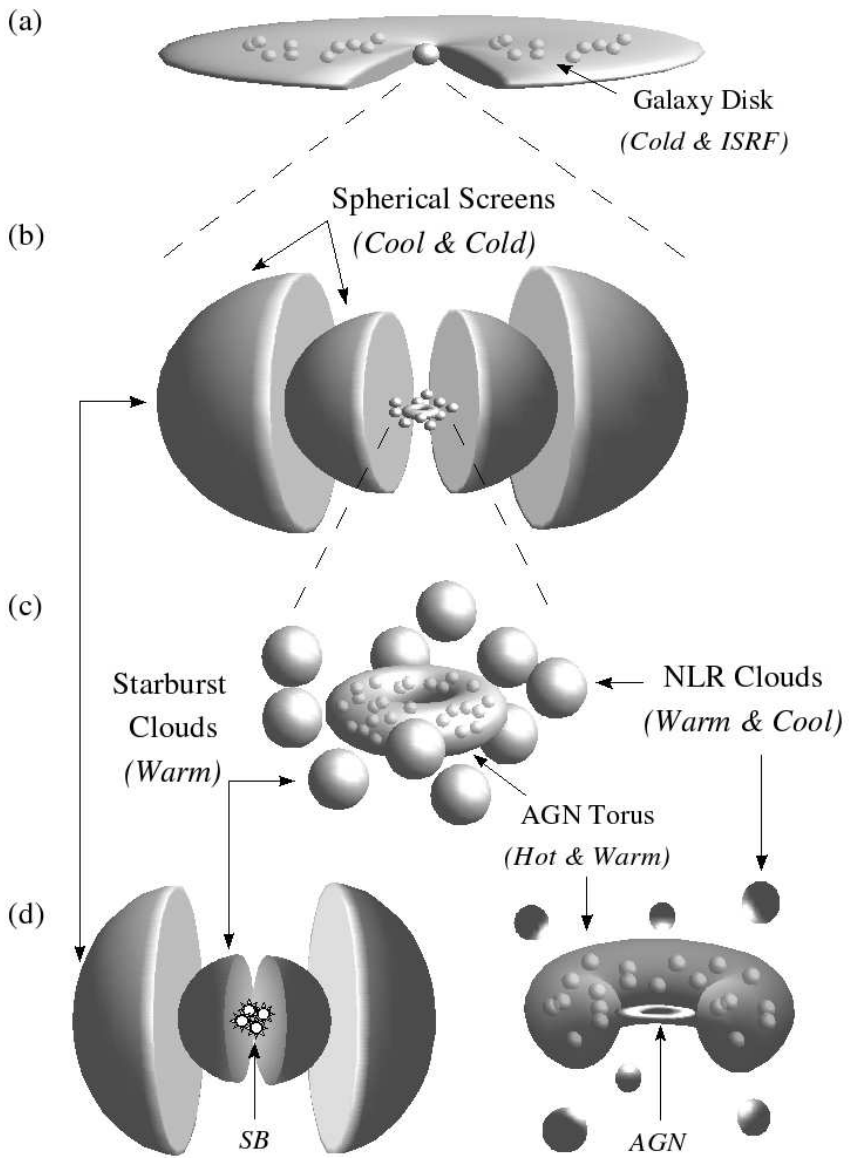

Figure 2.1 Example geometry of a dusty galaxy, demonstrating the potential roles played by each of our decomposition components. Panel (a) depicts the host galaxy disk which gives rise to *cold* dust emission and knots of *ISRF* emission from evolved stars. Panel (b) shows an enlarged view of the core of the galaxy embedded within obscuring screens of *cool* and *cold* dust. Panels (c) and (d) depict the composite nucleus. The starburst contains *SB* emission from young stars, *warm* dust in the surrounding shells, and possibly *cool* and/or *cold* dust in spherical screens around each individual star-forming cloud. The AGN contains an *AGN* accretion disk, *hot* and *warm* dust in the obscuring torus, and *warm* and *cool* dust in narrow-line-region (NLR) clouds.

and the actual geometry of a dusty galaxy may look quite different from the one presented. The illustration in Figure 2.1 should therefore not be taken as a literal description of the geometry of a particular galaxy (since our method requires none), but instead is intended to provide a structure within which to visualize the multiple roles potentially played by each decomposition component.

We note that star-formation in the disk of the host galaxy and in starburst regions are both explicitly accounted for via the *ISRF* and *SB* components. Furthermore, while Figure 2.1 depicts the specific case of a nuclear starburst, the actual location of the star-formation (e.g. nuclear versus off-center) has no effect on the decomposition (assuming that any off-center emission is contained within the spectroscopic slits and photometric apertures used to construct the SEDs). For example, in the decomposition of an off-center starburst, the *cool* and *cold* decomposition components (or portions thereof) could be interpreted as belonging to off-center obscuring clouds. Note, however, that if a galaxy contains both a highly-enshrouded nuclear starburst and a less-enshrouded off-center starburst, our decomposition method cannot explicitly fit both components simultaneously. Instead, a mean optical depth somewhere between the optical depths of the two individual components is obtained. Thus, care must be taken when interpreting the optical depths inferred from a globally integrated SED—an admonishment that is not unique to our analysis, but is a general statement about the nature of spatially integrated (i.e. unresolved) data.

2.1.1 Decomposition Algorithm

Once assembled, the ultraviolet to millimeter wavelength SEDs of the galaxies in our sample are fit to the model of the total flux density from equation (2.1).

The best-fit parameters are determined using a Levenberg-Marquardt least-squares routine to minimize

$$\chi^2 = \sum_k w_k \left[f_\nu^{\rm data}(\lambda_k) - f_\nu^{\rm total}(\lambda_k) \right]^2 , \tag{2.2}$$

where the w_k are the weights applied at each wavelength λ_k (see §2.1.2), $f_\nu^{\rm data}$ is the observed flux density, and $f_\nu^{\rm total}$ is the modeled flux density from equation (2.1). For photometric data, we integrate the modeled flux density over the filter transmission curve (if available) to properly calculate the broadband flux density. This is important for photometric bands containing emission and absorption features (e.g. L-band photometry containing the 3.3 μm PAH, 3.1 μm water-ice, and 3.4 μm HAC features—see §4.8 and §6), as well as those bands covering spectral regions that change rapidly with wavelength (e.g. J-band photometry sampling extinguished photospheric emission—see the near-IR fit to NGC 6240 in §9.1).

Experience has taught us that the greater the number of free parameters in a fitting model, the less likely the resulting "best-fit" will converge to the desired global minimum in the χ^2 function. Correspondingly, it becomes increasingly likely that the fit will converge to a local minimum, often with very unsatisfactory results. This is a practical matter and not a mathematical one since a fit with any number of parameters will reach the global minimum given sufficiently well-chosen initial conditions. In practice, however, it is desirable to have a more robust fitting method to increase the likelihood that a *reasonably* chosen set of initial conditions will converge to the global minimum (although we note that it is impossible to guarantee this will happen in all cases when using an automated method to construct the initial conditions). To meet this goal, we have developed an algorithm which separates the processes of fitting the continuum—defined as the sum of the source and dust components—and the individual PAH features

and atomic and molecular emission lines. Such a division into two separate least-squares processes greatly reduces the total number of free parameters in each fit. Parameter errors are calculated after the first step of the fitting procedure and propagated through to the following fit (see §2.1.2), so that the net accumulated uncertainty is reliably calculated.

After an SED has been fit, we perform a series of tests to ensure that all components are well-constrained (i.e. that the parameter errors are smaller than their values). First, if the *ISRF* luminosity is $< 1\%$ the sum of the luminosities of all source components, then the fit is repeated without the *ISRF* component. Similarly, if any of the observed dust component luminosities are $< 1\%$ the sum of the apparent luminosities of all dust components, the fit is repeated without those components. All three source components and the *hot* dust component emit strongly at ultraviolet to near-IR wavelengths. For some galaxies, these overlapping emission components are degenerate and result in unconstrained parameters. Our second check is therefore to test if either the *SB* or *AGN* components are unconstrained (i.e. if their luminosity uncertainties exceed their luminosities). If the *SB* component is unconstrained, we fix the *SB*-to-*PAHs* luminosity ratio (i.e. the ratio of the unextinguished *SB* luminosity to the *PAHs* luminosity—see §9.2) to the value derived from fits to the template starbursts NGC 7714 and NGC 2623, and restart the fit. Similarly, if the *AGN* component is unconstrained, we fix the *AGN*-to-*hot* dust luminosity ratio (i.e. the ratio of the unextinguished *AGN* luminosity to the unextinguished *hot* dust luminosity—see §9.2) to the value derived from fits to the template AGNs PG 0804+761 and Mrk 463, and restart the fit. As our final test, if any of the fitted optical depths are unconstrained, we fix the most unconstrained to zero and restart the fit. This sequence provides a well-defined method by which to sequentially impose constraints until a successful fit is obtained.

The steps in the fitting method are therefore: (1) Input the observed SED and the initial estimates of the *PAHs* and *lines* components derived from the IRS spectrum (see §6 and §7); (2) Subtract the estimated *PAHs* and *lines* components from the observed SED to create an observed continuum emission SED; (3) Decompose this SED using the model in equation (2.1) to obtain the fitted continuum; (4) Subtract this fitted continuum from the observed SED to create an observed PAH feature and line emission spectrum; (5) Fit the individual features in this spectrum; (6) Perform the sequence of tests to ensure that the fit is well-constrained; and (7) If necessary, repeat the fitting process with constrained components.

2.1.2 Data Weighting

The success or failure of a fitting algorithm and the reliability of the results is largely dependent upon the chosen method of weighting the data in equation (2.2). We adopt the function

$$w_k = \frac{\hat{\Lambda}_k}{\sigma^2(\lambda_k)}, \tag{2.3}$$

where $\sigma(\lambda_k)$ is the total 1–σ uncertainty in the flux density at wavelength λ_k, and $\hat{\Lambda}_k$ is a term which compensates for non-uniform wavelength sampling (i.e. ensuring that a region of the SED does not dominate the fit simply because it contains many more wavelength samples—see Appendix A). The total uncertainty in any observed data is given by the quadratic sum of the statistical and calibration (i.e. systematic) uncertainties. For IRS spectroscopic data, we use the difference of two spectra obtained at different nod positions (as produced during a typical IRS observation) to estimate the statistical uncertainties (see Appendix B for details). Carefully extracted low-resolution IRS spectra may still exhibit some residual calibration uncertainties (e.g. fringes in the long-low modules), which we

estimate to be $\sim$2% of the flux density at any given wavelength (based upon the observed magnitude of these residual features). For photometric data, the total uncertainty is taken to be equal to the quadratic sum of the uncertainties provided in the literature and an absolute calibration uncertainty (e.g. from scaling to the IRS apertures) taken to be 5%. The actual systematic uncertainties in the photometric data are difficult to estimate, although we note that the results of the decompositions are fairly insensitive to the specific adopted value of the systematic uncertainty since the sampling term ($\hat{\Lambda}$) dominates the weighting function.

As described in §2.1.1, each decomposition consists of two separate least-squares fits. In the first of these (step 3 above), the flux density that is fit is obtained by subtracting the *PAHs* and *lines* components from the observed SED, i.e. $f_\nu = f_\nu^{\rm data} - f_\nu^{\rm PAHs} - f_\nu^{\rm lines}$. When a component is subtracted from observed data to create an SED to be fitted, the uncertainty of the subtracted component must be propagated through the analysis. Thus, the total uncertainty input into the least-squares routine for this first fit is $\sigma^2 = \sigma_{\rm data}^2 + \sigma_{\rm PAHs}^2 + \sigma_{\rm lines}^2$. Here, $\sigma_{\rm data}$ is the uncertainty in the observed flux density, while $\sigma_{\rm PAHs}$ and $\sigma_{\rm lines}$ are the uncertainties in the estimated *PAHs* and *lines* components, respectively. Since the estimated strengths of the *PAHs* and *lines* components are derived from the observed spectrum, $\sigma_{\rm PAHs}$ and $\sigma_{\rm lines}$ are dominated by the IRS uncertainties. We therefore adopt $\sigma_{\rm PAHs} = \sigma_{\rm lines} = 0$, since the uncertainties in the IRS data on which they depend are already included through $\sigma_{\rm data}$. In the second fit (step 5 above), the flux density that is fit is obtained by subtracting the fitted continuum from the observed SED, i.e. $f_\nu = f_\nu^{\rm data} - f_\nu^{\rm cont}$, so that the total uncertainty input into the least-squares routine is $\sigma^2 = \sigma_{\rm data}^2 + \sigma_{\rm cont}^2$. Here, $\sigma_{\rm cont}$ is the formal uncertainty in the continuum calculated using the full covariance matrix obtained from the first fit.

Chapter 3

Source Emission

3.1 *ISRF* Component Emission

We adopt the model of the average interstellar radiation field presented in Mezger et al. (1982) and Li & Draine (2001) to represent the SED of emission from stars in the disk of a galaxy. In this model, the mean energy density in the solar neighborhood, $c\,u_\nu^{\mathrm{ISRF}} = f_\nu^{\mathrm{ISRF},\odot} = 4\pi J_\nu^{\mathrm{ISRF},\odot}$, is given by

$$u_\nu^{\mathrm{ISRF}} \propto \begin{cases} 0 & \lambda < 912\,\text{Å}, \\ \lambda^{5.4172} & 912\,\text{Å} < \lambda < 1100\,\text{Å}, \\ \lambda^{2} & 1100\,\text{Å} < \lambda < 1340\,\text{Å}, \\ \lambda^{0.3322} & 1340\,\text{Å} < \lambda < 2460\,\text{Å}, \\ \sum_n W_n B_\nu(T_n) & \lambda > 2460\,\text{Å}, \end{cases} \tag{3.1}$$

where B_ν is the Planck function per unit frequency and the $W_n = [0.025,\, 0.25,\, 1]$ are weighting factors for each blackbody component of temperature $T_n = [7500\,\mathrm{K},\, 4000\,\mathrm{K},\, 3000\,\mathrm{K}]$. This model spectrum is shown in Figure 3.1, normalized to have unit integrated energy density. Emission from the *ISRF* decomposition component is assumed to emerge from the galaxy disk, so that the line-of-sight extinction to the emitting stars is small in the infrared (i.e. $\lambda > 1\,\mu\mathrm{m}$). The flux density per unit frequency interval of emission from the *ISRF* component for use in equation (2.1) is therefore

$$f_\nu^{\mathrm{ISRF}} \propto u_\nu^{\mathrm{ISRF}}. \tag{3.2}$$

An example *ISRF* component SED, f_ν^{ISRF}, is shown in Figure 3.2. Displayed alongside the *ISRF* component is the emission from a 3500 K blackbody (characteristic

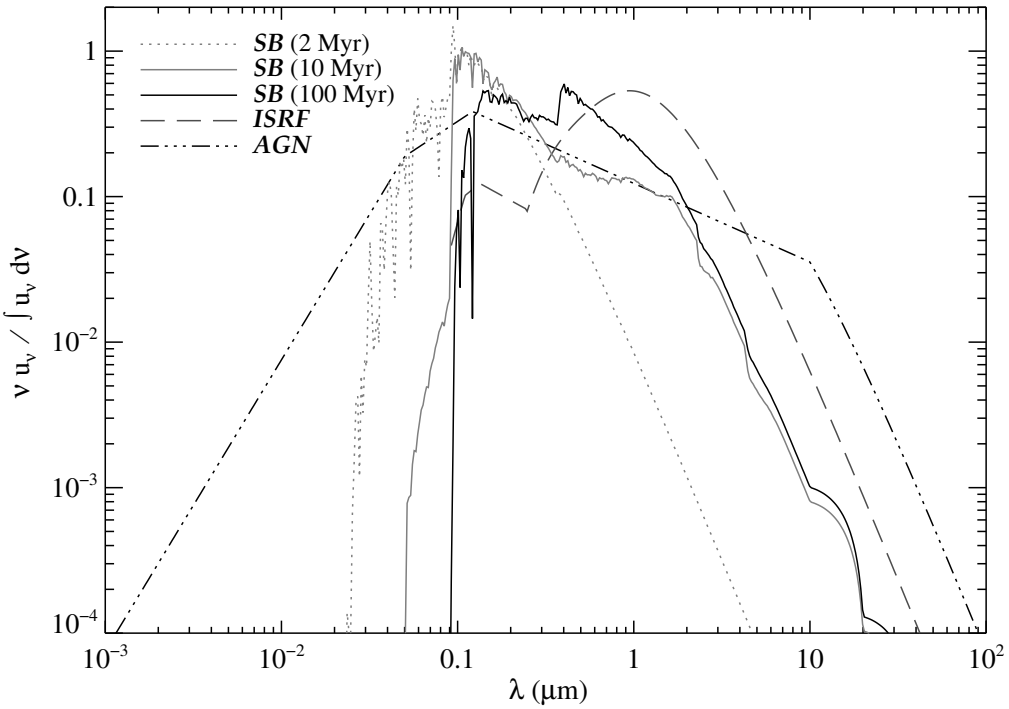

Figure 3.1 Normalized 10 Å–1000 μm energy densities of the principal luminosity sources in dusty galaxies—i.e. emission from starbursts 2, 10, and 100 Myr after an instantaneous burst (*SB*); evolved disk stars (*ISRF*); and an AGN accretion disk (*AGN*).

of evolved stars), scaled to match at 1.5 μm. The two curves are nearly identical at $\lambda > 1\,\mu$m, so that fitting near-IR data with the *ISRF* component is very similar to fitting it with a 3500 K blackbody.

3.2 *SB* Component Emission

In contrast to the modest $\sim 1\,M_\odot\,\mathrm{yr}^{-1}$ star-formation rate characteristic of emission from the *ISRF* component, the rates in starbursts are often much higher (e.g. $\gtrsim$ 10–100 $M_\odot\,\mathrm{yr}^{-1}$), resulting in significantly different stellar populations. In order to properly characterize the spectral properties and bolometric luminosities of these populations, we use Starburst99 (Leitherer 1990) to generate SEDs of in-

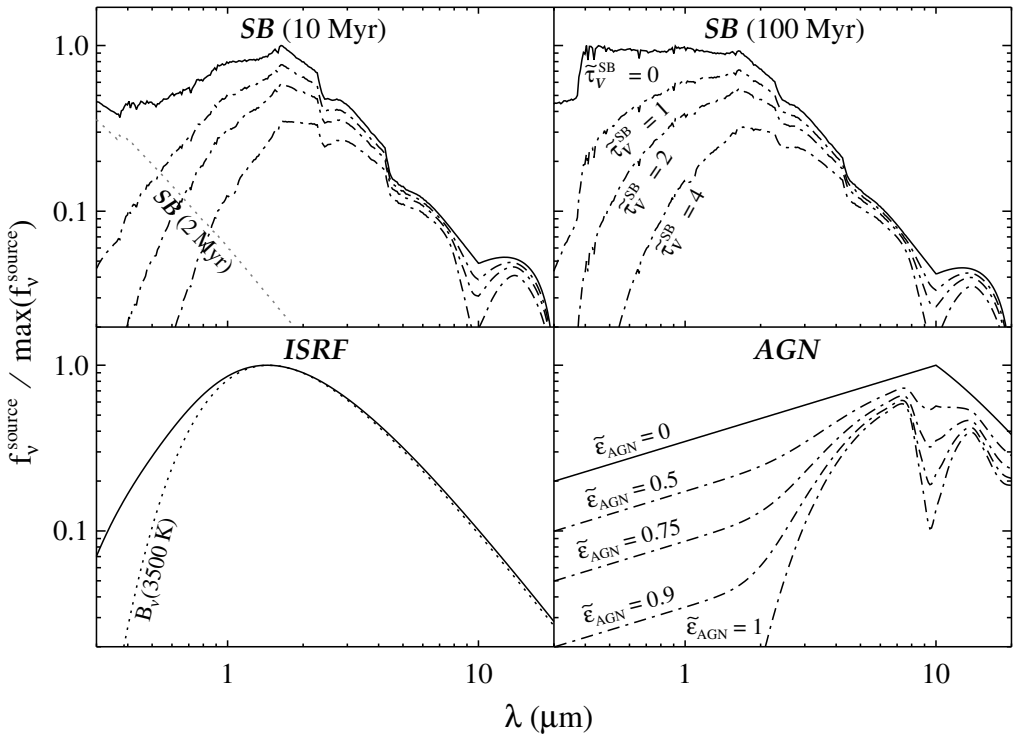

Figure 3.2 Example SEDs of emission from a starburst (*SB*) 10 and 100 Myr after an instantaneous burst, evolved disk stars (*ISRF*), and an AGN accretion disk (*AGN*). Also shown are the SEDs of the *SB* components extinguished by obscuring screens with the indicated optical depths, and the SEDs of the *AGN* component behind a $\tau_V \approx 25$ screen for the indicated covering factors (*dash-dotted lines*). Note that emission from the 2 Myr starburst population declines steeply at $\lambda > 3000\,$Å, and that the *ISRF* component is very similar to a 3500 K blackbody for $\lambda > 1\,\mu$m (*dotted lines*—see text).

stantaneous bursts at different epochs. We assume a Kroupa IMF (Kroupa 2001) having a $M^{1.3}$ power-law in the 0.1–0.5 $M_\odot$ range and a $M^{2.3}$ power-law in the 0.5–100 $M_\odot$ range. We further assume Padova AGB tracks with solar metallicity (Girardi et al. 2000). Populations of stars in starbursts evolve dramatically during the first 10 Myr after a burst. At 4 Myr the most massive stars still exist on the main sequence, but by 10 Myr all of the photoionizing stars have evolved into supergiants. As shown in Figure 3.1, the emission from a starburst 2 Myr after a

burst emerges almost exclusively at ultraviolet wavelengths. Since we have very little data in this wavelength range for the sources in our sample, we are unable to explicitly constrain the presence or absence of such a population. In contrast to this, the 10 and 100 Myr populations emit a large fraction of their luminosity at optical and longer wavelengths, where our SEDs are better constrained. Therefore, in order to adequately sample the evolutionary stages in a starburst that we are sensitive to, and to smoothly transition into the evolved population modeled with the *ISRF* component, we create a composite starburst spectrum containing equal contributions from the 10 and 100 Myr populations—i.e. $u_\nu^{\rm SB} = (u_\nu^{\rm SB10} + u_\nu^{\rm SB100})/2$. We note, however, that the omission of an ultraviolet-luminous young stellar population from $u_\nu^{\rm SB}$ may result in an underprediction of the total *SB* luminosity for some sources, perhaps by up to $\sim$1/3 if the 2 Myr population contributes at the same level as each of the older populations.

Unlike emission from the *ISRF* component, we assume that *SB* component emission emerges from regions that may be obscured by screens of dust out to infrared wavelengths. If the obscuration to the *SB* component is dominated by dust in the cocoons of material surrounding each star-forming knot, and not by extinction between the various knots, then the majority of the obscuration occurs via a screened geometry. Levenson et al. (2007) use radiative transfer models to show that such a screened geometry is actually required to reproduce the deep 9.7 μm silicate features observed in many ULIRGs, suggesting that the assumption of a screened geometry is reasonable for highly obscured sources. At lower optical depths (i.e. $\tau < 1$), mixed and screened geometries both give rise to extinctions scaling approximately as $f/f_0 \approx 1 - \tau$, so that the choice between the form of extinction is less critical. We therefore model the flux density per unit frequency

interval of emission from the *SB* component as

$$f_\nu^{\rm SB} \propto u_\nu^{\rm SB} e^{-\tau_{\rm SB}}, \tag{3.3}$$

where the optical depth through the obscuring screen to the *SB* component is given by

$$\tau_{\rm SB}(\lambda) = \tilde{\tau}_V^{\rm SB} \frac{\Sigma_{\rm abs}(\lambda)}{\Sigma_{\rm abs}(5500\,\text{Å})}. \tag{3.4}$$

Here, $\tilde{\tau}_V^{\rm SB}$ is the screen optical depth to the *SB* component at 5500 Å, and $\Sigma_{\rm abs} = \Sigma_{\rm ext} - \Sigma_{\rm scat}$ is the total dust absorption opacity obtained by subtracting the scattering opacity from the total extinction opacity (see §4.7). We use the absorption and not the extinction opacity in equation (3.4) since scattering tends to cancel itself out in sufficiently spherical geometries, such as depicted in Figure 2.1 (i.e. light scattered out of the beam along the direct path to the observer is offset by light scattered into the beam along another path). Furthermore, the extinction and absorption opacities of dust in our model have similar slopes between 1000 Å and 3 μm, where the *SB* component emits strongly. Since the derived optical depth depends only on the opacity slope and not its absolute value, the omission of scattering has very little effect. We note, however, that this omission may introduce some small uncertainties at $\lambda \lesssim 3\,\mu$m, where the scattering opacity is largest. Example 10 and 100 Myr SEDs, $f_\nu^{\rm SB10}$ and $f_\nu^{\rm SB100}$, used to construct the composite *SB* model, $f_\nu^{\rm SB}$, are shown in Figure 3.2. Also shown are example SEDs obscured by screens of dust with $\tilde{\tau}_V^{\rm SB} = 1$, 2, and 4.

3.3 *AGN* Component Emission

The spectral properties of radiation emerging from an AGN accretion disk depend sensitively upon the assumed geometry of the surrounding obscuring structure—

i.e. the putative torus of AGN unification models (Antonucci 1993). Important geometrical factors include the height of the inner edge of the torus, its proximity to the nucleus, the clumpy versus smooth structure of the obscuring medium, and the orientation of the torus with respect to the observer. Radiative-transfer calculations incorporating these geometric properties have been used to construct models of the emission from an AGN accretion disk and its obscuring torus (e.g. Pier & Krolik 1992; Laor & Draine 1993; Granato & Danese 1994; Nenkova et al. 2002; Dullemond & van Bemmel 2005). Since our intent in this dissertation is to characterize the general properties of the emergent SEDs of large samples of galaxies, and not to discern the detailed properties of the obscuring torus in individual sources, such modeling is unnecessary for our purposes.

Instead, we adopt an empirical model of the emission from an AGN accretion disk and assume that this SED may be extinguished by a foreground screen of dust. We use the accretion disk model from Schartmann et al. (2005) in which the emergent energy density, shown in Fig. 3.1, is modeled by

$$u_\nu^{\rm AGN} \propto \begin{cases} 0 & \lambda < 10\,\text{Å}, \\ \lambda^3 & 10\,\text{Å} < \lambda < 500\,\text{Å}, \\ \lambda^{1.8} & 500\,\text{Å} < \lambda < 1216\,\text{Å}, \\ \lambda^{0.46} & 1216\,\text{Å} < \lambda < 10\,\mu\text{m}, \\ B_\nu(1000\,\text{K}) & \lambda > 10\,\mu\text{m}. \end{cases} \tag{3.5}$$

The flux density per unit frequency interval of emission from the *AGN* component, including an obscuring screen with a non-uniform covering factor, is modeled as

$$f_\nu^{\rm AGN} \propto u_\nu^{\rm AGN} \left[(1 - \tilde{\epsilon}_{\rm AGN}) + \tilde{\epsilon}_{\rm AGN} e^{-\tau_{\rm AGN}} \right], \tag{3.6}$$

where $0 \leq \tilde{\epsilon}_{\rm AGN} \leq 1$ is the fraction of the accretion disk obscured by a screen of

optical depth

$$\tau_{\rm AGN}(\lambda) = \tilde{\tau}_V^{\rm AGN} \frac{\Sigma_{\rm ext}(\lambda)}{\Sigma_{\rm ext}(5500\,\text{Å})}. \tag{3.7}$$

Here, $\tilde{\tau}_V^{\rm AGN}$ is the screen optical depth to the *AGN* component at 5500 Å. An example unobscured *AGN* component SED, $f_\nu^{\rm AGN}$, is shown in Figure 3.2. Also shown are the SEDs of *AGN* component emission obscured by a $\tilde{\tau}_V^{\rm AGN} = 25$ screen, for several values of the screen covering factor $\tilde{\epsilon}_{\rm AGN}$. Note that significant ultraviolet and optical emission may still emerge from a highly extinguished accretion disk if the covering factor is less than unity.

In the bottom panel of Figure 2.1, the AGN accretion disk is depicted as being surrounded by an obscuring structure composed of discrete clouds and/or a smooth dusty component. The covering factor, $\tilde{\epsilon}_{\rm AGN}$, may therefore be interpreted as the fraction of the accretion disk covered by this obscuring material (from the point-of-view of the observer), which has an approximate visual band optical depth equal to $\tilde{\tau}_V^{\rm AGN}$. Note that the same qualifications regarding the relative importance of scattering and the subsequent uncertainties in the emergent flux density for $\lambda \lesssim 3\,\mu$m that were made for the *SB* component apply here as well. Since the clumpy torus is by definition not spherically symmetric, we use the full extinction opacity (including scattering) in equation (3.7). As described for the *SB* component, this choice has very little effect on the results since the extinction and absorption opacities have similar slopes from the ultraviolet to the near-IR, where the *AGN* component emits strongly.

Chapter 4

Astronomical Dust Model

4.1 Grain Properties

Observations of extinguished starlight passing through diffuse clouds along lines of sight in the Galaxy provide empirical evidence that interstellar dust grains are composed of graphitic materials and silicates. The observed 2175 Å absorption features is approximately reproduced by small graphite particles (Stecher & Donn 1965; Wickramasinghe & Guillaume 1965), while the observed ∼9.7 and ∼18 μm absorption features are attributed to the Si–O stretching mode, and O–Si–O bending mode of silicates.

Mathis et al. (1983, hereafter MRN) showed that the observed interstellar extinction can be reproduced by a simple two-component grain model, with graphite and silicate grains distributed in size according to

$$\frac{1}{n_{\rm H}}\frac{dn_i}{da} = A_i\ a^{-3.5}. \tag{4.1}$$

Here, the grain-size, a, runs from a minimum of $a_- = 50$ Å to a maximum of $a_+ = 0.25\,\mu$m, $n_i(a')$ is the number density of grain type i with size $a \leq a'$, and $n_{\rm H}$ is the hydrogen nucleon number density. The normalization factors for the graphite and silicate distributions were found by Draine & Lee (1984) to be $\log(A_{\rm gra}) = -25.11$ and $\log(A_{\rm sil}) = -25.16$, respectively, with A_i in units of cm$^{2.5}$ H^{-1}. For graphite and silicate densities of 2.24 and 3.5 g cm^{-3}, the total dust mass per hydrogen nucleon for the MRN model is 1.53×10^{-26} g H^{-1}.

More complex forms for the grain-size distribution function have been defined

by various authors in an attempt to explain the observed variations in extinction along different lines of sight through the Galaxy. Kim et al. (1994) use a smooth exponential cutoff at large grain-sizes to reproduce the extinction curves for various values of the parameter $R_V \equiv A_V/E_{B-V}$, the ratio of the visual extinction to the reddening. Weingartner & Draine (2001, hereafter WD01) use a similar form, but allow more freedom in the shape of their "power-law", and add log-normal populations of small grains to account for the observed diffuse emission from stochastically heated grains.

We adopt the WD01 grain-size distribution function and the optical properties of graphitic carbon and smoothed astronomical silicate from Draine & Lee (1984) and Laor & Draine (1993), with modifications from Weingartner & Draine (2001) and Li & Draine (2001). We modify the WD01 distribution function to include a small grain-size exponential cutoff, which we use to model the deficit of small grains that results from sublimation in intense heating conditions (see §4.2). The modified distribution function for graphite and silicate grains takes the form

$$\frac{1}{n_{\rm H}}\frac{dn_i}{da} = \left[\frac{1}{n_{\rm H}}\frac{dn_i}{da}\right]_{\rm WD01}\left(1-\exp\left[-\left(\frac{a}{a_-^i}\right)^{\beta_-}\right]\right), \tag{4.2}$$

where $[n_{\rm H}^{-1}dn_i/da]_{\rm WD01}$ is the WD01 distribution function for grains with radii satisfying $3.5\,\text{Å} \le a \lesssim 1\,\mu$m, $a_- = a_-(\tilde{U})$ is the minimum surviving grain-size in a distribution embedded in a radiation field with an energy density of magnitude $\tilde{U}$ (see §4.2 and eq. [4.3]), and β_- determines the exponential cutoff rate. In the limit of $\beta_- \to \infty$, the exponential provides a sharp cutoff at $a = a_-$. We choose $\beta_- = 3$, the same value adopted for the large grain-size exponential cutoff in WD01 (although we note that the specific value chosen has negligible impact on the results). The total dust mass per hydrogen nucleon for the WD01 model is 1.89×10^{-26} g H^{-1}.

Absorption and extinction efficiencies, $Q^i_{\rm abs}$ and $Q^i_{\rm ext}$, have been tabulated for graphite and silicate spheres as described in Laor & Draine (1993) to cover the wavelength range $10\,\text{Å} < \lambda < 1000\,\mu$m. Absorption cross sections are calculated from $C^{\rm gra}_{\rm abs}(a,\lambda) = \pi a^2 Q^{\rm gra}_{\rm abs}(a,\lambda)$ and $C^{\rm sil}_{\rm abs}(a,\lambda) = \pi a^2 Q^{\rm sil}_{\rm abs}(a,\lambda)$, with similar expressions for the extinction cross sections $C^{\rm gra}_{\rm ext}(a,\lambda)$ and $C^{\rm sil}_{\rm ext}(a,\lambda)$.

4.2 Grain Sublimation

Graphite and silicate grains sublimate when heated to temperatures above 1750 and 1400 K, respectively (Laor & Draine 1993). The minimum surviving grain-size in a distribution, a_-, is determined by the size of the smallest grain which does not sublimate in the radiation field in which the distribution is embedded. As the magnitude of the radiation field energy density increases, the grain distribution becomes increasingly depleted of small grains. A stronger radiation field therefore changes the SED of emission from a distribution of grains both by increasing the temperature of the grains, and by weighing the grain-size distribution function to larger grains. Additionally, due to their lower sublimation temperature, silicate grains become depleted before graphite grains. Sublimation is one of many physical processes which can set the minimum grain-size within a distribution. Shock waves (Jones et al. 1994; Draine 1995), sputtering (Draine & Salpeter 1979), and grain-grain collisions (Tielens et al. 1994) can also influence the minimum grain-size. However, these other effects are more difficult to model than sublimation, since they require a dynamic model of the region where the grains are located, and we do not consider them further.

4.3 Thermal Heating

The equilibrium temperature which a grain reaches is a function of its composition, size, and the spectrum and strength of the radiation field in which it is embedded. Our adopted dust model contains grains spanning several orders of magnitude in size, so that the temperatures of individual grains within a distribution embedded in a given radiation field vary greatly. For a graphite or silicate grain embedded in a radiation field with normalized energy density $\hat{u}_\nu$ (see Fig. 3.1) which has a fitted magnitude $\tilde{U}$, energy conservation gives

$$\int C^i_{\rm abs}(a,\nu)\tilde{U}c\hat{u}_\nu\,d\nu = \int C^i_{\rm abs}(a,\nu)4\pi B_\nu[T^i_{\rm eq}(a)]\,d\nu. \tag{4.3}$$

Here, the left and right sides represent the rates at which energy is absorbed and emitted by a grain, respectively. Equation (4.3) is therefore an implicit equation for the equilibrium temperatures, $T^i_{\rm eq}(a)$, of the graphite and silicate grains in a distribution. These temperatures are used in equation (4.6) to properly calculate the spectrum of emission from each decomposition component. We calculate the temperatures of grains in the *hot* dust component using the normalized *AGN* energy density, $\hat{u}^{\rm AGN}_\nu$, and the temperatures of grains in the *warm*, *cool*, and *cold* dust components using the normalized *ISRF* energy density, $\hat{u}^{\rm ISRF}_\nu$ (see Fig. 3.1). Note that although the shape of the illuminating radiation field does have an effect on the temperature of grains (since grains absorb and emit more efficiently at certain wavelengths), similar grain temperatures may be obtained from two different radiation fields by suitably adjusting the magnitude of the energy density of each. Thus, the specific choices of illuminating radiation fields we use to calculate our dust equilibrium temperatures do not have a significant impact on our results. Note also that once the shape of the normalized energy density is chosen, the temperature of a grain scales with the fitted magnitude of the energy density.

4.4 Stochastic Heating

The heat capacities of very small grains are sufficiently small that they undergo large temperature fluctuations upon absorption of individual photons, and reradiate most of the deposited energy on timescales much shorter than the typical time between photon strikes. To estimate the importance of this stochastic heating for our dust components, we calculate the threshold grain-size below which grains fall out of thermal equilibrium. This critical radius is calculated by finding the grain-size for which the timescales of photon absorption, $\tau_{\rm abs} = \dot{N}_\gamma^{-1}$, and grain cooling, $\tau_{\rm emit} = \bar{E}_\gamma / \dot{E}_{\rm emit}$, are equal. Here, $\dot{N}_\gamma = \int C_{\rm abs}\,(cu_\nu/h\nu)\,d\nu$ is the photon absorption rate, $\bar{E}_\gamma = \tau_{\rm abs}\,\dot{E}_{\rm abs} = \tau_{\rm abs}\int C_{\rm abs}\,cu_\nu\,d\nu$ is the mean energy absorbed per photon, and $\dot{E}_{\rm emit} = \int C_{\rm abs}\,4\pi B_\nu(T_{\rm vib})\,d\nu$ is the grain luminosity, with $T_{\rm vib}$ the "vibrational temperature" of a grain with internal energy $\bar{E}_\gamma$ (see Draine & Li 2001). For graphite grains, Draine & Li (2001) find

$$a_{\rm min} \approx 100\,{\rm \AA}\left(\frac{u}{u_{\rm MMP}}\right)^{-0.2}, \tag{4.4}$$

where $u \equiv \int u_\nu d\nu$ is the integrated spectral energy density of the illuminating radiation field, and $u_{\rm MMP}$ is the integrated spectral energy density of the local interstellar radiation field from Mezger et al. (1982). For our *cold*, *cool*, *warm*, and *hot* dust components, typical threshold grain-sizes from equation (4.4) are $a_{\rm min} \approx 53$, 14, 7.5, and 3 Å.

In the model of Li & Draine (2001), stochastically heated grains exhibit strong spectral feature emission (i.e. PAHs) but have very weak continua (due to the low continuum opacities of small grains). Most dusty galaxies contain a significant amount of thermally heated $\bar{T} \gtrsim 100\,{\rm K}$ dust which emits more continuum radiation than these stochastically heated grains (see also Laor & Draine 1993). Thus, the continuum radiation from stochastically heated grains in our *cold* com-

ponent (i.e. grains with $a < 53\,\text{Å}$) is weak compared to the thermal emission from warmer dust. Additionally, since the threshold grain-size decreases as the magnitude of the illuminating radiation field energy density increases, stochastically heated continuum emission is even less important for grains in our *cool*, *warm*, and *hot* components. Since the stochastic continuum emission of all components is weak compared to the emission from thermally heated grains, and given that the stochastically heated feature emission attributed to PAHs is included in our model through the *PAHs* component, we do not incorporate a detailed model of stochastic heating (as presented in e.g. Greenberg & Hong 1974; Purcell 1976; Draine & Anderson 1985; Guhathakurta & Draine 1989; Draine & Li 2001).

4.5 Dust Emissivity

The total emissivity per hydrogen nucleon of a distribution of grains (in units of erg s^{-1} Hz^{-1} sr^{-1} H^{-1}) is obtained by summing over the emissivity of each grain species

$$E_\nu = E_\nu^{\text{gra}} + E_\nu^{\text{sil}}. \tag{4.5}$$

Here, the emissivities of graphite and silicate grains are

$$E_\nu^i = \int_{50\,\text{Å}}^{\infty} \frac{1}{n_{\text{H}}} \frac{dn_i}{da}\; C_{\text{abs}}^i(a,\lambda)\; B_\nu[T_{\text{eq}}^i(a,\tilde{\tilde{T}})]\, da, \tag{4.6}$$

which is an average over the individual emissivities of the grains in the distribution. Note that in contrast to models using a single effective grain-size, the dust emissivity in our adopted model is *not* directly proportional to the dust opacity (see §4.7), since the equilibrium grain temperatures in equation (4.6) depend upon grain-size and composition.

4.6 Characteristic Distribution Temperature

As discussed in §4.3, the many grains within a distribution are brought to different equilibrium temperatures through interactions with the radiation field in which they are embedded. In our decomposition method this distribution of equilibrium temperatures is determined from the fitted magnitude of the illuminating radiation field energy density, $\tilde{U}$. A given dust component therefore has many temperatures associated with it, none of which uniquely characterize the properties of the distribution. This is clearly not a desirable situation, as we would like to associate a single characteristic temperature to each value of $\tilde{U}$, preferably a temperature which communicates the position of the spectral peak of the resulting emission from the distribution. To meet this goal, we define the luminosity-weighted characteristic distribution temperature

$$\bar{T} \equiv \bar{T}(\tilde{U}) = \frac{\int_{50\,\text{Å}}^{\infty} \sum_i f_L^i(a,\tilde{U}) T_{\text{eq}}^i(a,\tilde{U})\, da}{\int_{50\,\text{Å}}^{\infty} \sum_i f_L^i(a,\tilde{U})\, da}, \tag{4.7}$$

where the sum is over the two grain compositions, and

$$f_L^i(a,\tilde{U}) = \frac{1}{n_{\text{H}}} \frac{dn_i}{da} \int C_{\text{abs}}^i(a,\nu) B_\nu[T_{\text{eq}}^i(a,\tilde{U})]\, d\nu \tag{4.8}$$

is the grain-luminosity distribution function (which is essentially the spectrally integrated emissivity of an individual grain—see §4.5). Note that the integration starts at $a = 50\,\text{Å}$, since smaller grains are not in thermal equilibrium.

Using this weighting function, $\bar{T}$ is properly interpreted as the composition-averaged temperature of the luminosity-dominating grain-size. With this definition, the emission peak from a distribution of grains occurs near the wavelength expected from the dust-modified Wien's law

$$\lambda_{\text{peak}} \approx \left(\frac{300\,\text{K}}{\bar{T}}\right) 10\,\mu\text{m}, \tag{4.9}$$

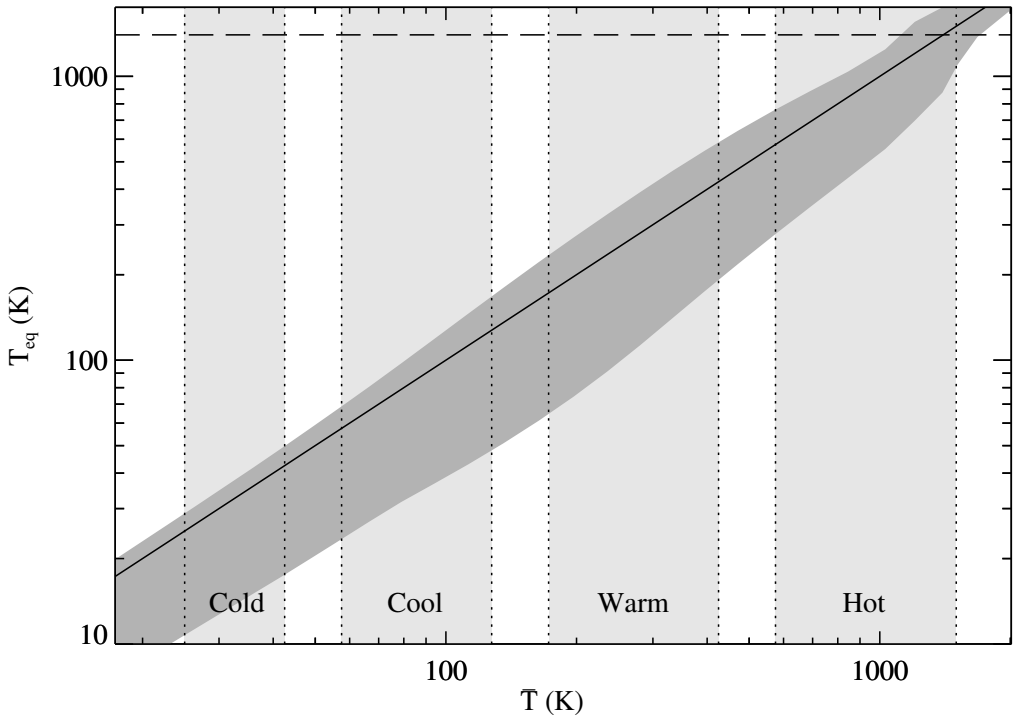

Figure 4.1 Range of equilibrium temperatures, $T_{\rm eq}$, of the grains within a distribution as a function of the characteristic distribution temperature $\bar{T}$. The dark shaded region shows the range of equilibrium temperatures within a given distribution (i.e. at a fixed value of $\bar{T}$), while the solid line shows their luminosity-weighted characteristic temperature. Light shaded regions indicate typical characteristic temperature ranges for the decomposition components. The sublimation temperature of silicates is also shown (*dashed line*).

where the peak is defined to occur at the wavelength coinciding with the maximum value of $E_\nu = \Sigma_{\rm abs} B_\nu(\bar{T})$ (i.e. the emissivity of a distribution in the limit in which the temperatures of its constituent grains are independent of their size and composition). Figure 4.1 shows the range of equilibrium temperatures, $T_{\rm eq}$, of the grains within a distribution for a given value of the characteristic distribution temperature, $\bar{T}$. The dark shaded region spans the range of equilibrium temperatures in a distribution, while the solid line shows the luminosity-weighted average over that distribution. Note that this average temperature is weighted towards

the warmer equilibrium temperatures since the grain-size distribution function is weighted towards smaller (i.e. warmer) grains. The light shaded regions indicate the typical ranges of the characteristic distribution temperatures for the dust components in our decomposition (i.e. as determined by the fitted values of $\tilde{U}$ for each component).

4.7 Dust Opacity

The total absorption opacity per hydrogen nucleon of a distribution of grains (in units of $\mathrm{cm}^2\ \mathrm{H}^{-1}$) is obtained by summing over the opacity of each grain species

$$\Sigma_{\mathrm{abs}}(\lambda) = \Sigma_{\mathrm{abs}}^{\mathrm{gra}}(\lambda) + \Sigma_{\mathrm{abs}}^{\mathrm{sil}}(\lambda). \tag{4.10}$$

Here, the opacities of graphite and silicate grains are

$$\Sigma_{\mathrm{abs}}^{i}(\lambda) = \int_{50\,\text{Å}}^{\infty} \frac{1}{n_{\mathrm{H}}} \frac{dn_i}{da} C_{\mathrm{abs}}^{i}(a,\lambda)\, da, \tag{4.11}$$

which is an average over the individual opacities of the grains in the distribution. The total extinction opacity per hydrogen nucleon, Σ_{ext}, is calculated in an analogous way with $C_{\mathrm{abs}} \rightarrow C_{\mathrm{ext}}$. According to Li & Draine (2001, Table 6), $\Sigma_{\mathrm{abs}} \propto \lambda^{-2}$ over the range $20\,\mu\mathrm{m} < \lambda < 700\,\mu\mathrm{m}$ and $\Sigma_{\mathrm{abs}} \propto \lambda^{-1.68}$ over the range $700\,\mu\mathrm{m} < \lambda < 10^4\,\mu\mathrm{m}$, to within $\pm 10\%$.

4.8 Water-Ice and HAC Opacity

Mid-IR spectra often exhibit 5.6–7.8 μm opacity produced from a combination of water-ice absorption near 6.1 μm (see e.g. Chiar et al. 2000; Gibb et al. 2000) and absorption from hydrogenated amorphous carbon (HAC) near 6.85 μm and 7.25 μm

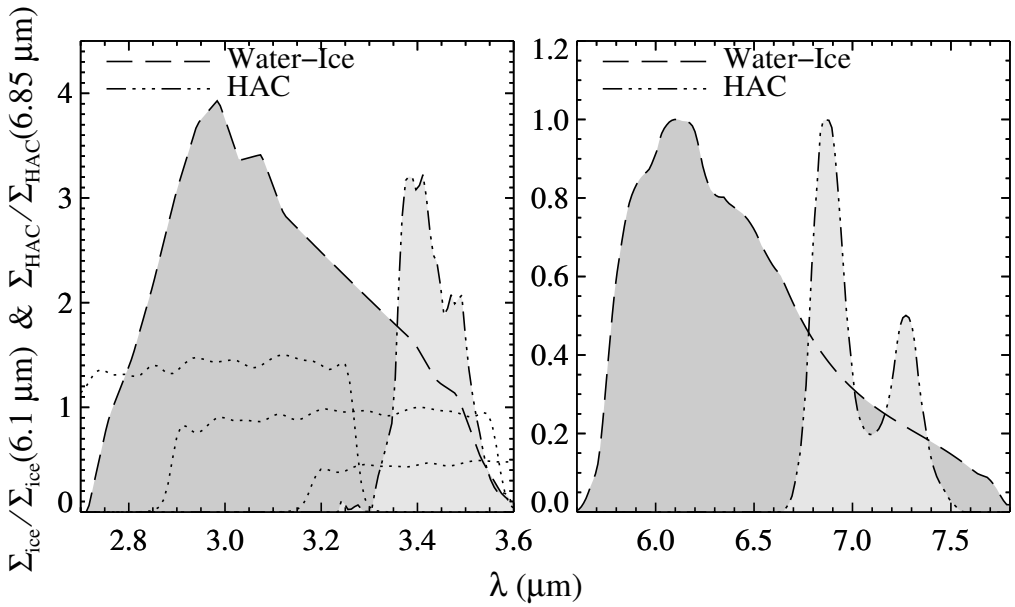

Figure 4.2 Water-ice and HAC opacity templates derived from L-band (Imanishi et al. 2006) and IRS (Spoon et al. 2004) spectra of ULIRGs (see text). Also shown in the left panel is the arbitrarily scaled IRAC 3.6 μm transmission curve for sources at $z = 0$, 0.1, and 0.2 (from right to left).

(Furton et al. 1999). Such water-ice and HAC absorption is particularly prominent in ULIRG spectra (e.g. Spoon et al. 2002). We derive 5.6–7.8 μm water-ice and HAC opacity templates from the IRS spectrum of the heavily obscured ULIRG IRAS F00183-7111 (Spoon et al. 2004). This high signal-to-noise spectrum exhibits strong water-ice and HAC absorption with very little PAH emission, thereby providing a clean spectrum from which to extract profiles of the various opacity sources. We fit a smooth spline to the observed spectrum between continuum points on either side of the water-ice and HAC features, and use the ratio of the observed spectrum to the estimated continuum to obtain the opacity templates displayed in the right-panel of Figure 4.2.

Additional opacity from 3.1 μm water-ice and 3.4 μm HAC features may significant affect the broadband photometry of some sources (see Fig. 4.2). We therefore

use the L-band spectra of ULIRGs presented in Imanishi et al. (2006) to derive opacity templates for these features to use in our decompositions. The opacities of the 3.1 μm water-ice and 3.4 μm HAC features are derived from spectra of the deeply obscured ULIRGs IRAS 00188-0856 and IRAS 08572+3915, respectively. Note that we do not derive the 6.1 μm water-ice template from the IRS spectrum of IRAS 00188-0856 since it is contaminated by 6.2 μm PAH emission. As measured from their L-band and IRS spectra, the water-ice features of IRAS 00188-0856 have apparent $\tau_{3.1}^{\rm ice}/\tau_{6.1}^{\rm ice} \approx 3.9$ while the HAC features of IRAS 08572+3915 have apparent $\tau_{3.4}^{\rm HAC}/\tau_{6.85}^{\rm HAC} \approx 3.3$. Our full opacity templates, shown in Figure 4.2, are constructed using these optical depth ratios to set the scalings between the 3.1–3.4 μm and 5.6–7.8 μm features.

4.9 Total Optical Depth

The total optical depth along a line-of-sight is the sum of the optical depths from each opacity source. Thus, in our case

$$\tau(\lambda) = \tau_{\rm dust}(\lambda) + \tau_{\rm ice}(\lambda) + \tau_{\rm HAC}(\lambda). \tag{4.12}$$

The optical depth through a column of dust having total absorption or extinction (depending on the situation) opacity $\Sigma(\lambda)$ is given by

$$\tau_{\rm dust}(\lambda) = N_{\rm H}\Sigma(\lambda) = \tilde{\tau}_{9.7}^{\rm dust}\frac{\Sigma(\lambda)}{\Sigma(9.7\,\mu{\rm m})}, \tag{4.13}$$

where $N_{\rm H}$ and $\tilde{\tau}_{9.7}^{\rm dust}$ are the hydrogen nucleon column density and 9.7 μm optical depth through the dust, respectively. The optical depth due to ice absorption is given by

$$\tau_{\rm ice}(\lambda) = \tilde{\eta}_{\rm ice}\tilde{\tau}_{9.7}^{\rm dust}\frac{\Sigma_{\rm ice}(\lambda)}{\Sigma_{\rm ice}(6.1\,\mu{\rm m})}, \tag{4.14}$$

where $\Sigma_{\rm ice}$ is the ice opacity template from Figure 4.2, and $\tilde{\eta}_{\rm ice} \equiv \tau_{6.1}^{\rm ice}/\tau_{9.7}^{\rm dust}$ determines the amount of ice opacity for a given dust opacity. Similarly, the optical depth due to HAC absorption is given by

$$\tau_{\rm HAC}(\lambda) = \tilde{\eta}_{\rm HAC}\tilde{\tau}_{9.7}^{\rm dust}\frac{\Sigma_{\rm HAC}(\lambda)}{\Sigma_{\rm HAC}(6.85\,\mu{\rm m})}, \tag{4.15}$$

where $\Sigma_{\rm HAC}$ is the HAC opacity template from Figure 4.2, and $\tilde{\eta}_{\rm HAC} \equiv \tau_{6.85}^{\rm HAC}/\tau_{9.7}^{\rm dust}$ determines the amount of HAC opacity for a given dust opacity. The ratios of the apparent $6.1\,\mu$m water-ice and $6.85\,\mu$m HAC optical depths to the apparent $9.7\,\mu$m silicate optical depth are both $\sim$0.1 for the various ULIRGs used to derive the opacity templates. We therefore restrict the fitted values of these ratios to satisfy $0 \leq \tilde{\eta}_{\rm ice} \leq 0.1$ and $0 \leq \tilde{\eta}_{\rm HAC} \leq 0.1$ in our decompositions.

Chapter 5

Dust Emission

5.1 Optically-Thin Dust Emission

Figure 5.1 presents an illustration of the optically-thin dust-shell approximation used to calculate the SEDs of emission from the dust components in our decomposition that are heated directly by ultraviolet and optical photons from the *SB* and *AGN* source components (see also Fig. 2.1). The left-panel depicts a starburst containing a *SB* source component surrounded by a shell of dust. The right-panel shows an AGN comprised of an *AGN* accretion disk, a dusty torus (either smooth or made of discrete clouds), and more distant narrow-line region clouds. In this geometry, ultraviolet and optical photons emitted by the source components either escape freely or are absorbed within shells of dust on the illuminated sides of clouds. By definition, these shells have an optical depth of order unity at the wavelength of peak energy absorption

$$\lambda_{\rm peak} = \frac{\int \Sigma_{\rm abs}(\lambda) u_\lambda \lambda \, d\lambda}{\int \Sigma_{\rm abs}(\lambda) u_\lambda \, d\lambda}. \tag{5.1}$$

Here, the absorption-weighted distribution function is obtained by integrating the energy absorbed by a single grain (i.e. the left-side of eq. [4.3]) over the distribution. As described in §4.3, we assume that grains in the *hot* component are heated by the *AGN* radiation field (Fig. 3.1), while grains in the other dust components are heated by the *ISRF* field. The peak absorption wavelengths from equation (5.1) for these fields are 1470 and 4550 Å, respectively. At these wavelengths, the dust absorption opacity is approximately 20 and 5 times greater than its value at 9.7 μm, so that the 9.7 μm optical depths of the thin dust shells illuminated by the *AGN*

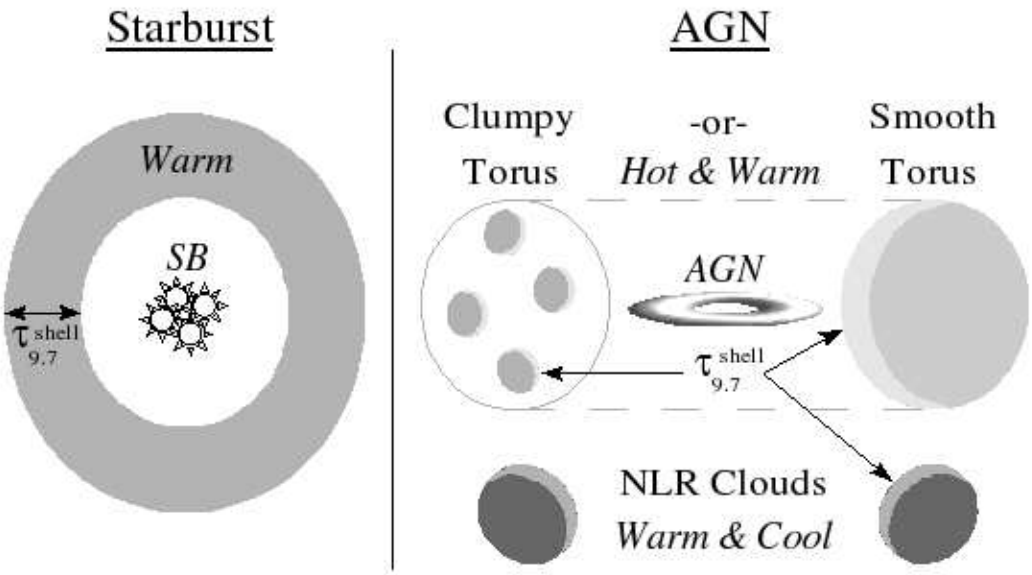

Figure 5.1 Cross-sectional views illustrating the optically-thin dust-shell approximation used to calculate the SEDs of dust components that are directly heated by ultraviolet and optical radiation from the *SB* and *AGN* source components (see text). The left-panel depicts a *SB* source component surrounded by a shell of dust. The right-panel shows an *AGN* accretion disk and torus (made either of discrete clouds as on the left *or* a smooth dust distribution as on the right), and more distant narrow-line region clouds.

and *ISRF* radiation fields are $\tau_{9.7}^{\rm shell} \approx 0.05$ and 0.2, respectively.

All emission from these shells therefore emerges from regions which are optically-thin at all infrared wavelengths (i.e. $\lambda \gtrsim 1\,\mu$m). As calculated from the radiative transfer equation, the emerging intensity from these shells is

$$I_\nu = \int_0^{\tau_{\rm shell}} S_\nu(\tau') e^{-[\tau_{\rm shell}-\tau']}\, d\tau' = \left[1 - e^{-\tau_{\rm shell}}\right] S_\nu. \qquad (5.2)$$

Here, the source function $S_\nu \equiv E_\nu/\Sigma_{\rm abs}$, is assumed to be constant (i.e. the magnitude of the radiation field energy density—and thus the dust temperature distribution—is assumed to be uniform). As shown above, $\tau_{\rm shell} < 1$ for all infrared

wavelengths, so that equation (5.2) simplifies to

$$I_\nu \approx N_{\rm H}^{\rm shell}\, E_\nu, \tag{5.3}$$

where $N_{\rm H}^{\rm shell}$ is the hydrogen nucleon column density (i.e. $\tau_{\rm shell} = N_{\rm H}^{\rm shell}\Sigma_{\rm abs}$).

5.2 *Hot* and *Warm* Component Emission

Using equation (5.3), the flux densities per unit frequency interval of emission from the *hot* and *warm* components are

$$f_\nu^{\rm hot} \propto E_\nu(\bar{T}_{\rm hot})e^{-\tau_{\rm hot}} \text{ and } f_\nu^{\rm warm} \propto E_\nu(\bar{T}_{\rm warm})e^{-\tau_{\rm warm}}, \tag{5.4}$$

where $\bar{T}_{\rm hot} = \bar{T}(\tilde{U}_{\rm hot})$ and $\bar{T}_{\rm warm} = \bar{T}(\tilde{U}_{\rm warm})$ are the characteristic component temperatures determined from the fitted values of $\tilde{U}_{\rm hot}$ and $\tilde{U}_{\rm warm}$ (see §4.6), and

$$\tau_{\rm hot} = \tilde{\tau}_{9.7}^{\rm hot}\frac{\Sigma_{\rm abs}(\lambda)}{\Sigma_{\rm abs}(9.7\,\mu{\rm m})} \text{ and } \tau_{\rm warm} = \tilde{\tau}_{9.7}^{\rm warm}\frac{\Sigma_{\rm abs}(\lambda)}{\Sigma_{\rm abs}(9.7\,\mu{\rm m})} \tag{5.5}$$

are the optical depths through the screens of dust obscuring the *hot* and *warm* components (e.g. provided by the *cool* and *cold* components in the geometry of Fig. 2.1). Here, $\tilde{\tau}_{9.7}^{\rm hot}$ and $\tilde{\tau}_{9.7}^{\rm warm}$ are the screen optical depths to the *hot* and *warm* components at $9.7\,\mu$m. Note that we use the absorption and not the extinction opacity since scattering is negligible for $\lambda \gtrsim 3\,\mu$m, where most dust emission (with the exception of the blue end of the *hot* component) is radiated. Example *hot* and *warm* component SEDs, $f_\nu^{\rm hot}$ and $f_\nu^{\rm warm}$, are shown in Figure 5.2 for the characteristic temperatures $\bar{T}_{\rm hot} = 1400\,{\rm K}$ and $\bar{T}_{\rm warm} = 200\,{\rm K}$. The fitted *hot* component characteristic temperature is constrained to satisfy $500\,{\rm K} < \bar{T}_{\rm hot} < 1500\,{\rm K}$ and the fitted *warm* component characteristic temperature typically satisfies $150\,{\rm K} < \bar{T}_{\rm warm} < 500\,{\rm K}$. Also shown in Figure 5.2 are example *hot* and *warm* component SEDs obscured by screens having $\tau_{9.7} = 1$, 2, and 3. Note that departures from a smooth continuum near 9.7 and $18\,\mu$m are caused by emission and absorption from silicates.

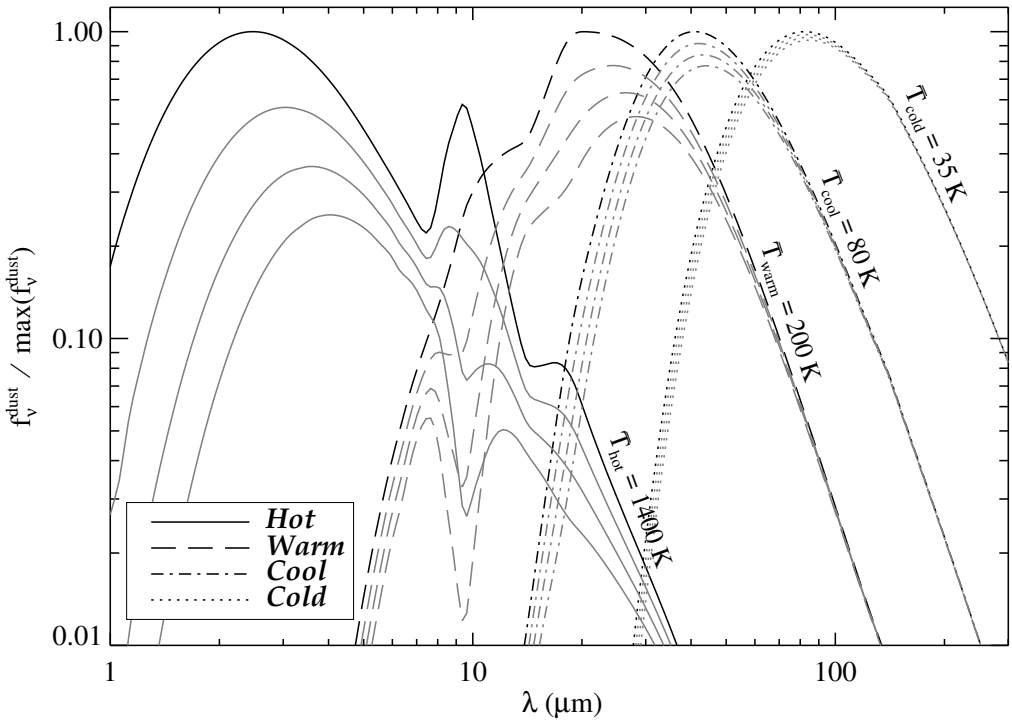

Figure 5.2 Example SEDs of emission from the *hot*, *warm*, *cool*, and *cold* dust components for typical characteristic temperatures of $\bar{T}$ = 1400, 200, 80, and 35 K (*black lines*). Also shown are the SEDs of dust obscured by screens (*gray lines*) having $\tau_{9.7} = 1$, 2, and 3 (top to bottom).

5.3 *Cool* and *Cold* Component Emission

In the geometry of Figure 2.1, dust in the *cool* and *cold* components may serve as sources of opacity to obscure the emission from other components. Given this geometry, and the observation that the mid-IR obscuration in dusty galaxies is often quite high (e.g. $\tau_{9.7} \approx 3$–5 for many of the local ULIRGs in Armus et al. 2006), the optically-thin approximation used to obtain equation (5.3) is not necessarily valid for the *cool* and *cold* components. However, as a result of their relatively cool characteristic temperatures and 40–100 μm SED peaks, the optical depth through these components at the wavelengths over which they emit strongly is a factor $\sim$10–30 times smaller than at 9.7 μm. Therefore, despite potentially large 9.7 μm

optical depths, both components are actually optically-thin at the wavelengths over which the majority of their emission is radiated. Thus, the conditions required for the validity of equation (5.3) are in fact still satisfied so that the flux densities per unit frequency interval of emission from the *cool* and *cold* dust components are

$$f_\nu^{\rm cool} \propto E_\nu(\bar{T}_{\rm cool}) \text{ and } f_\nu^{\rm cold} \propto E_\nu^{\rm cold}(\bar{T}_{\rm cold}), \tag{5.6}$$

where $\bar{T}_{\rm cool} = \bar{T}(\tilde{U}_{\rm cool})$ and $\bar{T}_{\rm cold} = \bar{T}(\tilde{U}_{\rm cold})$ are the characteristic component temperatures determined from the fitted values of $\tilde{U}_{\rm cool}$ and $\tilde{U}_{\rm cold}$. We assume that emission from both the *cool* and *cold* components emerges unextinguished since the optical depths required to achieve significant extinctions at $\lambda \gtrsim 50\,\mu$m would imply implausibly high optical depths at shorter wavelengths. Example *cool* and *cold* component SEDs, $f_\nu^{\rm cool}$ and $f_\nu^{\rm cold}$, are shown in Figure 5.2 for the characteristic temperatures $\bar{T}_{\rm cool} = 80\,{\rm K}$ and $\bar{T}_{\rm cold} = 35\,{\rm K}$. The fitted *cool* and *cold* component characteristic temperatures typically satisfy $50\,{\rm K} < \bar{T}_{\rm cool} < 100\,{\rm K}$ and $25\,{\rm K} < \bar{T}_{\rm cold} < 40\,{\rm K}$, respectively. Also shown in Figure 5.2 are the *cool* and *cold* SEDs obscured by screens having $\tau_{9.7} = 1$, 2, and 3, demonstrating that the obscured *cool* and *cold* component SEDs are changed very little.

5.4 Comparison with Other Methods

The emergent flux density from dust embedded in a distribution of radiation fields with energy densities U is

$$f_\nu^{\rm dust} \propto \int \frac{dM_{\rm dust}}{dU} E_\nu[\bar{T}(U)]\, dU. \tag{5.7}$$

Here, $M_{\rm dust}(U)$ is the mass of dust heated to the characteristic temperature $\bar{T}(U)$ by the field with strength U. Our four-component dust model characterizing the

emission from a galaxy is derived from equation (5.7) by taking

$$\frac{dM_{\rm dust}}{dU} = \sum_{i=1}^{4} M^i_{\rm dust}\delta(U - U_i), \tag{5.8}$$

where the sum is over four discrete values of U_i illuminating a mass $M^i_{\rm dust}$ of dust each. Clearly, equation (5.8) is an oversimplification of the true distribution of mass in a galaxy. Dale et al. (2001) and Li & Draine (2002) both calculate the integrated emission from dust in galaxies by assuming a power-law distribution of dust mass over heating intensity

$$\frac{dM_{\rm dust}}{dU} \propto U^{-\alpha}, \tag{5.9}$$

where α determines the relative contributions from each value of the radiation field energy density. Given a sufficient number of discrete temperature components, the model in equation (5.8) can be used to approximate the emission from the power-law model to arbitrary precision (with the appropriate weighting of each component through the $M^i_{\rm dust}$). The fact that both our multi-component model and these power-law models produce excellent fits to the integrated spectra of galaxies implies that the required "sufficient number" of discrete components postulated above must be approximately four.

The real power of our multi-component approach stems from the fact that it is capable not only of approximating the emission from the mass distribution of star-forming galaxies in equation (5.9), but also the emission from mass distributions which are *not* characterized by a power-law (since we do not make the geometrical assumptions concerning the distribution of dust within a galaxy implied by eq. [5.9]). For example, the composite emission from a galaxy containing both a starburst and an AGN may have a total mass distribution function dominated by a star-formation driven power-law at low energy densities superposed with an AGN driven power-law (having a different exponent) at high energy densities. Since the

sum of two power-laws with different exponents is not necessarily itself a power-law, a model such as equation (5.9) cannot properly model this scenario. This, coupled with the fact that our method allows us to fit for different levels of obscuration towards each component (as expected for physically distinct AGN and starburst regions), drives our decision to utilize the multi-component discrete temperature approach to describe the composite SEDs of dusty galaxies.

5.5 Dust Emission in Previous Publications

The decompositions of IRAS 10214+4724 in Teplitz et al. (2006), NGC 6240 in Armus et al. (2006), and the BGS sample of ULIRGs in Armus et al. (2007) were performed using an earlier version of the method described in this dissertation which utilized a different model to calculate the emission from each dust component. In these previous publications, dust emission is calculated from an optically thin shell of constant density material surrounding the illuminating source. As in equation (5.9), the dust in this shell is exposed to different radiation fields (depending on its distance from the central source), and is therefore brought to different equilibrium temperatures. In these previous works, we assume that the dust shells had thicknesses $r_{\rm out}/r_{\rm in} = 10$, which fixes the range of radiation fields and therefore dust temperatures, once the temperature at the minimum radius is defined (taken to be the sublimation temperature). Since each of these dust components contains a range of temperatures (from dust at different radii), only three components were needed to fit the sources instead of the four used in the current work. We choose to adopt the four-component method for this dissertation since it improves the fits at long wavelengths and simplifies the interpretation.

Chapter 6

PAH Emission

Observations with *ISO* and *Spitzer* have shown that the presence of PAHs (Leger & Puget 1984; Allamandola et al. 1985) can be used as an indicator of star-formation (e.g. Förster Schreiber et al. 2004; Peeters et al. 2004). We note, however, that Calzetti et al. (2005) find that PAH emission does not correlate well with other star-formation tracers in M 51. Additionally, Engelbracht et al. (2005) and Wu et al. (2006) find that PAH emission varies with metallicity, so may therefore not be a useful tracer of star-formation in low-metallicity systems. With these cautionary notes in mind, the presence or absence of PAH emission nevertheless provides an important clue to help distinguish between star-formation and accretion dominated ULIRGs (e.g. Genzel et al. 1998), thereby necessitating the development of a method to carefully decompose the contributions from PAHs to the total emission from dusty galaxies.

This process is complicated by the fact that it is difficult to establish the level of the continuum beneath the PAH features, especially in the presence of 9.7 μm silicate absorption. The method presented here provides a systematic means of estimating this continuum—and therefore the strength of the PAH features—without the need for the observer to define the continuum level by hand. We model the flux density per unit frequency interval of the *PAHs* component as

$$f_\nu^{\rm PAHs} = f_0^{\rm PAHs} \frac{\hat{f}_\nu^{\rm PAHs}}{\hat{f}_\nu^{\rm PAHs}(6.2\,\mu{\rm m})}, \tag{6.1}$$

where $f_0^{\rm PAHs} \equiv f_\nu^{\rm data}(6.2\,\mu{\rm m}) - f_\nu^{\rm cont}(6.2\,\mu{\rm m})$ is the estimated peak flux density of the 6.2 μm PAH feature obtained from the local continuum-subtracted observed

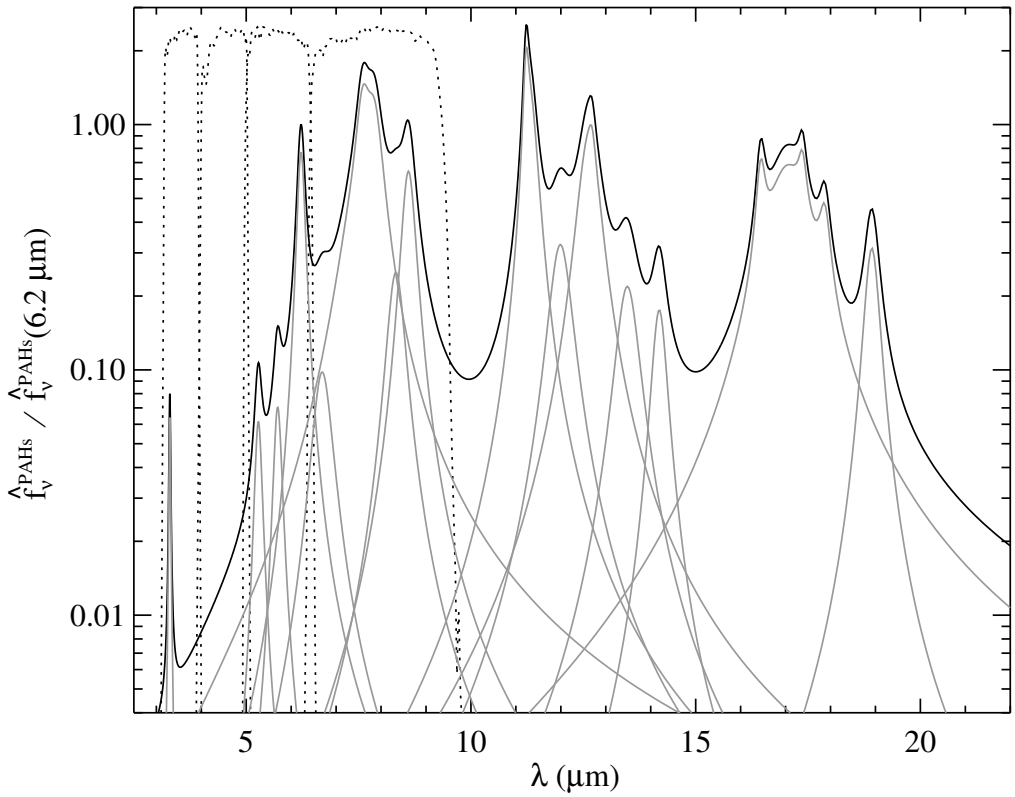

Figure 6.1 PAH emission template (*black line*) derived from the spectrum of the mean starburst galaxy from Brandl et al. (2006). The individual complexes (*gray lines*) are modeled with Drude profiles (see Smith et al. 2007). Note the significant "continuum" emission created by the addition of flux in the wings of the broad features. Also shown are the four arbitrarily scaled IRAC transmission curves.

spectrum, and

$$\hat{f}_\nu^{\rm PAHs} = \sum_i \frac{\gamma_i^2 f_{\nu,0}^i}{\left(\lambda/\lambda_0^i - \lambda_0^i/\lambda\right)^2 + \gamma_i^2} \tag{6.2}$$

is the PAH emission template shown in Figure 6.1 constructed by summing over a series of Drude profiles with the parameters presented in Table 6.1. As suggested by the definition of $f_0^{\rm PAHs}$, the overall strength of the PAH template is held fixed during the continuum fit, but the strengths of the individual features are allowed to vary in the subsequent PAH fit (see §2.1.1 and the following paragraph).

The central wavelengths and widths of our $\lambda_0 > 3.3\,\mu$m features are adapted

Table 6.1. PAH Template Parameters

Feature i	λ_0^i (μm)	γ_i (10^{-2})	$f_{\nu,0}^i$ (Jy)	$L_j / \sum_j L_j$ [a,b] (10^{-2})	Complex[c] j
1	3.30	1.2	0.07	0.6	1
2	5.27	3.4	0.06	1.0	2
3	5.70	3.5	0.07	1.1	3
4	6.22	3.0	0.77	9.7	4
5	6.69	7.0	0.10	2.7	5
6	7.42	12.6	0.24	39.3	6
7	7.60	4.4	0.89	–	–
8	7.85	5.3	0.86	–	–
9	8.33	5.0	0.25	3.9	7
10	8.61	3.9	0.65	7.6	8
11	11.23	1.2	1.29	11.3	9
12	11.33	3.2	1.04	–	–
13	11.99	4.5	0.32	3.2	10
14	12.62	4.2	0.85	7.9	11
15	12.69	1.3	0.19	–	–
16	13.48	4.0	0.22	1.7	12
17	14.19	2.5	0.18	0.8	13
18	16.45	1.4	0.43	8.4	14
19	17.04	6.5	0.64	–	–
20	17.38	1.2	0.29	–	–
21	17.87	1.6	0.26	–	–
22	18.92	1.9	0.31	0.8	15

[a]Fraction of total PAH luminosity emerging from each complex j.

[b]$L_j = \sum_{i \in j} L_i$ is the total luminosity of a complex of Drude profiles, where $L_i = 4\pi D_L^2 (\pi/2) \lambda_0^i \gamma_i f_{\lambda,0}^i$ is the apparent total luminosity of a single profile, with D_L the luminosity distance to the source.

[c]As defined in Smith et al. (2007), the 7.7, 11.3, 12.7, and 17 μm complexes are each composed of multiple Drude profiles.

from those used in the analysis of Smith et al. (2007), and their relative strengths are derived using PAHFIT[1] to fit the low obscuration ($\tau_{9.7} \approx 0.24$) mean starburst galaxy spectrum created from 13 IRS spectra in Brandl et al. (2006). The 3.3 μm PAH feature central wavelength and width are obtained from Li & Draine (2001), and the peak flux density of this feature is derived from the ratio of the strengths of the PAH features at 3.3 and 6.2 μm in the L-band and IRS spectra of the star-

[1]See http://turtle.as.arizona.edu/jdsmith/pahfit.php.

forming ULIRG IRAS 12112+0305 presented in Imanishi et al. (2006) and Armus et al. (2006). We include this 3.3 μm PAH feature so that its contribution to the integrated L-band (or IRAC 3.6 μm channel—see Fig. 6.1) flux density is explicitly included in the fitting method. As described in §2.1.1, after fitting the continuum, we fit the continuum-subtracted observed spectrum to refine our *PAHs* component (the properties of which are held fixed during the continuum fit). In this fit, the central wavelengths and FWHM of the PAH features are fixed to the values in Table 6.1, and the peaks are allowed to vary freely. This fit provides accurate luminosities for all PAH complexes, as well as error estimates derived from the full covariance matrix.

Chapter 7

Atomic and Molecular Line Emission

In order to accurately fit the continuum and PAH features in an IRS spectrum, the contributions from atomic and molecular lines must be properly fit as well. Of course, the strength of these lines is scientifically interesting, but we caution against using our decomposition method to measure them since the fitted continuum around each line is not necessarily as accurate as one estimated by hand (a statement which cannot be made concerning the underlying continuum beneath PAH features). Therefore, although we obtain integrated flux values for the lines we fit, we do not recommend using these measurements for scientific purposes (at least not without carefully checking the validity of the fitted local continuum around each line). The one caveat to this recommendation where we do suggest using the fitted integrated line flux is for the [Ne II] 12.81 μm line, which our decomposition method is capable of deblending from the 12.7 μm PAH complex in low-resolution IRS spectra.

We create our atomic and molecular emission line spectrum by estimating the peak flux density of each line in Table 7.1 from the local continuum-subtracted IRS spectrum. The flux density per unit frequency interval of the *lines* component is modeled as a sum over unresolved Gaussian profiles having central wavelengths λ_0, widths γ_i, and peak flux densities $f_{\nu,0}$

$$f_\nu^{\rm lines} = \sum_i f_{\nu,0}^i \exp\left[-\frac{1}{2}\left(\frac{\lambda-\lambda_0^i}{\lambda_0^i\gamma_i/(2\sqrt{2\ln 2})}\right)^2\right]. \quad (7.1)$$

Since the Gaussian profiles are unresolved, the width of each line is a function of the IRS module in which it is detected (see Table 7.1 for values of γ as a function of source redshift). As described in §6 for the *PAHs* component, after fitting the

Table 7.1. Atomic and Molecular Line Parameters

i	Line	λ_0^i (μm)	$\gamma_i^{z=0}$ (10^{-2})	$\gamma_i^{z=0.1}$ (10^{-2})	$\gamma_i^{z=0.25}$ (10^{-2})	$\gamma_i^{z=0.5}$ (10^{-2})
1	$H_2S(8)$	5.053	···	6.0	6.0	12.1
2	[Fe II]	5.340	6.0	6.0	6.0	12.1
3	$H_2S(7)$	5.511	6.0	6.0	6.0	12.1
4	[Fe II]	5.674	6.0	6.0	6.0	12.
5	$H_2S(6)$	6.109	6.0	6.0	12.1	12.1
6	[Fe II]	6.721	6.0	6.0	12.1	12.1
7	$H_2S(5)$	6.910	6.0	12.1	12.1	12.1
8	[Ar II]	6.985	6.0	12.1	12.1	12.1
9	[Ne VI]	7.652	12.1	12.1	12.1	12.1
10	$H_2S(4)$	8.025	12.1	12.1	12.1	12.1
11	[Ar III]	8.991	12.1	12.1	12.1	12.1
12	$H_2S(3)$	9.665	12.1	12.1	12.1	16.9
13	[S IV]	10.511	12.1	12.1	12.1	16.9
14	$H_2S(2)$	12.279	12.1	12.1	16.9	16.9
15	[Ne II]	12.814	12.1	12.1	16.9	16.9
16	[Ne V]	14.322	16.9	16.9	16.9	33.9
17	[Ne III]	15.555	16.9	16.9	22.3	33.9
18	$H_2S(1)$	17.035	16.9	16.9	33.9	33.9
19	[S III]	18.713	16.9	33.9	33.9	33.9
20	[Ne V]	24.317	33.9	33.9	33.9	33.9
21	[O IV]	25.890	33.9	33.9	33.9	···
22	$H_2S(0)$	28.219	33.9	33.9	33.9	···
23	[S III]	33.481	33.9	33.9	···	···
24	[Si II]	34.815	33.9	···	···	···
25	[Ne III]	36.014	33.9	···	···	···

Note. — The FWHM = $\lambda_0^i \gamma_i$ of a particular atomic or molecular line is a function of the IRS module in which it is detected, and therefore depends on the redshift of the source. We give example values of γ_i for all lines at $z = 0$, 0.1, 0.25 and 0.5. Values of γ_i are not given for lines that fall out of the IRS wavelength range at a given redshift.

continuum we perform a fit to the continuum-subtracted observed spectrum in order to refine the *lines* component (the parameters for which are held fixed in the continuum fit). In this fit, the central wavelengths and FWHM of the atomic and molecular emission lines are fixed to the values in Table 7.1, and their peak flux densities are allowed to range freely.

Chapter 8

Constructing Dusty Galaxy SEDs

The dusty galaxy SEDs presented in this dissertation were observed as part of the *Spitzer* GTO programs to obtain mid-IR spectra of nearby starburst galaxies, AGNs, and ULIRGs. There are a total of 108 galaxies in our sample, which we divide into two groups. The first group contains six galaxies (hereafter called the "template sample"), which serve as template sources for the detailed case studies presented in §9 and §10. Details of the decompositions of the second group containing the remaining galaxies are presented in Appendices C–H, and analysis of the combined results from the entire sample are presented in §11.

8.1 Sample Selection

Table 8.1 presents a summary of the six galaxies in our template sample. They have been selected in order to demonstrate the capabilities of our decomposition method on a variety of dusty galaxy SEDs which are representative of the diverse properties of the group. We include examples of unextinguished and obscured starbursts (NGC 7714 and NGC 2623), a quasar (PG 0804+761), a Seyfert 2 (Mrk 463), and two composite systems (NGC 6240 and Mrk 1014) powered by both AGN and starburst activity (see §10 for details about each source). The first four galaxies in this sample serve as templates to aid in understanding the properties of the components from which composite systems are built.

Our sample includes star-forming galaxies covering a range of infrared luminosities—from a minimum $L_{\rm IR} \approx 5 \times 10^{10}\,L_{\odot}$ for NGC 7714 to more than a fac-

Table 8.1. Dusty Galaxy Properties

Galaxy	z	D_L (Mpc)	Class	Reference
NGC 7714	0.009	39	Starburst	1,2
NGC 2623	0.018	78	Obscured Starburst	2
PG 0804+761	0.130	610	Quasar	5
Mrk 463	0.050	222	Seyfert 2	4
NGC 6240	0.024	105	Starburst+AGN	3
Mrk 1014	0.163	781	Quasar+Starburst	4

References. — [1] Brandl et al. (2004); [2] Brandl et al. (2006); [3] Armus et al. (2006); [4] Armus et al. (2004); [5] Hao et al. (2005a).

Note. — The IRS spectra of the first three sources are from *Spitzer* program 14, and the spectra of the last three are from *Spitzer* program 105. Luminosity distances are calculated assuming a flat ΛCDM cosmology with $H_0 = 70$ km s^{-1} Mpc^{-1}, $\Omega_M = 0.3$, and $\Omega_\Lambda = 0.7$.

tor ∼10 higher for NGC 6240. In Table 8.2, we present a summary of the properties of the remaining 102 sources in our sample. While it is true that this sample does not include examples of "normal" star-forming galaxies, our decomposition method is nonetheless valid for these sources as well. In fact, our method is applicable to *all* galaxies—including AGNs, starbursts, normal, dwarfs, and ellipticals—so long as their SEDs are composed of emission from stars, dust, PAHs, atomic and molecular lines, and possibly an AGN accretion disk (i.e. our decomposition components).

8.2 IRS Spectroscopy

The IRS spectra of the sources in our template sample were first presented in the papers referred to in Table 8.1 (most of the spectra of the sources in the complete sample are unpublished elsewhere). All spectra in this dissertation have been extracted using the method described in Armus et al. (2006). In brief, the

IRS pipeline at the Spitzer Science Center was used to reduce the data, and one-dimensional spectra were extracted using the SMART package (Higdon et al. 2004). After scaling and stitching the individual orders together, each spectrum was scaled to match the MIPS 24 μm flux density (if available—see §8.4) or the *IRAS* 25 μm flux density.

8.3 Supplementary Photometry

The spectral coverage of the IRS low-resolution modules ends at an observed-frame wavelength of $\sim$38 μm. Emission from typical *cool* component dust ($\bar{T} \sim 80\,\mathrm{K}$) therefore only contributes to the last few microns, while emission from typical *cold* component dust ($\bar{T} \sim 35\,\mathrm{K}$) contributes negligibly at IRS wavelengths. To better constrain these cooler components which dominate the dust mass and frequently provide $\sim$50% of the total dust luminosity, we supplement our IRS spectra with far-IR to millimeter wavelength photometry from the literature. Furthermore, the spectral coverage of the IRS modules begins at an observed-frame wavelength of $\sim$5.2 μm. As seen in Figure 3.1, our source components all radiate significantly at shorter wavelengths. Thus, to better constrain these components, we supplement our SEDs with ultraviolet to near-IR photometry from the literature (obtained via NED[1]). Table 8.3 provides literature references for all photometry used in our template sample decompositions (see NED for photometric references for other sources in the complete sample).

[1] http://nedwww.ipac.caltech.edu/

Table 8.2. Complete Dusty Galaxy Sample

Galaxy	z	D_L (Mpc)	Class
Starburst Sample			
IC 342	0.0001	0.4	SB
Mrk 266	0.0278	122	SB+Sy2
NGC 520	0.0035	15	SB
NGC 660	0.0028	12	SB+LINER
NGC 1097	0.0364	160	SB+Sy1
NGC 1222	0.0082	35	SB
NGC 1365	0.0175	76	SB+Sy2
NGC 1614	0.0159	69	SB
NGC 2146	0.003	13	SB
NGC 3079	0.0037	16	Sy2
NGC 3310	0.0033	14	SB
NGC 3556	0.0033	14	SB
NGC 3628	0.0028	12	SB+LINER
NGC 4194	0.0084	36	SB
NGC 4676	0.022	96	SB
NGC 4818	0.0035	15	SB
NGC 4945	0.0035	15	SB+Sy2
NGC 7252	0.0156	68	SB
NGC 7469	0.0163	71	Sy1
AGN Sample			
PG 1119+120	0.0502	223	Sy1
PG 1211+143	0.0808	367	Sy1
PG 1351+640	0.0881	402	QSO
PG 2130+099	0.0621	278	Sy1
IZw1	0.0611	274	Sy1
ULIRG Sample			
F00183-7111	0.327	1710	LINER
00188-0856	0.128	603	SB+LINER
00199-7426	0.0963	442	SB
00275-0044	0.242	1210	···
00275-2859	0.279	1430	SB+Sy1
00397-1312	0.262	1330	HII
00406-3127	0.342	1810	Sy2
01003-2238	0.118	548	SB+Sy2
01199-2307	0.156	744	HII
01298-0744	0.136	641	SB
01388-4618	0.0902	412	HII
01494-1845	0.158	754	SB
03158+4227	0.134	632	Sy2
03538-6432	0.301	1560	···
04114-5117	0.124	582	···

Table 8.2 (cont'd)

Galaxy	z	D_L (Mpc)	Class
05189-2524	0.0425	188	Sy2
06009-7716	0.117	544	···
06035-7102	0.0794	360	SB
06206-6315	0.0924	423	SB+Sy2
06301-7934	0.156	746	···
06361-6217	0.16	765	SB+LINER
07598+6508	0.149	706	SB+Sy1
F08208+3211	0.396	2140	···
08572+3915	0.0583	261	LINER
09022-3615	0.0596	267	···
09104+4109	0.442	2440	Sy2
09463+8141	0.155	737	LINER
F10156+3705	0.49	2760	···
10378+1109	0.136	641	LINER
F10398+3247	0.633	3760	···
10565+2448	0.0431	191	HII
F11038+3217	0.13	610	···
11095-0238	0.107	493	LINER
11582+3020	0.223	1110	LINER
12018+1941	0.169	810	LINER
12032+1707	0.217	1070	LINER
12071-0444	0.128	602	Sy2
12112+0305	0.0726	328	LINER
12205+3356	0.263	1330	···
13120-5453	0.0307	135	···
13342+3932	0.179	867	Sy1
13352+6402	0.236	1180	···
13451+1232	0.122	569	Sy2
14348-1447	0.0827	376	LINER
14378-3651	0.0676	304	Sy2
F14548+3349	0.443	2450	Sy2
15206+3342	0.124	581	HII
15250+3609	0.0553	247	LINER
15462-0450	0.0997	459	Sy1
16090-0139	0.133	628	LINER
F16124+3241	0.71	4330	···
16334+4630	0.191	930	LINER
17068+4027	0.179	866	HII
17179+5444	0.147	700	Sy2
17208-0014	0.043	190	SB
17463+5806	0.309	1610	Sy2
18030+0705	0.146	691	···
18443+7433	0.135	634	···
19254-7245	0.0617	277	Sy2
19297-0406	0.0857	391	HII

Table 8.2 (cont'd)

Galaxy	z	D_L (Mpc)	Class
19458+0944	0.0999	460	···
20087-0308	0.106	488	LINER
20100-4156	0.13	608	SB
20414-1651	0.087	397	SB+LINER
20551-4250	0.0426	188	HII
21272+2514	0.151	717	···
22491-1808	0.0772	350	HII
23128-5919	0.0446	198	SB+Sy2
23129+2548	0.179	866	LINER
23230-6926	0.106	491	SB+LINER
23365+3604	0.0644	289	LINER
23498+2423	0.212	1050	Sy2
Arp 220	0.0181	79	SB+LINER
Mrk 231	0.0421	186	Sy1
Mrk 273	0.0378	167	Sy2
UGC 5101	0.04	177	LINER

Note. — Properties of the complete sample of dusty galaxies analyzed in this dissertation. The indicated galaxy classifications (SB = Starburst) are from NED.

In each wavelength range, we construct our SEDs using data which most closely samples the spatial region contained within the IRS slits. We treat photometric points that sample larger spatial regions (i.e. for wavelength ranges where no data at a similar spatial resolution is available in the literature) as upper-limits to the flux density of the area covered by the IRS spectrum. To include such a limit as input to the χ^2 fitting routine, we assign the data to have an upper-limit flux density $f_\nu^\downarrow = 0$ and an uncertainty $\sigma_\downarrow = f_\nu^{\rm data}/\xi$. Here, ξ determines the weighting of the limit in the fit, which we take to be $\xi = 3/2$. If, in addition to an upper-limit to the flux density contained in the IRS slit, we also have an estimate of the lower-limit (e.g. as estimated using a small aperture measurement), we assign the point to have a flux density of $f_\nu^\updownarrow = (f_\nu^\downarrow + f_\nu^\uparrow)/2$ with an uncertainty of $\sigma_\updownarrow = (f_\nu^\uparrow - f_\nu^\updownarrow)/\xi$, so that the fit is constrained to fall between these two values.

Table 8.3. Sample Supplementary Photometry

Galaxy	Ultraviolet	Optical	Near-IR	Far-IR	Sub-mm
NGC 7714	1	5	5	12,13	13,17
NGC 2623	2	6	9	12	17,18
PG 0804+761	3	3	10,11	14,15	···
Mrk 463	1	7	10	14,16	···
NGC 6240	4	8	9	12,16	16,18
Mrk 1014	3	7	9	14,15	···

References. — [1] Kinney et al. (1993); [2] GALEX (2006); [3] Baskin & Laor (2005); [4] Smith et al. (1992); [5] Lançon et al. (2001); [6] Taylor et al. (2005); [7] Surace & Sanders (2000); [8] de Vaucouleurs et al. (1991); [9] Scoville et al. (2000); [10] 2MASS PSC; [11] Neugebauer et al. (1987); [12] Sanders et al. (2003); [13] Krugel et al. (1998); [14] Moshir & et al. (1990); [15] Haas et al. (2003); [16] Klaas et al. (2001); [17] Dunne et al. (2000); [18] Benford (1999).

8.4 IRAC and MIPS Photometry

All of the source components and the *hot* dust component radiate significantly from 3–5 μm—i.e. between the JHK bands and the onset of the IRS spectral range (see Figs. 3.2 and 5.2). To better constrain the fits in this critical region, we derive observed-frame 3.6 and 4.5 μm nuclear flux densities of the central point-source for all galaxies in our sample with available Infrared Array Camera (IRAC) images (either archival or via our *Spitzer* program 30076). The IRAC images available for our template sample are shown in Figure 8.1, and the images for the complete sample are presented in Appendices F–H. Photometry for our template sample is presented in Table 8.4, calculated using the post-BCD products provided by the Spitzer Science Center. Photometric values for the rest of the sample are provided with their images in the Appendices. Flux densities for NGC 7714, NGC 2623, and NGC 6240 are calculated using a 5″ radius circular aperture to match both the near-IR literature photometry and the IRS slit-width. We do not apply any point-

source aperture corrections for these sources since they are all extended at these wavelengths. Mrk 1014 and Mrk 463 are both point-like at these wavelengths, so we calculate their flux densities using a 12.2″ radius aperture, which requires no aperture correction to recover the full point-source value. Photometry for the rest of the sources in our complete sample is calculated by integrating the flux within a 2.4″ radius aperture, and applying aperture corrections of 1.348 and 1.362 for channels 1 and 2, which we derive from the Mrk 1014 images. Since the contribution from extended emission is uncertain, we treat the aperture corrected IRAC values as upper-limits to the flux density, and the uncorrected values as lower-limits. Uncertainties are estimated to be 5–10%.

The *IRAS* and *ISO* beam-sizes are both much larger than the 5–11″ IRS slits, so that far-IR photometry of nearby extended sources contains emission from regions outside the slits. We therefore derive mid-IR and far-IR nuclear flux densities of the central point-sources for all galaxies in our sample from available Multiband Imaging Photometer for Spitzer (MIPS) images (obtained from the *Spitzer* archive or our GTO program 30073). The available MIPS images for galaxies in our template sample are shown in Figure 8.1, and all available images for the entire dusty galaxy sample are presented in Appendices F–H. We use the post-BCD products provided by the Spitzer Science Center to derive photometry for the template sample, presented in Table 8.4. Photometric values for the complete sample are presented with their images in the Appendices. We use Mrk 463 to derive aperture corrections since it is well-detected in all three bands and appears very point-like. To calculate the nuclear flux densities, we measure the emission from each source within small apertures (3″, 8″, and 20″ radii at 24, 70, and 160 μm), and scale these values by the appropriate aperture correction (3.37, 4.09, and 2.95 for 24, 70, and 160 μm). The *Spitzer* beam-sizes at 24, 70, and 160 μm

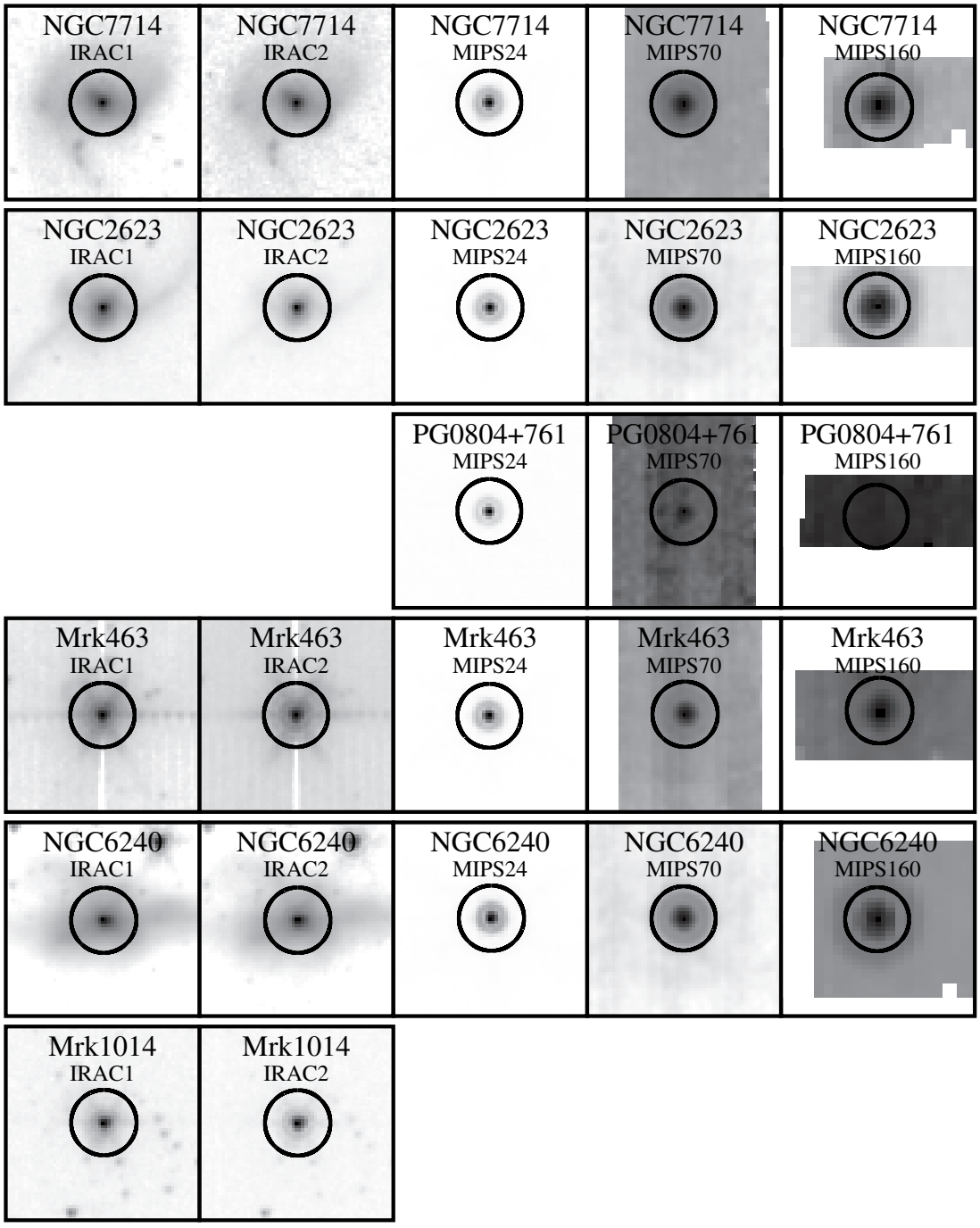

Figure 8.1 IRAC 3.6 and 4.5 μm (channels 1 and 2) and MIPS 24, 70 and 160 μm images for the dusty galaxies in our template sample.

Table 8.4. IRAC and MIPS Nuclear Photometry

		IRAC		MIPS		
Galaxy	PID	3.6 (mJy)	4.5 (mJy)	24 (Jy)	70 (Jy)	160 (Jy)
NGC 7714	59	17.0	13.5	1.96	6.67	4.64
NGC 2623	32	11.8	13.5	1.33	16.4	7.56
PG 0804+761	49	···	···	0.19	0.11	0.033
Mrk 463	32	115	156	1.50	1.90	0.89
NGC 6240	32,3672	33.7	46.0	2.71	14.7	9.08
Mrk 1014	32	19.2	23.2	···	···	···

Note. — IRAC flux density errors are estimated to be 5–10%. MIPS flux density errors are driven by the post-BCD calibration uncertainties and are ∼10% for the 24 μm band and ∼20% for the 70 and 160 μm bands. No color corrections are applied since they are much smaller than the uncertainties. The PID are the *Spitzer* program numbers for the IRAC and MIPS observations.

are ∼6″, 17″, and 39″. The 24 μm beam is therefore similar to the 5–11″ IRS slits, justifying scaling the IRS spectrum to this MIPS point. The beams at 70 μm and 160 μm are significantly smaller than the $> 100''$ *IRAS* and *ISO* beams. MIPS data therefore provides a much better estimate of the nuclear flux density. Flux density errors are dominated by the post-BCD calibration uncertainties and are estimated to be 10% at 24 μm and 20% at 70 and 160 μm. No color corrections are applied to the IRAC or MIPS photometry since all corrections are much smaller than the uncertainties.

Chapter 9

Decomposing Dusty Galaxies

9.1 Spectral Decomposition Results

In Figures 9.1–9.7, we present our decompositions of the *nuclear* SEDs of the dusty galaxies in our template sample. In these fits, the MIPS photometric points are used to constrain the nuclear far-IR SEDs, while the globally integrated *IRAS*, *ISO*, and sub-mm data provide upper-limits to this nuclear emission. The entire ultraviolet to millimeter wavelength SEDs are presented in Figure 9.1 and the upper-panels of Figures 9.3–9.7, and enlarged views focusing on the IRS regions are shown in Figure 9.2 and the lower-panels of Figures 9.3–9.7. In the figures displaying the full wavelength range, we also show the *global* fitted flux densities obtained using the full values of the large-beam *IRAS*, *ISO*, MIPS160, and sub-mm data. The temperatures of the *cold* and *cool* dust components obtained in the global fits are held fixed to these values in the nuclear decompositions. The decompositions of the complete sample of galaxies are presented in Appendices C–E. Note that the *ISRF* component contributes minimally in these nuclear decompositions since the small-aperture near-IR photometry used to match the IRS slits is dominated by emission from young stellar populations and not evolved stars.

9.2 Decomposition Parameters and Constraints

Example decomposition parameters obtained from the fits to the nuclear SEDs of the dusty galaxies in our template sample are presented in Tables 9.1 and 9.2.

Table 9.1. Sample Nuclear SED Decomposition Parameters

Galaxy	χ^2/dof[a]	dof[a]	$\bar{T}_{\rm cold}$[b] (K)	$\bar{T}_{\rm cool}$[b] (K)	$\bar{T}_{\rm warm}$[b] (K)	$\bar{T}_{\rm hot}$[b] (K)	$\tilde{\tau}_{9.7}^{\rm warm}$[c]	$\tilde{\tau}_{9.7}^{\rm hot}$[c]	$\tilde{\tau}_V^{\rm SB}$[d]	$\tilde{\epsilon}_{\rm AGN}$[e]	$\tilde{\eta}_{\rm ice}$[f]	$\tilde{\eta}_{\rm HAC}$[f]
NGC 7714	1.33	382	31	71	165	···	0.19	···	0.97	···	0	0
			±1	±1	±1	···	±0.03	···	±0.02	···	···	···
NGC 2623	2.46	383	29	53	206	···	3.52	···	4.81	···	0.1	0.1
			±1	±1	±1	···	±0.06	···	±0.11	···	···	···
PG 0804+761	2.77	363	42	150	400	1410	0.78	1.22	0	0.25	0.050	0.044
			±2	±6	±3	±10	±0.01	±0.03	···	±0.01	±0.012	±0.035
Mrk 463	1.90	364	30	55	211	1130	1.30	2.06	1.12	1	0.012	0.062
			±2	±2	±1	±6	±0.05	±0.01	±0.26	···	±0.004	±0.009
NGC 6240	1.77	369	29	61	193	1260	3.64	0	4.68	1	0.067	0.1
			±1	±1	±1	±30	±0.07	···	±0.08	···	±0.007	···
Mrk 1014	2.00	362	31	71	195	1500	0.14	2.70	5	0.49	0.031	0.1
			±1	±1	±1	···	±0.02	±0.04	···	±0.01	±0.005	···

[a]Total weighted reduced χ^2 value (see eqs. [2.2] and [2.3]) for the indicated number of degrees of freedom (dof).

[b]Characteristic dust temperature (see §4.3) determined from the fitted value of the magnitude of the illuminating radiation field energy density, $\tilde{U}_i$.

[c]9.7 μm optical depth through the screen obscuring the *warm* and *hot* dust components (see eqs. [5.4]).

[d]V-band (5500 Å) optical depth through the screen obscuring the *SB* source component (see eqs. [3.3] and [3.4]).

[e]Fraction of the *AGN* source component covered by the obscuring screen (see eq. [3.6]).

[f]Ratio of the 6.1 μm water-ice and 6.85 μm HAC optical depths to the 9.7 μm optical depth of each dust component (see eqs. [4.14] and [4.15]).

Note. — Formal statistical uncertainties are given beneath each parameter value. If none is given, the corresponding parameter was pegged at a limiting value. The 5500 Å optical depth to the *AGN* component is fixed to $\tilde{\tau}_V^{\rm AGN} = 25$.

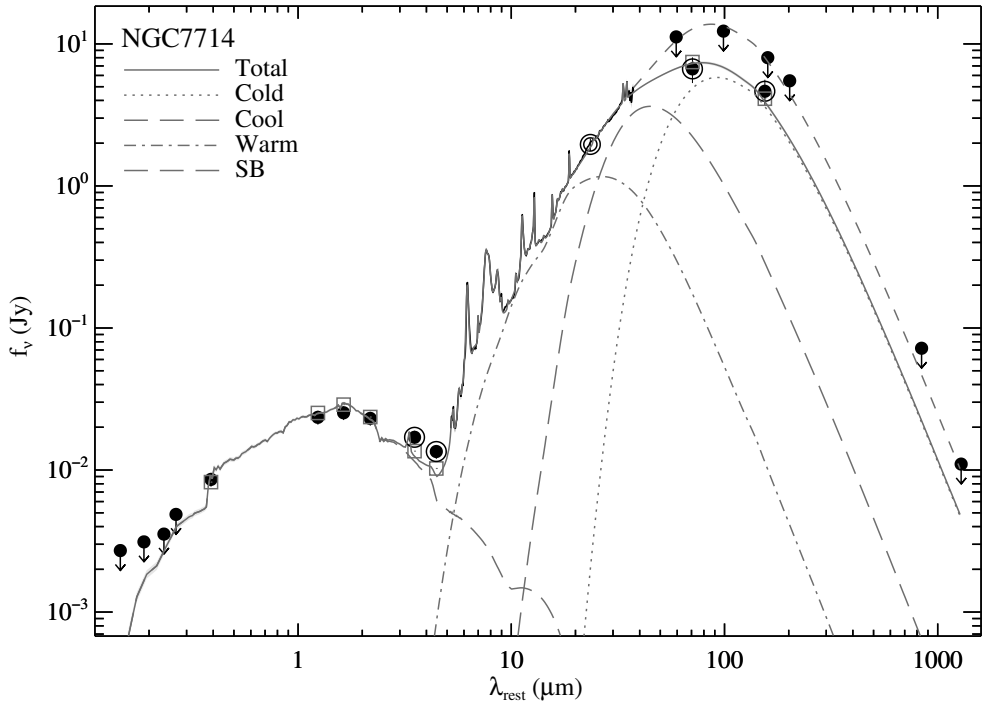

Figure 9.1 Spectral decomposition of the ultraviolet to millimeter wavelength SED (*black solid lines* and *filled circles*) of the nuclear region of the starburst galaxy NGC 7714. Arrows indicate upper or lower-limits (see §8.3). The unfilled symbol indicates the position of the MIPS 24 μm point to which the IRS spectrum is scaled. IRAC and MIPS photometric points are circled. The various decomposition components are shown as indicated in the figure legend. Additionally, the total fitted SED obtained using the globally integrated far-IR data (*dashed "Total" line*) is displayed.

There are a total of 17 free parameters in a decomposition. The *SB* source component has two free parameters: $\tilde{\alpha}_{\rm SB}$ and $\tilde{\tau}_V^{\rm SB}$ determine the fractional *SB* contribution to the total luminosity (see eq. [2.1]) and the 5500 Å optical depth (see eq. [3.3]). The *ISRF* source component has only a single free parameter: $\tilde{\alpha}_{\rm ISRF}$ (see eq. [3.2]). The *AGN* source component has a total of two free parameters: $\tilde{\alpha}_{\rm AGN}$ and $\tilde{\epsilon}_{\rm AGN}$, where the latter determines the fraction of the *AGN* component covered by the obscuring screen (see eq. [3.6]). The optical depth through the obscuring clouds

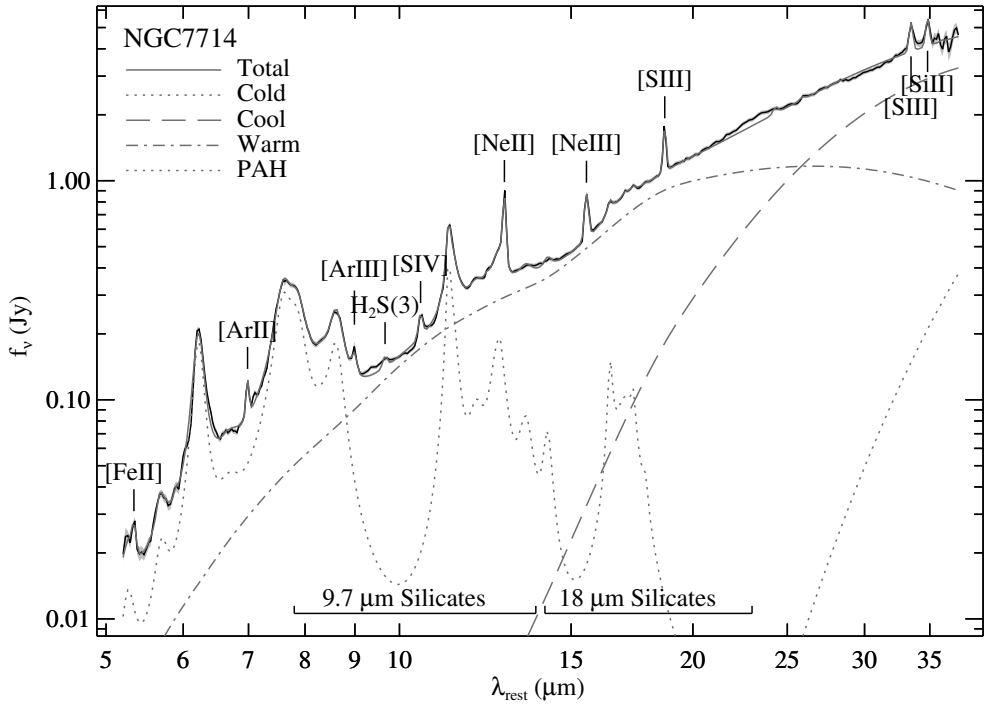

Figure 9.2 Closeup view of the IRS wavelength range for the decomposition of the starburst galaxy NGC 7714 presented in Figure 9.1. The various decomposition components are shown as indicated in the figure legend. Also shown is the 1–σ uncertainty in the IRS spectrum (*dark shaded regions*) and the formal 1–σ error contour for the total fit (*light shaded regions*). Emission lines and the wavelength ranges over which silicate emission and absorption is observed are also labeled.

to the *AGN* component is fixed to $\tilde{\tau}_V^{\rm AGN} = 25$. The *hot* and *warm* dust components each have three free parameters: $\tilde{\alpha}_i$, $\tilde{\tau}_{9.7}^i$, and $\tilde{U}_i$ determine the component luminosities, 9.7 μm optical depths, and dust temperatures via $\bar{T}_i \equiv T(\tilde{U}_i)$ (see eq. [5.4]). The *cool* and *cold* components each have two free parameters: $\tilde{\alpha}_i$ and $\tilde{U}_i$ (see eq. [5.6]). Finally, there are two additional free parameters that control the water-ice and HAC contributions to the total opacity: $\tilde{\eta}_{\rm ice}$ and $\tilde{\eta}_{\rm HAC}$ (see eqs. [4.14] and [4.15]).

We impose the following constraints to provide sensible limits over which

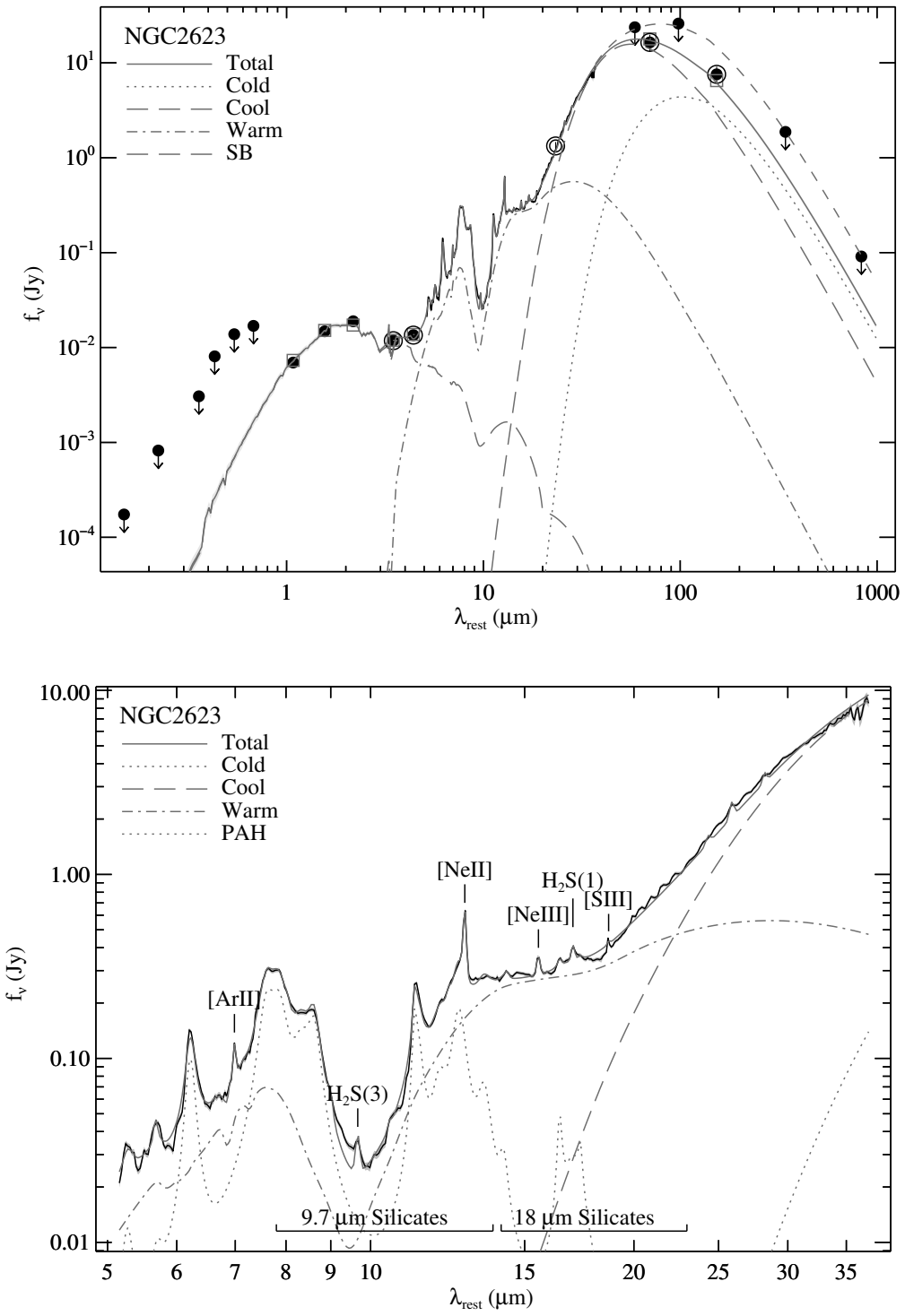

Figure 9.3 Ultraviolet to millimeter wavelength (*upper-panel*) and IRS (*lower-panel*) views of the NGC 2623 spectral decomposition. Labeling and annotations are as in Figs. 9.1 and 9.2.

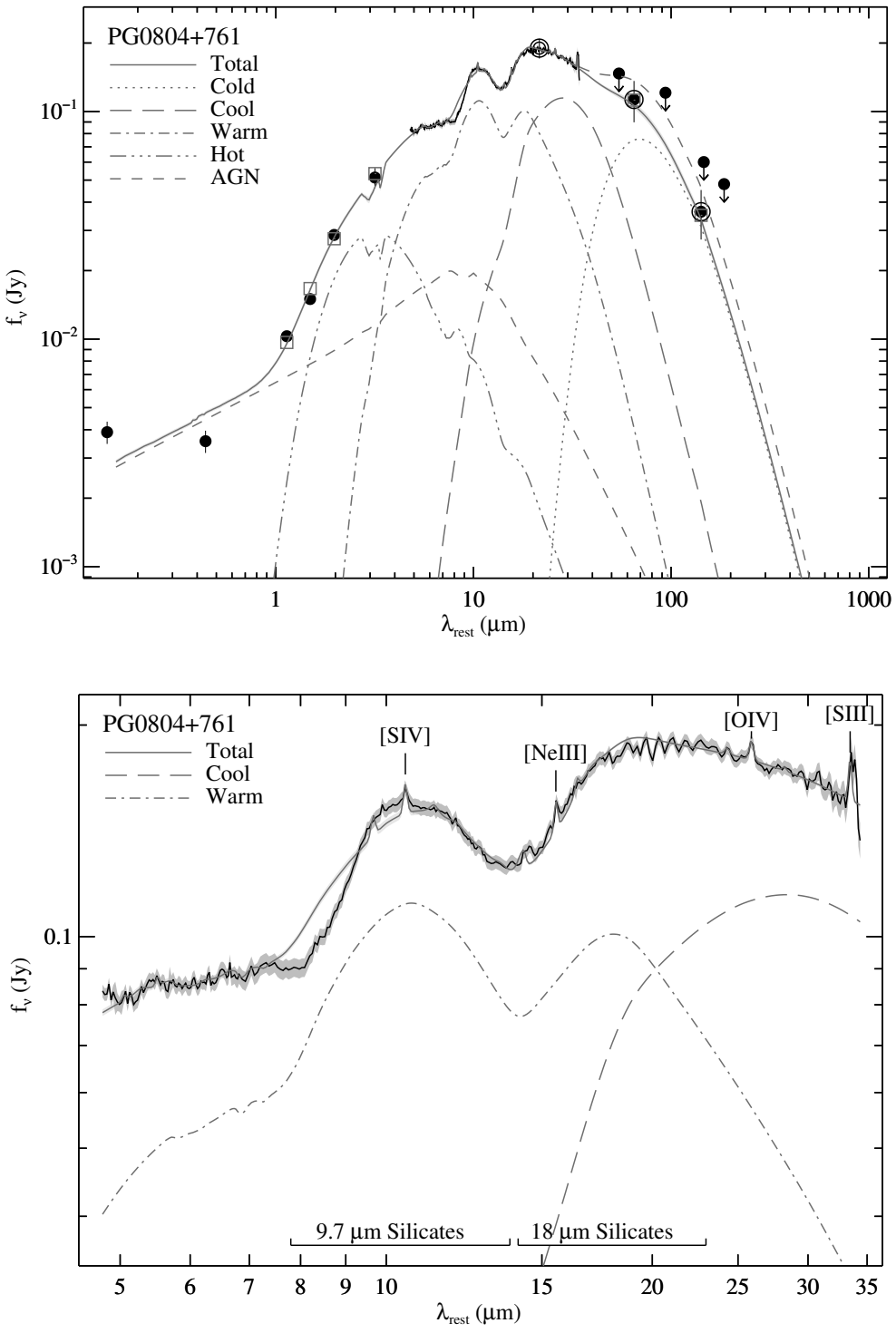

Figure 9.4 Ultraviolet to millimeter wavelength (*upper-panel*) and IRS (*lower-panel*) views of the PG 0804+761 spectral decomposition. Labeling and annotations are as in Figs. 9.1 and 9.2.

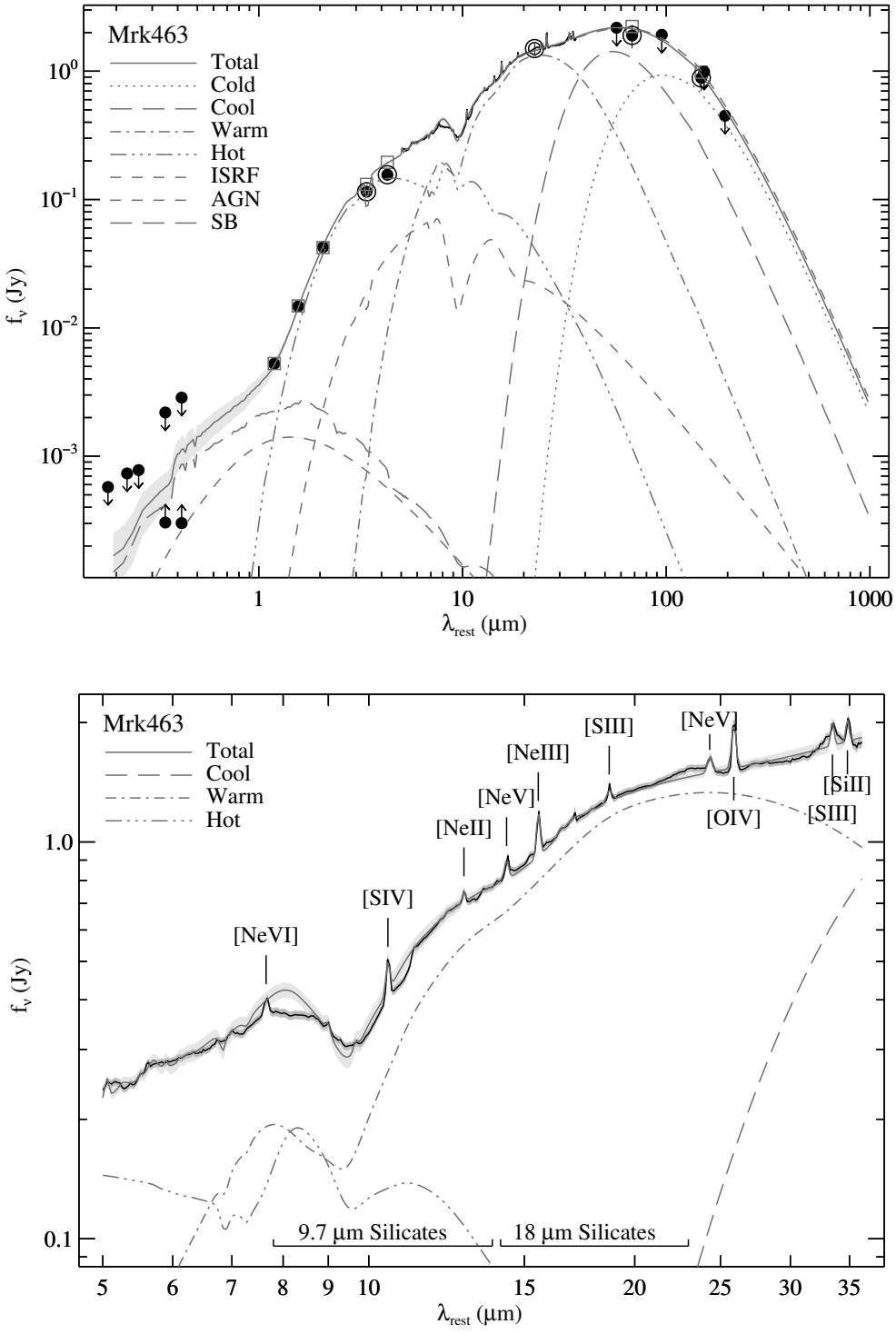

Figure 9.5 Ultraviolet to millimeter wavelength (*upper-panel*) and IRS (*lower-panel*) views of the Mrk 463 spectral decomposition. Labeling and annotations are as in Figs. 9.1 and 9.2.

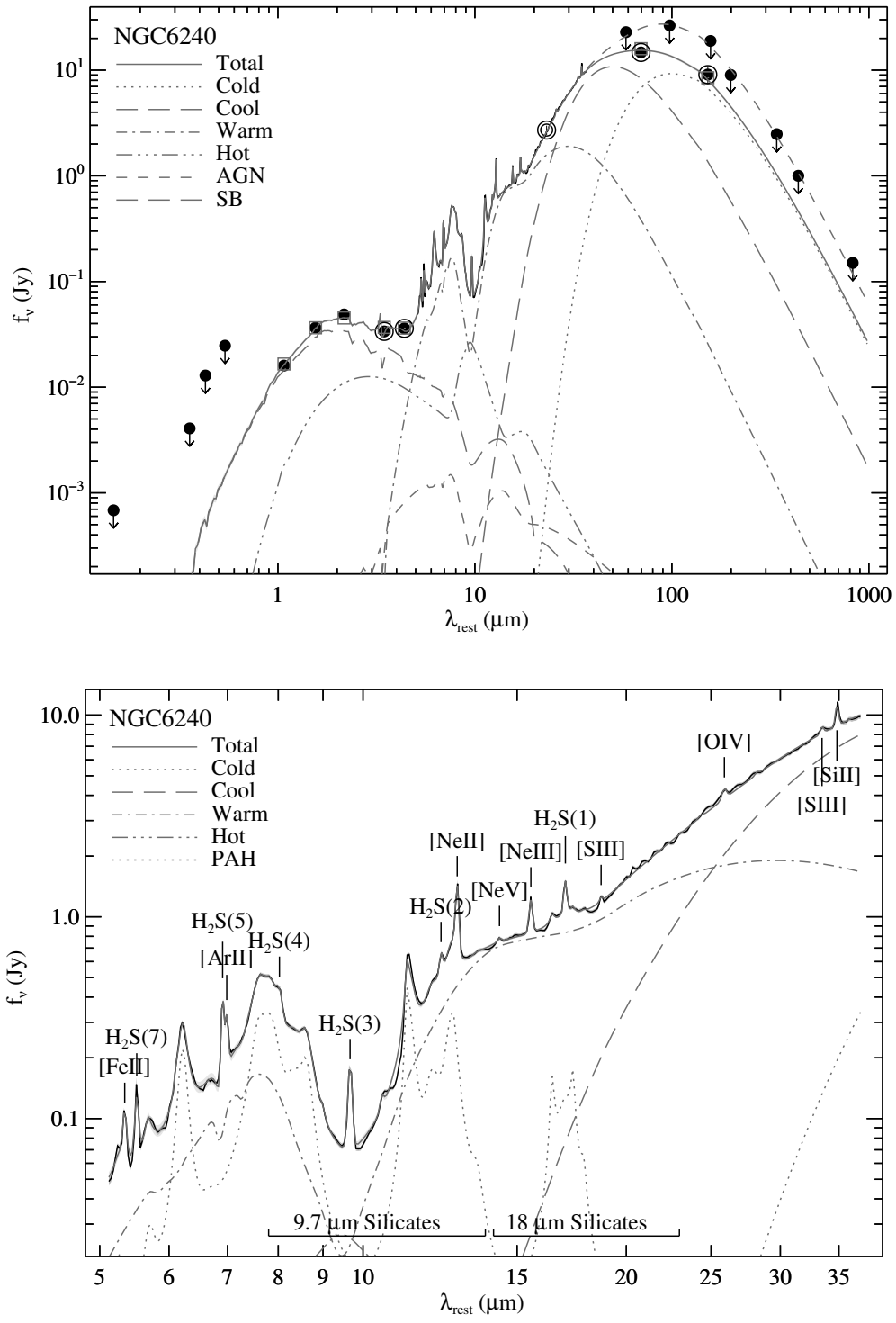

Figure 9.6 Ultraviolet to millimeter wavelength (*upper-panel*) and IRS (*lower-panel*) views of the NGC 6240 spectral decomposition. Labeling and annotations are as in Figs. 9.1 and 9.2.

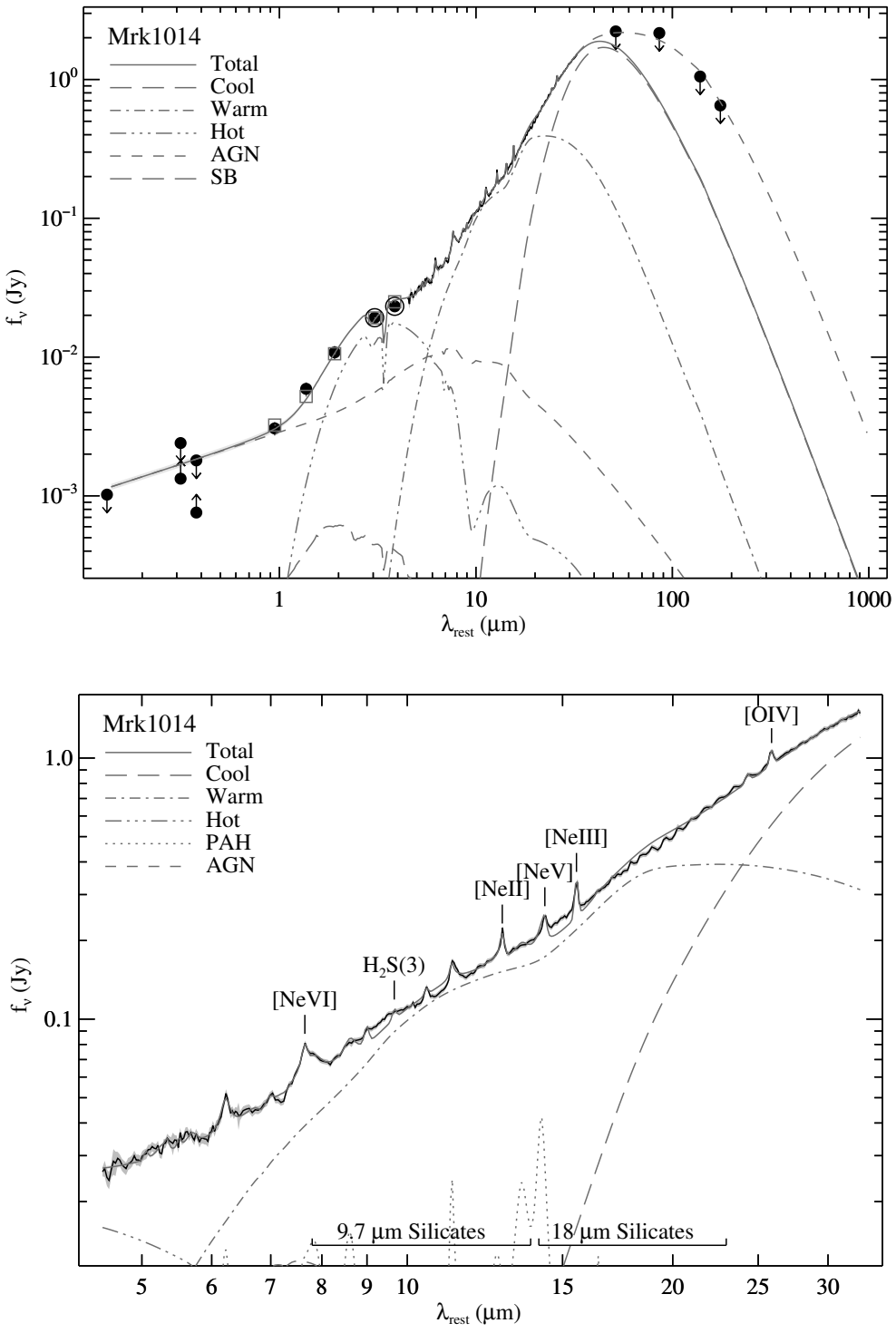

Figure 9.7 Ultraviolet to millimeter wavelength (*upper-panel*) and IRS (*lower-panel*) views of the Mrk 1014 spectral decomposition. Labeling and annotations are as in Figs. 9.1 and 9.2.

the free parameters may range: (1) The magnitude of the radiation field energy density illuminating each dust component is constrained to give characteristic dust temperatures satisfying $20\,\mathrm{K} < \bar{T}_{\mathrm{cold}} < 50\,\mathrm{K}$, $50\,\mathrm{K} < \bar{T}_{\mathrm{cool}} < 150\,\mathrm{K}$, $150\,\mathrm{K} < \bar{T}_{\mathrm{warm}} < 350\,\mathrm{K}$, and $350\,\mathrm{K} < \bar{T}_{\mathrm{hot}} < 1500\,\mathrm{K}$; (2) The maximum water-ice and HAC contributions to the total opacity are constrained by their strengths in sources with very clean absorption spectra (see §4.8); (3) The extinction to the *AGN* source component is fixed to $\tau_V = 25$; (4) The extinction to the *SB* source component must satisfy $\tau_V < 5$; (5) The optical depths through the screens obscuring the *hot* and *warm* components must not exceed the critical values beyond which their extinction-corrected luminosities would exceed the total dust luminosity; (6) The ratio of the unextinguished luminosity of the *SB* component to the luminosity of the *PAHs* component must be between the values obtained for our unobscured and obscured template starbursts NGC 7714 and NGC 2623; and (7) The *hot* dust covering fraction (i.e. the ratio of the unextinguished *hot* dust luminosity to the unextinguished *AGN* luminosity) must be > 0.5 consistent with observations, corresponding to torus opening angles $> 30°$.

9.3 Derived Quantities

9.3.1 Source and Dust Component Luminosities

Example apparent and extinction-corrected source and dust component luminosities from the nuclear decompositions of the galaxies in our template sample are presented in Table 9.2. The apparent luminosity of each component is calculated

Table 9.2. Nuclear SED Decomposition Luminosities

	Source						Dust						
Galaxy	$L_{\rm source}$ ($10^{10}\,L_\odot$)	$\tilde{\alpha}_{\rm ISRF}$	$\tilde{\alpha}_{\rm SB}$	$\tilde{\alpha}'_{\rm SB}$	$\tilde{\alpha}_{\rm AGN}$	$\tilde{\alpha}'_{\rm AGN}$	$L_{\rm dust}$ ($10^{10}\,L_\odot$)	$\tilde{\alpha}_{\rm cold}$	$\tilde{\alpha}_{\rm cool}$	$\tilde{\alpha}_{\rm warm}$	$\tilde{\alpha}'_{\rm warm}$	$\tilde{\alpha}_{\rm hot}$	$\tilde{\alpha}'_{\rm hot}$
NGC 7714	0.78	0	1	3.8	0	0	3.25	0.344	0.394	0.262	0.275	0	0
	±0.03	···	±0.05	±0.1	···	···	±0.04	±0.011	±0.006	±0.004	±0.004	···	···
NGC 2623	0.72	0	1	27	0	0	22.5	0.136	0.792	0.072	0.194	0	0
	±0.05	···	±0.09	±2	···	···	±0.2	±0.010	±0.010	±0.001	±0.004	···	···
PG 0804+761	99	0	0	0	1	1.27	62.5	0.036	0.146	0.457	0.639	0.361	1
	±2	···	···	···	±0.03	±0.04	±1.1	±0.002	±0.003	±0.011	±0.013	±0.014	±0.02
Mrk 463	8.2	0.12	0.23	1.03	0.65	18.1	74	0.068	0.165	0.470	0.703	0.297	1
	±0.6	±0.03	±0.05	±0.08	±0.05	±1.4	±2	±0.003	±0.005	±0.027	±0.038	±0.009	±0.03
NGC 6240	2.61	0	> 0.99	24.8	< 0.01	0.29	45.2	0.257	0.528	0.198	0.514	0.017	0.017
	±0.07	···	±0.04	±0.7	···	±0.01	±0.7	±0.011	±0.009	±0.007	±0.020	±0.001	±0.001
Mrk 1014	120	0	0.018	0.49	0.98	1.86	337	···	0.583	0.336	0.352	0.081	0.66
	±3	···	±0.001	±0.01	±0.03	±0.04	±2	···	±0.005	±0.003	±0.003	±0.002	±0.02

Note. — Apparent and extinction-corrected luminosities of each source and dust component in the nuclear decompositions are given as fractions of $L_{\rm source}$ and $L_{\rm dust}$ (see eqs. [9.1] and [9.2]). Formal statistical uncertainties for the fitted luminosities are given beneath their values. The nuclear dust luminosity of Mrk 1014 is uncertain by ∼20% (i.e. the difference between its nuclear and global values) and its *cold* component luminosity is undetermined since no MIPS data is available to constrain its far-IR SED.

Table 9.3. Nuclear SED Decomposition Dust Masses

Galaxy	$M_{\rm cold}$ ($10^6\,M_\odot$)	$M_{\rm cool}$ ($10^4\,M_\odot$)	$M_{\rm warm}$ ($10^2\,M_\odot$)	$M_{\rm hot}$ ($M_\odot$)
NGC 7714	4.26 ± 0.13	4.90 ± 0.04	5.55 ± 0.05	0
NGC 2623	19.8 ± 1.4	335 ± 2	9.3 ± 0.2	0
PG 0804+761	1.53 ± 0.07	0.91 ± 0.01	2.95 ± 0.04	1.75 ± 0.09
Mrk 463	23.7 ± 0.9	185 ± 3	101 ± 13	7.9 ± 0.2
NGC 6240	67.3 ± 2.6	201 ± 1	69 ± 6	0.049 ± 0.003
Mrk 1014	···	736 ± 5	333 ± 3	1.13 ± 0.03

Note. — Formal statistical uncertainties for the fitted masses of the dust components in the nuclear decompositions are given along with their values. The mass of *cold* dust in the nucleus of Mrk 1014 is undetermined since no MIPS data is available to constrain its far-IR SED.

from

$$L_i = 4\pi D_L^2 \int f_\nu^i \, d\nu \equiv \begin{cases} \tilde{\alpha}_i L_{\rm source} & L_i \in L_{\rm source}, \\ \tilde{\alpha}_i L_{\rm dust} & L_i \in L_{\rm dust}, \end{cases} \tag{9.1}$$

where D_L is the luminosity distance to the galaxy (see Table 8.1), and $L_{\rm source}$ and $L_{\rm dust}$ are the sums of the luminosities of all source and dust components, respectively. Extinction-corrected luminosities are calculated from

$$L_i' = 4\pi D_L^2 \int \frac{f_\nu^i}{\Upsilon_i(\nu)} \, d\nu \equiv \begin{cases} \tilde{\alpha}_i' L_{\rm source} & L_i \in L_{\rm source}, \\ \tilde{\alpha}_i' L_{\rm dust} & L_i \in L_{\rm dust}, \end{cases} \tag{9.2}$$

where the Υ_i are the extinction terms for each component (i.e. $\Upsilon_{\rm AGN} = [1-\tilde{\epsilon}_{\rm AGN}] + \tilde{\epsilon}_{\rm AGN} \exp[-\tau_{\rm AGN}]$ for the *AGN* component and $\Upsilon_i = \exp[-\tau_i]$ for the *warm*, *hot*, and *SB* components).

9.3.2 Dust Component Masses

The mass of dust in each of the *cold*, *cool*, *warm*, and *hot* nuclear decomposition components of the galaxies in our template sample are provided in Table 9.3. We generalize the expression used to calculate dust masses for a single grain-size and composition (e.g. see eq. [4] of Klaas et al. 2001) to the case in which grains are distributed both in size and composition. The mass of dust in each component is therefore given by

$$M_i = D_L^2 \frac{f_\nu^i(\lambda_0)}{E_\nu^i(\lambda_0) e^{-\tau_i(\lambda_0)}} \sum_j \int \frac{4}{3} \pi a^3 \rho_j \frac{1}{n_{\rm H}} \frac{dn_j}{da}\, da, \tag{9.3}$$

which is the product of the number of hydrogen nucleons required to power the fitted dust component and the total dust mass per hydrogen nucleon for the adopted dust model (summed over the graphite and silicate compositions). In this equation, λ_0 is an arbitrary wavelength at which the terms are evaluated, and the densities of graphite and silicate are taken to be $\rho_{\rm gra} = 2.24$ and $\rho_{\rm sil} = 3.50$ g^{-1} cm^{-3}. For comparison to the dust masses and luminosities obtained from the nuclear decompositions, we present the corresponding properties for the global decompositions of the galaxies in our template sample in Table 9.4.

9.3.3 Comparison With Previous Results

Klaas et al. (2001) fit the far-IR to sub-mm wavelength SEDs of a sample of ULIRGs using dust-modified blackbodies with temperatures typically ranging between 28 and 50 K. Included among their sources are two galaxies which are also in our sample, Mrk 463 and NGC 6240, for which they fit single $\beta = 2$ dust components with temperatures of 40 and 33 K, respectively. In a similar study of quasars presented in Haas et al. (2003), the far-IR SED of PG 0804+761 is fitted with a

Table 9.4. Global SED Decomposition Dust Properties

Galaxy	$L_{\rm dust}$ ($10^{10}\,L_\odot$)	$\tilde{\alpha}_{\rm cold}$	$\tilde{\alpha}_{\rm cool}$	$M_{\rm cold}$ ($10^6\,M_\odot$)	$M_{\rm cool}$ ($10^4\,M_\odot$)
NGC 7714	4.50 ± 0.05	0.530 ± 0.010	0.280 ± 0.006	9.1 ± 0.1	4.8 ± 0.1
NGC 2623	30.3 ± 0.9	0.365 ± 0.036	0.581 ± 0.019	72 ± 13	331 ± 3
PG 0804+761	62.6 ± 3.8	0.050 ± 0.004	0.140 ± 0.010	2.2 ± 0.1	0.88 ± 0.03
Mrk 463	74.5 ± 1.3	0.076 ± 0.014	0.153 ± 0.007	27 ± 5	173 ± 8
NGC 6240	61.2 ± 3.7	0.461 ± 0.039	0.381 ± 0.040	164 ± 21	197 ± 60
Mrk 1014	414 ± 23	0.188 ± 0.015	0.469 ± 0.054	303 ± 18	730 ± 280

Note. — Global SED decomposition properties derived from fitting the total far-IR emission (see Figs. 9.1–9.7). All quantities are analogous to those in Tables 9.2 and 9.3. The temperatures of the *cold* and *cool* components are the same as given in Table 9.1. Formal statistical uncertainties for the fitted properties are given along with their values.

47 K dust component. The temperatures we derive from our decompositions are all consistent with these values. Our decomposition of Mrk 463 includes contributions from 30 K and 55 K dust components, while our fit to NGC 6240 includes emission from dust at 29 K and 61 K. Finally, our decomposition of PG 0804+761 is dominated in the far-IR by emission from 42 K dust. For all three sources, the temperatures of the single component fits in the literature fall between the temperatures of the dust in our multi-component fits. Klaas et al. (2001) also fit the $\lambda > 60\,\mu$m SED of NGC 6240 with multiple $\beta = 2$ dust components and obtain temperatures of 31 and 41 K (they also include a 10 K component to fit to sub-mm upper-limits). Again, these temperatures are quite comparable to ours, noting that our warmer component is at a somewhat higher temperature in order to fit to the shorter wavelength data included in our fits.

As illustrated by these decompositions, multi-component fits including dust at different temperatures are rarely unique since several components can usually be added together to approximate the SED of emission from a smaller number

of components. In fact, dust in galaxies is likely to be distributed throughout many regions with various heating conditions, and is therefore distributed over a continuum of temperatures. Any multi-component decomposition therefore serves only to characterize these distributions of temperatures. Additionally, if either or both of the restrictions that dust is optically-thin to its own emission and that its far-IR emissivity index is characterized by $\beta = 2$ imposed above are lifted, yet different dust temperatures may be obtained for the same SEDs. For example, Klaas et al. (2001) perform fits in which the dust optical depth and emissivity are free parameters, and obtain much higher temperatures—52 and 57 K for Mrk 463 and NGC 6240, respectively. Given the multiple factors determining the temperatures derived from spectral decompositions (e.g. fixed versus variable β), we emphasize that caution must be taken when comparing temperatures derived from different methods to ensure that they are in fact comparable.

The total far-IR luminosity from dust inferred from a multi-component decomposition is largely independent of the number of components and the choice of their characteristic temperatures (since the luminosity is just the integral under the SED). The total mass of dust, however, depends upon these choices (since the mass is a strong function of temperature). Since the total mass of dust in galaxies is dominated by low-temperature material, decompositions with multiple components (including very cold dust) produce much higher dust masses. For example, Klaas et al. (2001) estimate the mass of dust in Mrk 463 to be greater than $5 \times 10^6\,M_\odot$ and less than $1.2 \times 10^7\,M_\odot$ as derived from their single and multi-component fits, respectively. Similarly, they estimate that the mass of dust in NGC 6240 is between $3.6 \times 10^7\,M_\odot$ and $5.8 \times 10^8\,M_\odot$. Our decompositions yield total globally integrated dust masses of $2.8 \times 10^7\,M_\odot$ and $1.6 \times 10^8\,M_\odot$ for the two sources, relatively consistent with the previously derived masses (within the un-

certainties of the methods). Klaas et al. (2001) estimate the H_2 mass of NGC 6240 to be $3.7 \times 10^{10}\,M_\odot$ (assuming $M[H_2] = 4.6 L_{CO}$). This value, along with our estimate of the total dust mass in NGC 6240, gives a gas-to-dust ratio of ∼230, in reasonable agreement with the canonical value of ∼165 from Li (2005).

9.3.4 Diagnostic Ratios

In Table 9.5, we present several "diagnostic" ratios for each galaxy in our template sample. The values are derived from the nuclear decomposition masses and luminosities presented in Tables 9.2 and 9.3. The first entry in this table gives the ratio of the total dust luminosity to the total gas mass. The total gas mass is calculated from the fitted value of the total dust mass and the gas-to-dust ratio of our adopted dust model: $M_{gas}/M_{dust} = 1.4\,M_H/M_{dust} = 124$ (Li & Draine 2001). The definition of this quantity is motivated by the fact that two sources with equivalent values of L_{dust} or L_{IR} may have completely different physical properties (e.g. a very massive but inactive system may have the same dust luminosity as a relatively small but highly active galaxy). The total dust luminosity is therefore a degenerate quantity which does not alone provide great insight into the nature of a galaxy. Normalizing the dust luminosity by the dust mass, however, does provide a means of breaking this degeneracy. This ratio characterizes the radiative efficiency of a galaxy, with smaller L_{dust}/M_{gas} ratios indicating lower-efficiencies and cooler dust temperatures and larger ratios indicating higher-efficiencies and warmer dust temperatures.

Also included in Table 9.5 are the ratios of the extinction-corrected *SB* and *AGN* source component luminosities to the total nuclear dust luminosity. A ratio of unity or greater in these quantities indicates that the total observed dust emis-

Table 9.5. Nuclear SED Decomposition Diagnostic Ratios

	Dust	Starburst		AGN		PAHs	
Galaxy	$L_{\rm dust}/M_{\rm gas}$[a] ($L_\odot\,M_\odot^{-1}$)	$L'_{\rm SB}/L_{\rm dust}$[b]	$L'_{\rm SB}/M_{\rm gas}$[b] ($L_\odot\,M_\odot^{-1}$)	$L'_{\rm AGN}/L_{\rm dust}$[c]	$L'_{\rm AGN}/M_{\rm gas}$[c] ($L_\odot\,M_\odot^{-1}$)	$L_{\rm PAHs}/L_{\rm dust}$[d]	$L_{\rm PAHs}/M_{\rm gas}$[d] ($L_\odot\,M_\odot^{-1}$)
NGC 7714	60.4 ± 2.0	0.912 ± 0.018	55.3 ± 1.9	···	···	0.052 ± 0.002	3.17 ± 0.13
NGC 2623	78.2 ± 4.7	0.877 ± 0.028	68.5 ± 4.6	···	···	0.021 ± 0.001	1.65 ± 0.11
PG 0804+761	3270 ± 160	···	···	2.00 ± 0.06	6530 ± 327	···	···
Mrk 463	233 ± 10	0.114 ± 0.003	26.5 ± 0.9	2.00 ± 0.06	466 ± 16	···	···
NGC 6240	52.4 ± 2.1	1.43 ± 0.02	75.1 ± 2.8	0.017 ± 0.001	0.88 ± 0.03	0.032 ± 0.002	1.65 ± 0.11
Mrk 1014	···	0.173 ± 0.001	···	0.661 ± 0.001	···	0.012 ± 0.001	···

[a]Ratio of the total integrated dust luminosity to the total gas mass.

[b]Ratios of the extinction-corrected *SB* source component luminosity to the total dust luminosity and total gas mass.

[c]Ratios of the extinction-corrected *AGN* source component luminosity to the total dust luminosity and total gas mass.

[d]Ratios of the total *PAHs* component luminosity (integrated over all features) to the total dust luminosity and total dust mass.

Note. — Formal statistical uncertainties for the diagnostic ratios are given along with their values. Mass-normalized values are not given for Mrk 1014 since no MIPS data is unavailable to constrain its far-IR SED (and therefore $M_{\rm gas}$). This absence of data also results in a ∼20% uncertainty for the value of $L_{\rm dust}$ for Mrk 1014 (i.e. the difference between its nuclear and global values), and therefore in all quantities normalized by this total dust luminosity.

sion could be heated by the fitted source component. A ratio significantly greater than unity indicates that either the source extinction correction was over-predicted, or that the dust covering fraction is less than unity. In the latter case, the fraction of the source which is covered by dust is obtained from the inverse of the source-to-dust ratio. A ratio significantly less than unity indicates that either the extinction to the source component is underpredicted, or that additional unmodeled source emission is present which has not been accounted for in the decomposition (e.g. the apparent near-IR luminosity of a deeply embedded source may be small in comparison to a relatively unextinguished source, even though the two may be intrinsically similar in strength). In addition to the source-to-dust *luminosity* ratios, we also calculate source-to-dust *mass* ratios, where the extinction-corrected SB and AGN luminosities are given as a fraction of the total gas mass. This quantity indicates the relative "dustiness" (in terms of mass) of a source compared to others of the same luminosity.

9.3.5 PAH Feature Luminosities

The total apparent PAH luminosity (integrated over all features) of each source in our template sample, normalized to both the total dust luminosity and the total gas mass, are presented in Table 9.5. Additionally, the fitted ratios of the luminosities of the four primary PAH complexes (see Table 6.1) to the total PAH luminosity are presented in Table 9.6. For reference, we also provide the corresponding ratios for the mean starburst galaxy spectrum from Brandl et al. (2006) used to create our PAH template, and the median ratios for the star-forming SINGS galaxies from Smith et al. (2007). With the exception of Mrk 1014, the fitted PAH luminosity ratios of the four sources in our sample with well-detected PAH emission are fairly

Table 9.6. PAH Feature Luminosities

Galaxy	$L_{6.2}/L_{\rm PAHs}$	$L_{7.7}/L_{\rm PAHs}$	$L_{11.3}/L_{\rm PAHs}$	$L_{17}/L_{\rm PAHs}$
NGC 7714	0.114 ± 0.002	0.396 ± 0.004	0.114 ± 0.002	0.067 ± 0.004
NGC 2623	0.088 ± 0.002	0.407 ± 0.005	0.074 ± 0.001	0.026 ± 0.002
PG 0804+761	...	...	...	...
Mrk 463	...	...	...	...
NGC 6240	0.115 ± 0.005	0.371 ± 0.009	0.105 ± 0.002	0.069 ± 0.004
Mrk 1014	0.112 ± 0.013	0.211 ± 0.014	0.067 ± 0.008	0.051 ± 0.016
Mean Starburst	0.10	0.39	0.11	0.08
Median SINGS	0.11	0.42	0.12	0.06

Note. — Ratios of the luminosities of each of the four main PAH complexes to the total PAH luminosity. Formal statistical uncertainties for the fitted properties are given along with their values. Also shown are the ratios for the mean starburst galaxy spectrum used to derive our PAH template (see Table 6.1) and the median values for the SINGS sample of star-forming galaxies presented in Smith et al. (2007).

consistent with the values of the mean starburst and SINGS templates (see §10 for more on the PAH emission from Mrk 1014).

The apparent ratios of PAH emission from a galaxy may differ from those of the low-obscuration templates in Table 9.6 for several reasons. First, the size of an individual PAH molecule (i.e. the number of carbon atoms it contains) and its ionization state can alter the relative strengths of its emission features (see Draine & Li 2001). Additionally, the apparent ratios may vary as a result of extinction from intervening dust. In Table 9.7, we present the ratios of the 6.2, 7.7, and 11.3 μm PAH complexes to the total PAH luminosity for the mean starburst galaxy from Table 9.6 after its emission passes through screens of dust with different values of $\tau_{9.7}$. In addition to the feature ratios, we also provide correction factors used to convert the total apparent PAH luminosity (i.e. integrated over all features) into the actual emitted PAH luminosity for a particular value of $\tau_{9.7}$ estimated from the feature ratios.

Table 9.7. Extinguished Mean Starburst PAH Feature Luminosities

$\tau_{9.7}$	$L_{6.2}/L_{\rm PAHs}$[a]	$L_{7.7}/L_{\rm PAHs}$[a]	$L_{11.3}/L_{\rm PAHs}$[a]	$L'_{\rm PAHs}/L_{\rm PAHs}$[b]
0.25	0.101	0.402	0.106	1.09
0.5	0.104	0.411	0.099	1.19
1	0.111	0.429	0.087	1.40
2	0.123	0.462	0.067	1.91

[a]Complex-to-total PAH luminosity ratio for the indicated screen $\tau_{9.7}$.

[b]Unextinguished-to-apparent PAH luminosity ratio for the indicated screen $\tau_{9.7}$.

Chapter 10

Dusty Galaxy Case Studies

10.1 NGC 7714

Our low-obscuration template starburst is a massive barred spiral galaxy that makes up the western component of the interacting system Arp 284. The compact ultraviolet-luminous starburst nucleus of NGC 7714 has very low extinction, and there is no evidence at any wavelength for the presence of an AGN. The IRS spectrum of this galaxy (see Brandl et al. 2004) exhibits a rising continuum, strong PAH feature and line emission, and no perceptible 9.7 μm silicate absorption. As suggested by the relatively flat continuum near 10 μm, all parameters from our fitting are consistent with this starburst galaxy being relatively unobscured at all wavelengths. The *warm* dust and *SB* source components have fitted values of $\tau_{9.7} \approx 0.19$ and $\tau_V = 0.97$, respectively. Puxley & Brand (1994) estimate a screen extinction to the ionized gas within NGC 7714 of $A_V \approx 0.86 \pm 0.13$ using optical and near-IR recombination lines, a value which is entirely consistent with our *SB* component optical depth. For our adopted dust model, $A_V \approx 0.86$ corresponds to $\tau_{9.7} \approx 0.07$–0.22, depending on the influence of scattering in the total effective opacity (the latter value is for zero scattering contribution, as expected for spherical symmetry). This range is again completely consistent with the extinction we find for the *warm* dust component.

The extinction-corrected *SB*-to-dust ratio given in Table 9.5 is $L'_{\rm SB}/L_{\rm dust} = 0.91$, indicating that the fitted source component is capable of powering nearly all (i.e. 91%) of the total dust emission. Although we attempt to calculate the true far-

IR dust luminosity of the nuclear point-source, we may nonetheless overestimate this quantity since our MIPS photometry may still contain flux from outside the nucleus. Such an overestimate could give rise to the slight source-luminosity deficit in our decomposition (i.e. there is not enough source emission to explain the observed dust emission). Given this plausible explanation, and the fact that the fitted deficit is small ($< 10\%$), we conclude that the observed source-to-dust ratio of NGC 7714 is consistent with the total dust emission from the system being powered by star-formation.

Our decomposition of this galaxy therefore indicates that the warmest dust in pure low-obscuration starbursts typically has a temperature $\sim$165 K, and that emission from $\sim$1000 K dust is therefore negligible. Also, the observed PAH luminosity in NGC 7714 is $\sim$5.2% of its total nuclear dust luminosity, providing an estimate of the typical total PAH strength in low-obscuration starbursts. Smith et al. (2007) find a median PAH-to-dust luminosity ratio of $\sim$10% for the "normal" (i.e. non-starburst) star-forming galaxies in the SINGS sample, with the ratio ranging between 3.2 and 16% for the sample. Thus, the ratio measured for NGC 7714 is consistent with this range, with the nearly factor of two difference from the median value likely indicating real differences in the emission from galaxies with different levels of star-formation. Note also that the PAH ratio $L_{11.3}/L_{7.7} \approx 0.28$ for NGC 7714 is very similar to the value of this ratio for the unobscured mean starburst template ($\sim$0.27). Consistent with the results from other extinction indicators, the PAH emission in NGC 7714 therefore appears to be relatively unobscured.

The total global dust emission in our sample (i.e. obtained using *IRAS* and *ISO* far-IR data) ranges from $\sim$1.0 to 1.4 times the nuclear emission (i.e. obtained

using MIPS data). Lançon et al. (2001) estimate that only 10–50% of the stellar emission in NGC 7714 emerges from the $2'' \times 2''$ ($\sim$0.37 pc^2) nucleus, and therefore suggest that 50–90% of the far-IR *IRAS* emission likely emerges from the extended disk of the galaxy. They further reason that the strength of the extra-nuclear far-IR emission is likely to be towards the lower end of this range, since the ultraviolet observations used to quantify the stellar emission strength are prone to missing emission from extinguished populations. In comparing the results of our global and nuclear spectral decompositions of NGC 7714, we calculate that at least $\sim$50% of the *cold* dust component luminosity (and 30% of the total dust emission) emerges from extended regions, consistent with the Lançon et al. (2001) prediction.

10.2 NGC 2623

Our extinguished template starburst galaxy is a late stage merger with long tidal tails and a $r^{1/4}$ nuclear stellar light profile (Wright et al. 1990; Scoville et al. 2000). The radio continuum (Condon et al. 1991) and mid-IR (Soifer et al. 2001) emission is similarly dominated by a compact nuclear source. The IRS spectrum of NGC 2623 is dominated by deep silicate absorption features at 9.7 and 18 μm and a very steep continuum beyond 20 μm. The fitted optical depths to the *warm* dust and *SB* source components of NGC 2623 are $\tau_{9.7} \approx 3.5$ and $\tau_V \approx 4.8$. Note that Brandl et al. (2006) find an apparent 9.7 μm optical depth of $\sim$1.5, which is more than a factor two lower than our fitted value. This difference occurs as a result of the method they employ to determine the *apparent* optical depth—namely, interpolating a smooth continuum above the silicate absorption feature, and using the ratio of this "unextinguished" continuum to the observed value to infer $\tau_{9.7}$. In contrast, the unextinguished continuum in the dust model used in

our decomposition method is not smooth at 9.7 μm, but instead contains a silicate *emission* feature (the presence of which is consistent with observations—e.g. see the fit for PG 0804+761)—therefore requiring a higher optical depth to obtain the same extinguished continuum.

We find no evidence for the presence of an AGN contribution to the SED of NGC 2623, consistent with the similar conclusion in Risaliti et al. (2000) based upon hard X-ray observations. The extinction-corrected *SB*-to-dust ratio given in Table 9.5 is $L'_{\rm SB}/L_{\rm dust} = 0.88$, indicating that the fitted source component is capable of powering most of the total dust emission. As with NGC 7714, it is likely that this ratio is indicative of an entirely star-formation powered system (taking into account the likely small overprediction of the nuclear dust luminosity due to the MIPS resolution). Like NGC 7714, the mid-IR spectrum of NGC 2623 also exhibits significant emission from PAHs, albeit a factor ∼2.5 weaker. The PAH ratio $L_{11.3}/L_{7.7} \approx 0.18$ for NGC 2623 is also lower than the value for NGC 7714, with the lower ratio being consistent with PAH emission obscured by a screen of dust with $\tau_{9.7} \approx 1$ (as determined by comparison with the obscured mean starburst template properties in Table 9.7). For this optical depth, the apparent PAH luminosity of the mean starburst template is only ∼71% its true emitted value. Using this correction factor, we estimate that the true PAH-to-dust luminosity ratio of NGC 2623 is $L'_{\rm PAHs}/L_{\rm dust} \approx 0.029$, a factor ∼1.8 lower than NGC 7714. See §11.1 for a detailed comparison of the properties of the low obscuration system NGC 7714 and the obscured starburst NGC 2623.

10.3 PG 0804+761

Our Type-1 template AGN is a variable source displaying ∼40% near-IR and 10.6 μm brightness fluctuations over the course of a decade (Neugebauer & Matthews 1999). The first deep infrared observations of this source were obtained with *ISO* (Haas et al. 2003), which revealed a power-law spectral shape and a very warm infrared SED peaking at ∼30 μm. Analysis of its IRS spectrum by Hao et al. (2005a) revealed the presence of strong 9.7 and 18 μm amorphous silicate emission features. In our decomposition, these emission features are produced by grains in the *warm* dust component. If we assume that the *warm* component is directly illuminated by the PG 0804+761 accretion disk ($L_{\rm AGN} = 1.26 \times 10^{12}\,L_{\odot}$), then equation (4.3) with $\tilde{U}c\hat{u}_{\nu} \rightarrow L_{\nu}/4\pi r^2$ indicates that this dust is located ∼19 pc from the nucleus. Jaffe et al. (2004) analyze 10 μm VLTI interferometric observations of the nucleus of the nearby Type-2 AGN NGC 1068, and conclude that its torus emission must be confined to a region $\lesssim$ 2 pc in size. Thus, some of the optically-thin *warm* component emission from PG 0804+761 may emerge from regions beyond the torus, perhaps from clouds in the narrow-line-region. Note that this distance to the *warm* dust is actually an upper-limit to the true distance, since the emission may also originate from indirectly illuminated torus clouds (see Fig. 5.1) at radii < 19 pc.

The unextinguished *AGN*-to-dust ratio in the PG 0804+761 decomposition is ∼2 (see Table 9.5), indicating that the *AGN* source component is more than capable of heating the total observed dust emission. The inverse of this ratio provides an estimate of the total dust covering factor (i.e. the fraction of sky covered by the torus as seen from the nucleus), which is $f_{\rm torus} \approx 0.5$ (note that this value is at the constraint imposed during the fit—see §9.2). This covering factor is consistent

with a torus opening angle of $\sim 30^\circ$ (i.e. $\sin\theta_{\rm torus} = f_{\rm torus}$, where $\theta_{\rm torus}$ is the angle extending from the mid-plane to the top of the torus as viewed from the accretion disk). Based upon the statistics of Seyfert galaxies (i.e. the relative numbers of Type-1 and 2 galaxies), Schmitt et al. (2001) find approximately twice as many Type-2 AGNs, and hence estimate $\theta_{\rm torus} = 45^\circ$. More recently, Hao et al. (2005b) study the AGNs in the Sloan Digital Sky Survey and conclude that $\theta_{\rm torus} \approx 30^\circ$, consistent with the value obtained from our decomposition.

Jaffe et al. (2004) find that the 8–13 μm VLTI spectrum of NGC 1068 can be decomposed into a $\bar{T} > 800\,{\rm K}$ dust component obscured by a $\tau_{9.7} = 2.1 \pm 0.5$ screen and a $\bar{T} = 320 \pm 30\,{\rm K}$ component behind a $\tau_{9.7} = 0.3 \pm 0.2$ screen. The temperatures and screen optical depths of these components are comparable to those obtained in our spectral decomposition (see also the properties of Mrk 463). PG 0804+761 has the worst reduced χ^2 of the galaxies in our sample, due primarily to the poor fit to its IRS spectrum between 7.5–10 μm (although the fit to the rest of the SED is quite good). Jaffe et al. (2004) report a similar problem in this wavelength range in their fit to the spectrum of NGC 1068, and conclude that the fit is improved using high-temperature calcium aluminium silicate dust instead of the standard olivine-type silicates (the opacity of the 9.7 μm feature of the former species begins near 9 μm as opposed to the $\sim$8 μm onset for olivine). We finally note that our decomposition of the ultraviolet and optical emission is consistent with a largely uncovered *AGN* accretion disk—with only $\sim$25% covered—consistent with a Type-1 source.

10.4 Mrk 463

Our Type-2 template AGN is a merging system with two nuclei separated by $\sim 4''$ (Mazzarella et al. 1991). The portion of the IRS spectrum obtained with the short-low module is likely dominated by the eastern component Mrk 463e (since the slit of this module is only $\sim 3.6''$ wide and the observation targeted the eastern component), while the portion obtained with the wider-slit of the long-low module likely contains emission from both nuclei (although the optically-bright western component may not contribute significantly at these wavelengths). Mrk 463 has a luminous steep-spectrum radio core, and broad lines are seen in scattered optical (Miller & Goodrich 1990) and direct near-IR light (Goodrich et al. 1994; Veilleux et al. 1997). Like the quasar PG 0804+761, the mid-IR spectrum of this galaxy shows no discernible PAH emission features (Armus et al. 2004). Silicate absorption at $9.7\,\mu$m is clearly seen in the spectrum of Mrk 463, producing a mid-IR continuum dominated by a broad emission-like feature at $\sim 8\,\mu$m, characteristic of self-absorbed silicate dust. In our decomposition, this feature is primarily produced by the *warm* component which has a screen optical depth $\tau_{9.7} \approx 1.3$. Like the quasar PG 0804+761, Mrk 463 has a moderately obscured ($\tau_{9.7} \approx 2.1$) *hot* dust component. The *hot* component optical depth and the deviations of the fit to the IRS spectrum from 7.5–9 μm are both similar to the reported properties of PG 0804+761 and NGC 1068 described above. Unlike the fit to the quasar PG 0804+761, the *AGN* component of Mrk 463 is completely covered by obscuring clouds—i.e. $\tilde{\epsilon}_{\rm AGN} = 1$—as is expected for a Type-2 source.

The *AGN*-to-dust ratio for Mrk 463 is 1.93 (similar to the value for PG 0804+761), consistent with the *AGN* source component powering the total observed dust emission, and implying a torus opening angle $\theta_{\rm torus} \approx 31^\circ$. There

is evidence for *ISRF* and *SB* contributions in the decomposition, although these are bolometrically weak compared to the power of the AGN ($< 5\%$). Although Mrk 463 and PG 0804+761 have similar *AGN*-to-dust ratios, they have very different quantities of cooler dust. Mrk 463 has 16 times more *cold* dust by mass (see Table 9.3), and it also has a factor 14 times smaller dust luminosity-to-mass ratio (also indicative of cooler mean dust temperatures—see Table 9.5). Similarly, the ratio of the unextinguished *AGN* component luminosity to the total gas mass is a factor 14 smaller for Mrk 463 (i.e. it has 14 times more gas mass for the same accretion disk luminosity). In the standard AGN unification scenario, the only difference between a Type-1 source (such as PG 0804+761) and a Type-2 source (such as Mrk 463) is the orientation of the obscuring torus with respect to the observer. Thus, within this picture, Type-1 and Type-2 AGNs should have similar *cold* dust masses relative to their total masses, and they should therefore have similar *AGN* luminosity to mass ratios (since the accretion disk luminosity and the total mass of dust do not depend on orientation). In §11.3, we suggest that differences in the relative orientation of the accretion and host galaxy disks may explain why this simple consequence of the unification scenario does not hold for some galaxies. *We therefore emphasize that the SEDs of individual AGNs may appear falsely inconsistent with the unification scenario due to local geometrical factors, even if unification holds for AGNs as a class.*

10.5 NGC 6240

The first of our two composite sources is an interacting system containing two nuclei separated by $\sim 1''$ (so that both nuclei are contained within all IRS slits). With an $L_{\rm IR} \approx 6.5 \times 10^{11}\,L_{\odot}$, NGC 6240 is technically a LIRG, although it is often

treated as a ULIRG since it shares most properties with other members of the class. Based upon its optical nuclear spectrum, NGC 6240 is classified as a LINER (Armus et al. 1989), and X-ray observations (Komossa et al. 2003) provide clear evidence for the presence of a pair of AGNs located behind significant columns of absorbing neutral gas ($N_{\rm H} = 1$–$2 \times 10^{24}{\rm cm}^{-2}$). The mid-IR spectrum of NGC 6240 is extremely rich, displaying strong PAH features, both low and high ionization lines (e.g. [Ne II] 12.8 μm and [Ne V] 14.3 μm) as well as strong emission from molecular hydrogen (see Armus et al. 2006). Like NGC 2623, the mid-IR continuum of this galaxy is shaped by strong absorption from silicate grains at 9.7 and 18 μm, as indicated by the *warm* component screen optical depth of $\tau_{9.7} \approx 3.6$. The near-IR continuum of NGC 6240 is well-fitted by a combination of apparently unobscured weak *hot* dust and extinguished ($\tau_V = 4.7$) *SB* component emission. The detection of [Ne V] 14.3 μm in the high-resolution IRS spectrum of NGC 6240 presented in Armus et al. (2006) and the evidence for X-rays are both consistent with the presence of *hot* dust in our decomposition—indicating that a (potentially small) fraction of the near-IR emission is powered by an AGN.

Based upon *Chandra* X-ray observations, Lira et al. (2002) conclude that the AGN in NGC 6240 likely contributes between 30–50% of the bolometric luminosity. However, as reported in Armus et al. (2006), the small [Ne V]/[Ne II] and [Ne V]/$L_{\rm IR}$ flux ratios are both consistent with an AGN contribution of only 3–5% of the bolometric luminosity. Similarly, the apparent *hot* dust emission in our decomposition makes up just $\sim$2% of the total dust luminosity (compared to > 36 and 30% for PG 0804+761 and Mrk 463, respectively), so that any contribution to the observed near- and mid-IR from an AGN is very small. On the other hand, the *SB*-to-dust ratio for NGC 6240 is 1.43, indicating that the total observed dust emission could be powered by the observed *SB* component. This galaxy there-

fore presents quite a puzzle, whereby its appearance changes radically depending upon where you look—although X-rays suggest powerful AGNs, data at optical and longer wavelengths do not require such a presence. We note that even though the *hot* component in the decomposition is unobscured, it could still be associated with a deeply obscured AGN in a clumpy geometry, where most of the hottest dust is too obscured to be seen, and we view only the most unobscured portions (see §11.2). If this scenario is true, the actual *hot* dust contribution to the total bolometric luminosity could easily be pushed higher (see §11.2).

10.6 Mrk 1014

Our second composite source is a radio-quiet infrared-luminous QSO with broad optical emission lines (FWHM Hβ > 4000 km s^{-1}). Mrk 1014 displays twin tidal tails, indicative of a recent interaction and merger (MacKenty & Stockton 1984). It is a relatively warm far-IR source, with the peak of its SED located around 70 μm. Its mid-IR spectrum is characterized by a nearly power-law continuum, with no obvious silicate emission or absorption features, and weak PAH emission (see Armus et al. 2004). This power-law continuum is rather remarkable (assuming the continuum is thermal in origin) since a nearly featureless SED must be constructed from emission components which are known to have significant features (i.e. silicates). The decomposition which provides a solution to this puzzle is consistent with Mrk 1014 being a composite source, containing a combination of dust components seen in both our template starbursts and AGNs. Like the AGNs, Mrk 1014 contains a moderately obscured ($\tau_{9.7} \approx 2.7$) *hot* dust component and a much less obscured *warm* component ($\tau_{9.7} \approx 0.14$). Like the starbursts (and unlike the quasar PG 0804+761), Mrk 1014 also contains bolometrically significant

emission from cooler dust, comprising ∼60% of its total dust luminosity. We argue in §11.3 that some of this far-IR emission is likely powered by the AGN.

The values of the extinction-corrected *AGN*-to-dust and *SB*-to-dust luminosity ratios for Mrk 1014 are 0.66 and 0.17, respectively, indicating that the AGN is capable of powering $> 65\%$ of the observed dust emission from the galaxy. As fitted, the *AGN* and *SB* components are together capable of powering 83% of the observed dust emission, thereby requiring the presence of at least an additional 17% source luminosity to power the remaining dust emission (note also that the total nuclear dust luminosity from Mrk 1014 is uncertain by ∼20% since no MIPS data is available to constrain its far-IR SED). If all of this undetected source luminosity emerges from the AGN accretion disk (e.g. if we underpredict the *AGN* component luminosity as a result of too rigid a constraint on the *hot*-to-*AGN* luminosity ratio), the AGN would account for 83% of the bolometric luminosity of Mrk 1014. If, on the other hand, the remaining undetected source luminosity is entirely produced by a starburst (e.g. if we underpredict the *SB* component luminosity as a result of missing emission from highly embedded regions), then the AGN would account for 66% of the bolometric luminosity.

Armus et al. (2007) create diagnostic diagrams based upon mid-IR spectral lines (see their Figs. 5–8) which are all consistent with an AGN fraction between 50–90% for Mrk 1014. Additionally, Boller et al. (2002) conclude that Mrk 1014 is dominated by an AGN and not star-formation based upon X-ray observations. If we take the *PAHs*-to-dust luminosity fractions of the galaxies NGC 2623 and NGC 6240 to be representative of the range of values in obscured starbursts, then the *PAHs*-to-dust ratio of Mrk 1014 suggests that between ∼38 and 57% of its bolometric luminosity is powered by obscured star-formation (assuming all PAH

emission comes from star-formation). Given our conclusion above that the starburst contribution is between 17 and 34%, it is therefore likely either that we are underestimating the total starburst contribution based upon the source components (which seems improbable given the corroborating X-ray and emission line evidence), or that some of the observed PAH emission may actually be powered by the AGN (see §11.3). We note as well that the PAH feature luminosity ratios for Mrk 1014 (see Table 9.6)—in particular the 7.7 μm complex—differ significantly from the template starbursts, perhaps indicative of an AGN contribution giving rise to non-standard PAH emission.

Chapter 11

Properties of Starbursts and AGNs

11.1 Comparison of Starburst SEDs

From our modest sample of two starburst galaxy decompositions, it is apparent that starburst SEDs do not form a homogeneous group. Comparing the fits of NGC 2623 and NGC 7714, noticeable differences include a 30% higher maximum dust temperature, a factor 20 times higher maximum optical depth, a factor 2.5 times weaker *PAHs*-to-dust luminosity ratio, and comparatively weaker [Ne III] 15.56 μm, [S III] 18.71 μm, [S III] 33.48 μm, and [Si II] 34.82 μm line emission. If the nuclear emission from each starburst emerges from distinct star-forming clouds consisting of embedded stars surrounded by cocoons of dust (see Fig. 2.1), then many of the observed variations in the SEDs of NGC 7714 and NGC 2623 can be understood as resulting from: (1) differences in the total number of star-forming clouds (i.e. if individual cloud complexes in each galaxy have similar intrinsic luminosities, then the total luminosity of each galaxy is determined by the total number of clouds it contains), and (2) the mean optical depth through an individual cloud. There are, of course, many other factors shaping the SEDs of starbursts as well—e.g. age and metallicity. The simple model described in this section is therefore not intended to provide a comprehensive explanation of all starburst properties, but rather a structure within which to understand several general properties.

If we assume for simplicity that each cloud in a starburst has constant gas density, then the optical depth through a cloud is $\tau(r) = \tau_{\rm cloud}(r/r_{\rm cloud})$, where $\tau_{\rm cloud}$ and $r_{\rm cloud}$ are the total optical depth and radius of the cloud. As described

in §5.1, direct emission from stars heats a shell of dust out to a radius $r_{\rm shell}$, corresponding to the optical depth $\tau_{9.7}^{\rm shell}$, where the cloud becomes optically thick to the heating stellar photons (i.e. essentially the outer edge of the photodissociation region). Using the equation for the optical depth above, we obtain $r_{\rm shell}^{2623}/r_{\rm shell}^{7714} = (\tau_{\rm cloud}^{7714}/\tau_{\rm cloud}^{2623})(r_{\rm cloud}^{2623}/r_{\rm cloud}^{7714})$. Here, we assume that $\tau_{9.7}^{\rm shell}$ is the same for all clouds since it depends only on the properties of dust and the illuminating radiation field. With $\tau_{\rm cloud} \rightarrow \tau_{\rm warm}$ (i.e. using the *warm* component optical depth as a proxy for the total cloud optical depth), this gives $r_{\rm shell}^{2623}/r_{\rm shell}^{7714} \approx (0.05)(r_{\rm cloud}^{2623}/r_{\rm cloud}^{7714})$. If the clouds in each galaxy are similar in size, this suggests that $r_{\rm shell}^{2623}/r_{\rm shell}^{7714} < 1$ (i.e. the *warm* dust shell from Fig. 5.1 is geometrically more extended in NGC 7714 than NGC 2623), so that stellar photons penetrate to much larger radii in the star-forming clouds of NGC 7714. Furthermore, the fractional cloud volume containing dust at the temperature of the *warm* component should be smaller in NGC 2623 than NGC 7714, and consequently the mass of *warm* dust relative to the total mass should be smaller as well. Indeed, from Table 9.3 we find that $(M_{\rm warm}/M_{\rm dust})_{7714} \approx 1.3 \times 10^{-4}$ and $(M_{\rm warm}/M_{\rm dust})_{2623} \approx 4 \times 10^{-5}$, consistent with this prediction.

For $r < r_{\rm shell}$, energy conservation dictates that the temperatures of grains within a cloud scale roughly as $T \propto r^{-1/2}$. This, coupled with the fact that $r_{\rm shell}^{2623} < r_{\rm shell}^{7714}$, implies that the mean temperature of such grains should be higher in NGC 2623 than NGC 7714—a prediction which is consistent with its 25% higher *warm* component temperature. The luminosities per unit mass of dust at the temperatures of the *warm* components in the two galaxies scale approximately as $(\bar{T}_{\rm warm}^{2623}/\bar{T}_{\rm warm}^{7714})^4 \approx (1.25)^4 \approx 2.4$ (i.e. a mass of *warm* dust from NGC 2623 will be ∼2.4 times more luminous than an equivalent mass from NGC 7714). This ratio, along with the absolute *warm* component dust masses for the two galaxies, suggests that the ratio of the *warm* component luminosities should be

$L^{2623}_{\rm warm}/L^{7714}_{\rm warm} \approx (\bar{T}^{2623}_{\rm warm}/\bar{T}^{7714}_{\rm warm})^4 (M^{2623}_{\rm warm}/M^{7714}_{\rm warm}) \approx 4$. The actual fitted ratio is 4.7, in reasonable agreement with this prediction. Furthermore, the $L_{\rm dust}/M_{\rm H}$ ratio from Table 9.5 is ∼30% higher in NGC 2623 than NGC 7714. If the *warm* dust in NGC 7714 were at the temperature of the *warm* dust in NGC 2623, the total dust luminosity of NGC 7714 would increase by ∼40%, and the resulting dust luminosity-to-mass ratios of the two sources would differ by only ∼7%. Thus, the different values of $L_{\rm dust}/M_{\rm gas}$ are directly related to the higher *warm* dust temperature in NGC 2623, which itself is likely directly related to the higher optical depth through the star-forming clouds in that galaxy.

The apparent *PAHs*-to-dust luminosity ratio is a factor ∼2.5 times lower in NGC 2623 than NGC 7714. We estimate that extinction to the *PAHs* component in NGC 2623 reduces its luminosity by a factor 1.4 (see §10), so that the unextinguished *PAHs*-to-dust luminosity ratios for the two galaxies differ by a factor 1.8. With this correction, we also find that $L_{\rm PAHs}/M_{\rm gas}$ is only a factor 1.4 greater in NGC 7714, as opposed to the observed factor 1.9. As described above, the *warm*-to-total dust mass ratio is less in NGC 2623, so that the volume within which PAH molecules are heated is smaller for this source. Therefore, some portion of the reduced *PAHs* luminosity giving rise to the differences in ratios described above likely results from such a difference in heating geometries. Using the ratio of the extinction-corrected $L_{\rm PAHs}/M_{\rm gas}$ values derived above, we estimate that this geometrical effect must decrease the observed *PAHs* luminosity of NGC 2623 by a factor 1.4 (i.e. assuming that the full difference is caused by this geometrical effect). Note that this factor is similar to the value $[(M_{\rm warm}/M_{\rm dust})_{2623}/(M_{\rm warm}/M_{\rm dust})_{7714}](L^{2623}_{\rm warm}/L^{7714}_{\rm warm}) \approx 1.4$, where the first term accounts for the difference in volume within which PAHs are heated, and the second term accounts for the difference in heating intensity. With these two correction

factors of 1.4, the *PAHs*-to-dust luminosity ratio of NGC 2623 differs by only ∼30% from that of NGC 7714. Recalling that the the dust luminosity of NGC 7714 would increase by ∼40% if its *warm* dust were at the same temperature of the dust in NGC 2623, the *PAHs*-to-dust luminosity ratios of the two galaxies differ by less than 10%.

The differences in the apparent PAH emission from our two starburst templates may therefore be understood as resulting from a combination of: (1) extinction to the PAHs, (2) the geometry of the PAH emitting regions, and (3) the method of normalizing the *PAHs* component luminosity. We suggest that the ratio $L_{\rm PAHs}/M_{\rm gas}$ is a somewhat better tracer of the true strength of PAH emission than $L_{\rm PAHs}/L_{\rm dust}$, since it is less affected by temperature effects. This latter ratio, or a related quantity such as $L_{6.2}/L_{\rm FIR}$, is often used to quantify the amount of star-formation in galaxies (e.g. Peeters et al. 2004). Given that both our template starbursts are believed to be entirely powered by star-formation, it is clear that there is significant variation in the relative strength of PAH emission in pure starbursts. *We therefore caution that great care must be taken when using any of these metrics to derive absolute quantities of star-formation, since both extinction and geometrical effects may result in different ratios for pure starburst galaxies.*

There is additional evidence for this scenario based upon our decompositions of the full dusty galaxy sample. Figure 11.1 shows the ratio of the total PAH luminosity (integrated over all features) to the total dust luminosity of all sources in our sample with available 70 or 160 μm MIPS data, plotted against the 9.7 μm optical depth of the *warm* dust component. The starburst galaxies are predominantly located in a band across the figure, with their relative PAH strength decreasing weakly with increasing optical depth. This overall trend is the same as observed

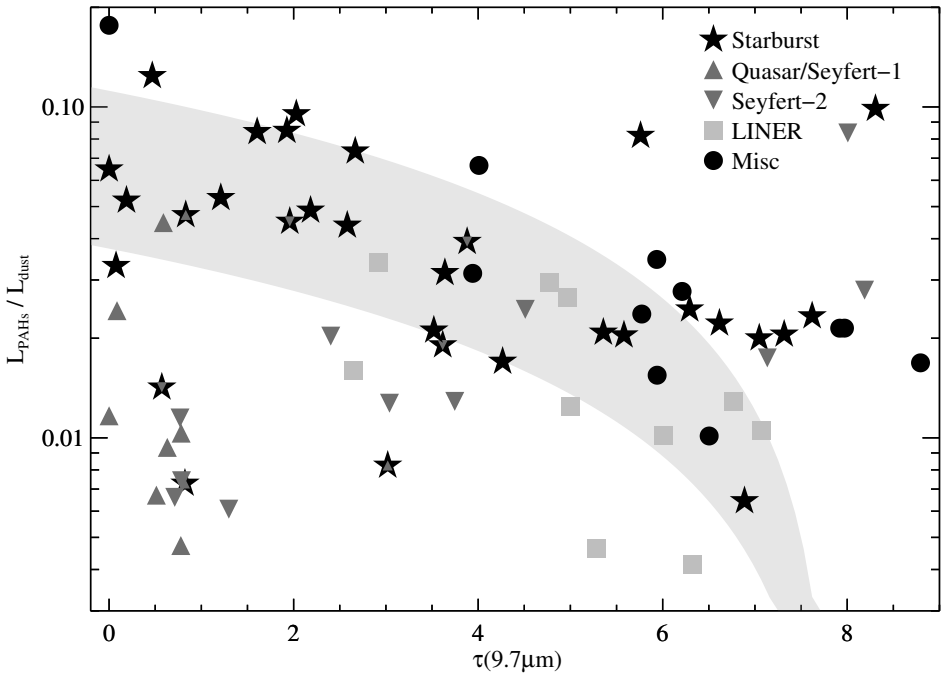

Figure 11.1 The ratio of the total PAH luminosity (integrated over all features) to the total dust luminosity is plotted against the 9.7 μm optical depth of the *warm* dust component. Different symbols represent galaxies with the optical classification indicated in the figure legend. The shaded region shows the trend expected if the relative PAH strengths and optical depths of the template starbursts NGC 7714 and NGC 2623 are linearly extrapolated over the entire sample.

between our two template starbursts, NGC 7714 and NGC 2623, as described in the previous paragraphs. The shaded band in Figure 11.1 illustrates the trend expected if the relative PAH strengths and optical depths of these two template starbursts are linearly extrapolated over the entire sample. While there is no reason that the relationship must be linear, this simple scenario produces a trend within which to understand the overall distribution of starburst galaxies in this plot. Note that as expected (due to their AGN), the Seyfert galaxies are predominantly located at relatively low PAH strengths (i.e. $L_{\rm PAHs}/L_{\rm dust} \lesssim 0.02$), although they do range over nearly an order of magnitude (see §11.3).

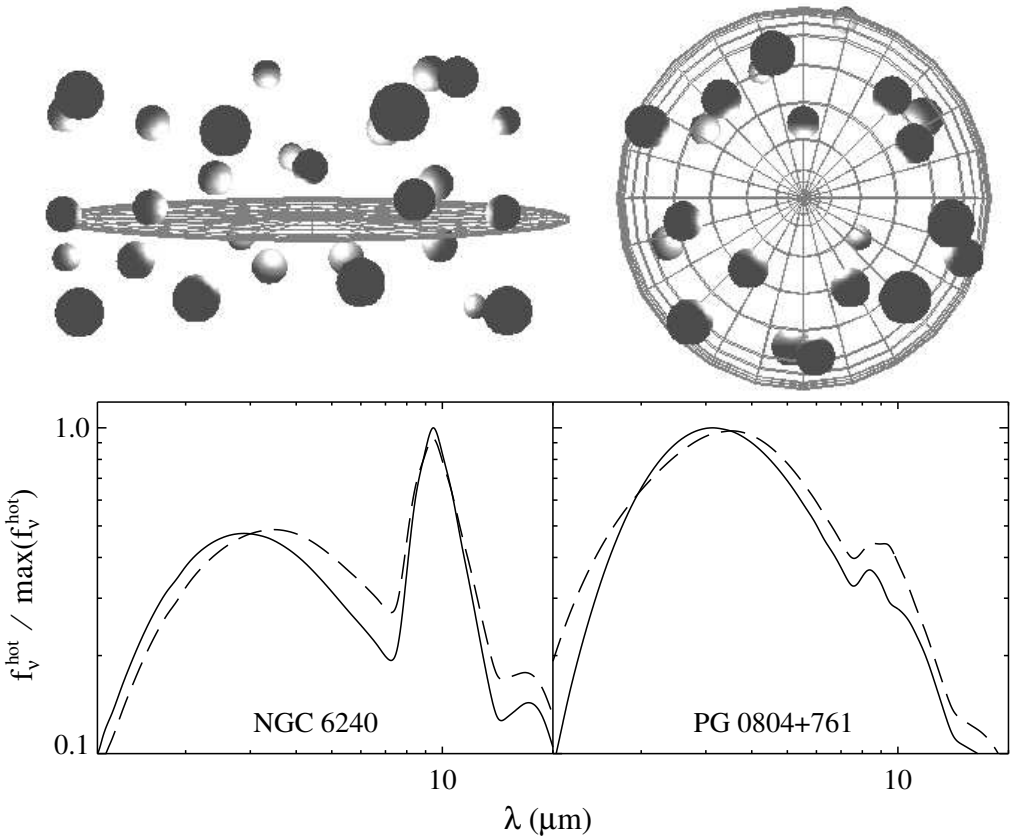

Figure 11.2 Edge-on (*upper-left*) and face-on (*upper-right*) views of a clumpy torus comprised of a toroidal distribution of discrete clouds. Directly illuminated cloud faces (i.e. the sources of *hot* emission) are obscured from most viewpoints by dust on the shaded side of each cloud. SEDs of the fitted NGC 6240 and PG 0804+761 *hot* components are shown beneath the schematic torus model representing their geometry (*solid lines*), along with model SEDs derived assuming that a fraction of the *hot* component emission (50% for NGC 6240 and 75% for PG 0804+761) is obscured by a $\tau_V = 25$ screen, with the remainder emerging unobscured (*dashed lines*).

11.2 Hot Dust Emission from Clumpy AGN Tori

If the obscuring dust surrounding an AGN accretion disk is arranged in a smooth (i.e. non-clumpy) toroidal distribution, then the ∼3–8 μm SEDs of Type-1 sources should be dominated by emission from relatively unobscured *hot* dust (since this

hot dust is viewed directly by the observer, with no intervening material from the torus along the line-of-sight to obscure it). If, however, the obscuring structure is instead composed of discrete clouds distributed in a roughly toroidal shape (i.e. a clumpy torus), then *hot* dust emission is not expected to emerge unobscured. As illustrated in Figure 11.2, the directly illuminated (and therefore hotter) faces of clouds in a clumpy torus always point radially towards the nucleus, and therefore away from the observer. Thus, emission from these hot cloud faces, and therefore *hot* component emission from such sources, is obscured by cooler dust on the shaded sides of clouds. Our decomposition of the quasar PG 0804+761 includes a moderately obscured ($\tau_{9.7} \approx 1.2$) *hot* dust component, consistent with such a clumpy obscuring torus.

The SED of the *hot* dust component from the PG 0804+761 decomposition is shown in the lower-right panel of Figure 11.2. Also shown is a curve representing emission from dust at the temperature of the PG 0804+761 *hot* component, with 75% obscured by a $\tau_V = 25$ screen (i.e. equivalent to the screen obscuring the *AGN* component), and the remaining 25% emerging unobscured. While this model with non-uniform coverage does not exactly reproduce the SED from the fully covered model (in particular at shorter wavelengths), it nonetheless produces a very similar spectrum which would also provide an adequate fit to the PG 0804+761 SED (with suitable small adjustments to the *AGN* and *warm* components). Thus, the SED of *hot* component emission from a highly obscured geometry with a few clear lines-of-sight may appear similar to the emission from a fully covered but less obscured geometry. For a traditional torus made from a smooth dust distribution, *hot* dust emission from a face-on source would emerge unobscured with strong silicate emission features (since there are no shaded sides of clouds to obscure the *hot* emission). Our decomposition of PG 0804+761 does not show such strong features

from the *hot* component, suggesting that its *hot* dust, and possibly that of most Type-1 sources, may therefore be significantly obscured by the shadowed sides of clumpy torus clouds.

The lower-left panel of Figure 11.2 depicts the fitted NGC 6240 *hot* dust component SED (unobscured in the decomposition), along with a model in which 50% of its *hot* dust is covered by a screen with $\tau_V = 25$ and the remainder emerges unobscured. As with PG 0804+761, this partially covered model does not precisely reproduce the fitted *hot* dust component. It is, however, similar enough to the fitted component to provide a reasonably good fit (i.e. since the *hot* component of NGC 6240 contributes in a region with strong contributions from several other components, the small deviations between the two models would not affect the decomposition greatly). The near equivalence of these two models demonstrates that emission from a highly obscured, but only partially covered, geometry may appear quite similar to emission from a fully covered geometry at much lower levels of obscuration. Therefore, despite the small apparent optical depth derived from the fit to NGC 6240, it is possible that the *hot* component in this source is actually much more significantly obscured (i.e. we may only see direct emission from a few clear lines-of-sight, while the majority of the *hot* dust is completely obscured).

11.3 Origin of the Far-IR Emission in AGNs

Since emission from dust at far-IR ($\lambda > 50\,\mu$m) wavelengths is likely to emerge unobscured from galaxies, the average properties of the far-IR SEDs of AGNs (e.g. their relative cold dust luminosities and masses) should be similar for all sources (assuming their nuclei are similarly structured), independent of their orientation-

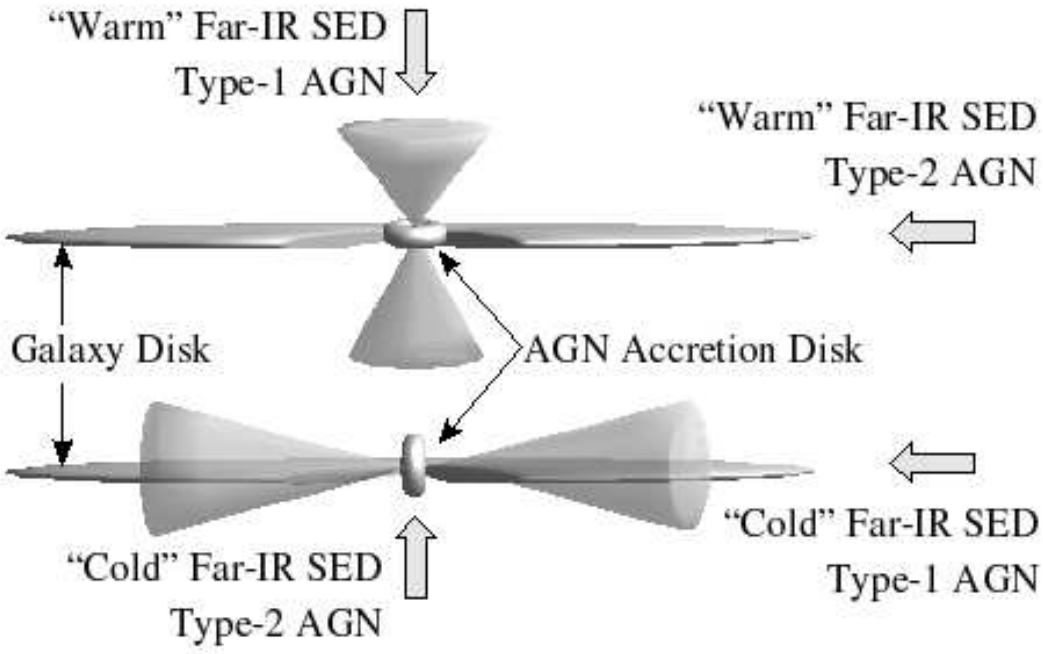

Figure 11.3 If the disk of the host galaxy and the AGN accretion disk are co-planar (*top*), very little dust in the disk of the galaxy is illuminated by the AGN (i.e. the radiation cones from the accretion disk do not intersect the host galaxy disk). In contrast, if the host galaxy and AGN accretion disks are orthogonal (*bottom*), the AGN heats dust over a large area of the galaxy disk (i.e. the radiation cones *do* intersect the host galaxy disk), resulting in far-IR and possibly PAH emission. Broad arrows label the line-of-sights giving rise to the indicated properties of the emergent SEDs for the various geometries.

based (i.e. Type-1 versus Type-2) classification. As described in §10, the two template AGNs in our sample have very different far-IR properties (e.g. Mrk 463 has a dust luminosity-to-mass ratio ∼15 times that of PG 0804+761), in sharp contrast to these expectations. Farrah et al. (2003) use a two-component (starburst+AGN) template decomposition to conclude that some optically classified AGNs with strong far-IR emission likely have significant contributions from starbursts. While this is likely true for many AGNs with cool far-IR SEDs, it does not appear to hold for Mrk 463 (see §10). As illustrated in Figure 11.3, we instead

suggest that the far-IR emission from *some* AGNs (including Mrk 463) is powered by the AGN itself and originates from cool dust in the disk of the host galaxy. We note here that this suggestion is based upon the SEDs of only two AGNs, so further study using a much larger sample (to be presented in a subsequent paper) is needed before conclusions are drawn about the origin of far-IR emission from the class of AGNs.

While it is often assumed that an AGN accretion disk and the disk of the galaxy hosting the AGN are co-planar (as in the top of Fig. 11.3), this geometrical assumption is not necessarily always true. After the merger of two galaxies, the resulting accretion and host galaxy disks may eventually come to rest in the same plane (e.g. due to torques), but there is a period of time after the merger during which their relative orientation is essentially random. If the two disks are tilted with respect to each other, a significant quantity of dust in the disk of the host galaxy may be heated by the AGN out to large radial distances (see the bottom of Fig. 11.3). Assuming that the galaxy disk is not a significant source of opacity, a galaxy therefore appears as a Type-1 or Type-2 AGN depending upon the relative orientation of the obscuring torus with respect to the observer (i.e. the standard AGN unification scenario). Additionally, depending on the relative orientation of the host galaxy and AGN accretion disks (but independent of the orientation of the observer), the source may exhibit weak or strong far-IR emission (i.e. "Warm" or "Cold" far-IR SEDs as labeled in Fig. 11.3). In this model, Mrk 463 and PG 0804+761 are therefore "Cold" and "Warm" far-IR sources, respectively, with emission arising from geometries similar to those in the bottom and top of Figure 11.3, respectively. We note that the geometry suggested here has a similar impact on the SEDs of galaxies as the 'warped-disk' geometry from Sanders et al. (1989).

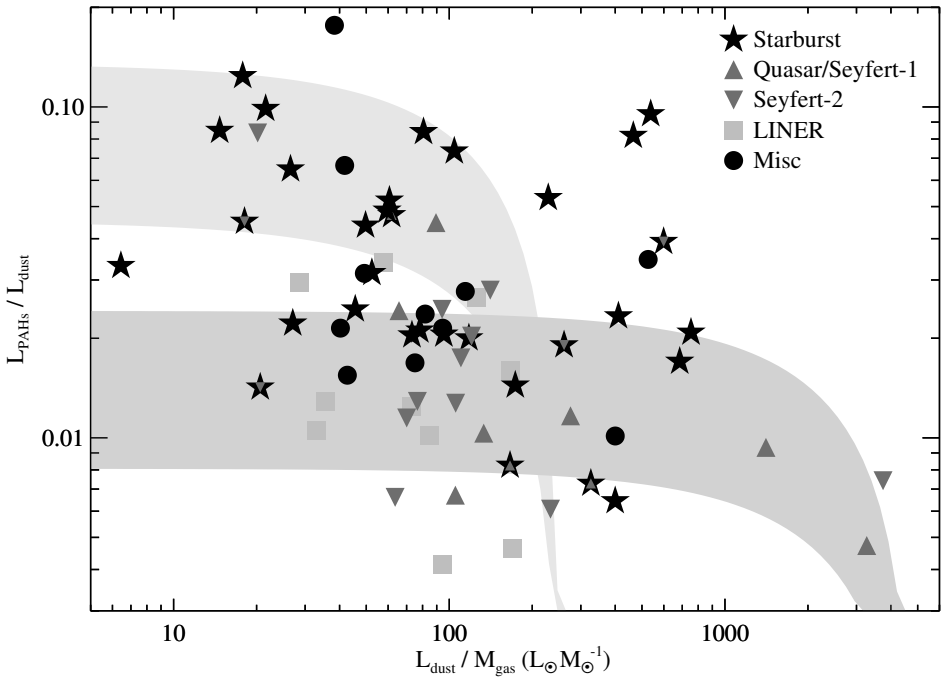

Figure 11.4 The ratio of the total PAH luminosity (integrated over all features) to the total dust luminosity is plotted against the ratio of the total dust luminosity to the total gas mass. Different symbols represent galaxies with the optical classification indicated in the figure legend. The lighter shaded region shows the trend expected if the relative PAH strengths and dust luminosity-to-mass ratios of the template starbursts NGC 7714 and NGC 2623 are linearly extrapolated over the entire sample. The darker shaded region below similarly shows the trend expected if the properties of the template AGNs PG 0804+761 and Mrk 463 are extrapolated over the entire sample.

Figure 11.4 shows the ratio of the total PAH luminosity (integrated over all features) to the total dust luminosity plotted against the ratio of the total dust luminosity to the total gas mass for all sources in our sample with available 70 or 160 μm MIPS data to constrain their far-IR SEDs. From this plot, it is clear that the trend described above concerning the divergent far-IR properties of Mrk 463 and PG 0804+761 holds over a much larger sample of Seyfert galaxies. As described in §9.3.4, the dust luminosity-to-mass ratio is related to the quantity of cold dust

in a galaxy—with larger values indicating less cold dust. Figure 11.4 shows that this ratio varies over two orders of magnitude for the AGNs in our sample, so that the amount of cold dust in AGNs is quite varied. The orientation-dependent standard model of AGN unification predicts that the dust luminosity-to-mass ratio should on average be similar for all AGNs. The considerable evidence in support of this unification picture suggests that it is an accurate portrayal of the nuclei of AGNs. It is for this reason, together with the magnitude of the observed variation in far-IR properties, that we suggest the model shown in Figure 11.3 to provide a simple geometrical argument describing the AGN-powered origin of some far-IR emission emerging from the disks of galaxies.

As described in §10, we estimate that ∼35% of the bolometric luminosity of Mrk 1014 is powered by star-formation. If all of this luminosity emerges in the form of *cool* dust, this still leaves ∼30% of its 70 K emission component to be powered by its AGN. We therefore suggest that the geometry of Mrk 1014 is likely to be similar to that of Mrk 463 (i.e. the bottom of Figure 11.3). Additionally, the luminosity of the Mrk 1014 *PAHs* component compared to its inferred starburst fraction suggests that between ∼20–50% of its PAH emission is powered by its AGN (i.e. derived by comparison with the properties of the obscured starbursts NGC 2623 and NGC 6240—see §10). Schweitzer et al. (2006) argue against AGN powered far-IR emission in a sample of QSOs observed with *Spitzer* based largely on the fact that PAHs are destroyed in a hard AGN radiation field. However, in the geometry of Figure 11.3, the radiation field gradually softens as the photons propagate through the galaxy disk, so that at some radius PAH molecules illuminated by the AGN may survive.

In Figure 11.4, we show two shaded regions to indicate the trends expected

if the relationships between the plotted properties of the two template starbursts (top lighter region) and two template AGNs (bottom darker region) are linearly extrapolated over the entire sample. Although there is no reason to expect that these relationships must be linear, the bands nonetheless envelop the majority of the starburst galaxies and AGNs, respectively. Note that the slopes of the two trends are different, so that the relative PAH luminosities of starbursts and AGNs increase at different rates as a function of the dust luminosity-to-mass ratio for each galaxy class—providing evidence that some of the PAH emission from AGNs is likely powered by the AGN itself and not necessarily star-formation. Clearly, more work is required (e.g. radiative transfer calculations with realistic PAH destruction models) to verify if this scenario is indeed realistic, and we do not dispute that some far-IR emission in AGNs is powered by starbursts, but the suggested mechanism to generation far-IR and PAH emission in AGNs as a result of the interaction of the accretion disk with its host galaxy should be considered as well. *Furthermore, we warn against the blanket assumption that all PAH and far-IR emission is directly associated with star-formation, as this could result in an overestimation of the true level of star-formation activity in galaxies.*

11.4 The Nature of Composite Sources

Much of the recent history of infrared extragalactic astronomy has largely revolved around determining the underlying source of power hidden within obscured dusty galactic nuclei (see §1). Figure 11.5 presents a diagram to aid in diagnosing the AGN and starburst contributions to these galaxies. In the Figure, the equivalent width of the 6.2 μm PAH feature is plotted against the ratio of the total dust luminosity to the total gas mass (both obtained from the decompositions). This

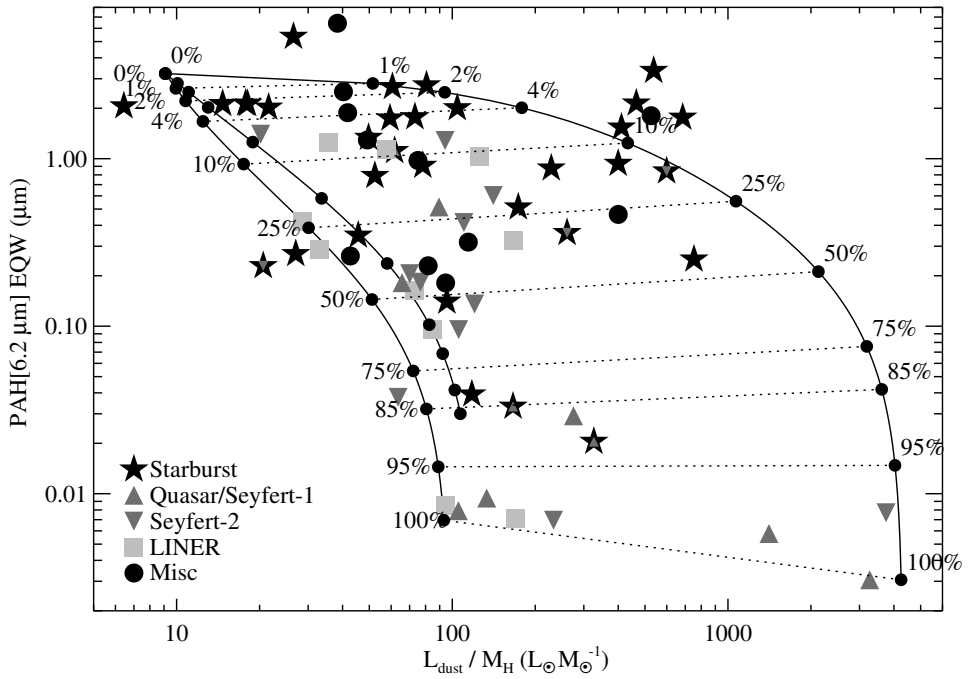

Figure 11.5 The ratio of the equivalent width of the 6.2 μm PAH features is plotted against the ratio of the total dust luminosity to the total gas mass. Different symbols represent galaxies with the optical classification indicated in the figure legend. The curves represent two-component mixing lines between a starburst galaxy and a (1) Type-2 AGN (e.g. Mrk 463—*left*), (2) far-IR-cold Type-1 AGN with PAH emission (e.g. Mrk 1014—*middle*), (3) far-IR-warm Type-1 AGN without PAH emission (e.g. PG 0804+761–*right*). The numbers listed along each mixing line are the AGN percentage at each location.

particular set of quantities has been chosen since both axes are relatively independent of extinction *if* the extinction diminishes both the PAH and continuum emission simultaneously (which certainly need not be true for all sources). Also shown in Figure 11.5 are three mixing lines. The left line is a linear mix of a starburst galaxy and a Type-2 AGN with a far-IR SED similar to that of Mrk 463. The numbers listed along each mixing line are the AGN percentage at each location. The center line is a mixture of a starburst galaxy and a Type-1 far-IR-cold AGN

with PAH emission, similar to Mrk 1014. The right line is a mixture of a starburst galaxy and a Type-1 far-IR-warm AGN, similar to PG 0804+761. This diagnostic diagram provides sensible results (i.e. known starbursts are towards the top of the plot, and known AGNs are generally towards the bottom), although the diagnoses are by no means certain (see the following).

As discussed in §11.3, the amount of AGN-powered PAH emission emerging from a particular galaxy is quite uncertain, since it is unknown if AGNs are at all capable of powering PAH emission (we suggest in §11.3 that they can, in some circumstances). The two mixing lines on the left of Figure 11.5 illustrate the ambiguity that arises from this uncertainty. If it is assumed that a source which is entirely powered by an AGN has *no* PAH emission (as in the leftmost line), then the derived AGN fraction for a particular source will typically be lower than if one assumes that some PAH emission may emerge from a pure AGN (i.e. as in the center mixing line of Fig. 11.5). Despite this, either mixing line produces fairly consistent results (i.e. as to whether a source is *dominated* by an AGN or not). *However, we caution that care must be taken not to over-interpret the exact strength of an AGN based upon this (or any other) diagnostic diagram, since the baseline properties of starbursts and AGNs are as yet not sufficiently well-understood.* Note that the absence of points in the right half of Figure 11.5 is not significant, but is simply a result of the fact that most sources in our sample are ULIRGs, which are heavily biased towards low dust luminosity-to-mass ratios (i.e. they are fairly "cold" sources).

Chapter 12

Summary and Outlook

We have presented a new multi-component spectral energy distribution decomposition method, and demonstrated its effectiveness for studying the SEDs of composite dusty galaxies. We note that the method is quite general, and may also be applicable to much broader classes of galactic and extragalactic sources. To demonstrate the efficacy of the method, we have applied it to the ultraviolet through millimeter wavelength SEDs of a large sample of 108 dusty galaxies obtained as part of the *Spitzer* GTO program.

In comparing the SEDs of our starburst galaxies, we find that their spectral properties are quite heterogeneous. *We demonstrate that many of the differences in their properties (including the luminosities and masses of their dust components and the strength of their PAH emission) can largely be explained in terms of the different mean optical depth through the dusty cocoons surrounding their newly formed stars.* We similarly find that the far-IR SEDs of AGNs are quite heterogeneous. *We suggest this may result from variations in the relative orientation of their host galaxy and AGN accretion disks, such that differing amounts of AGN-heated cold dust emission emerge from their host galaxies.*

We also study in detail two known composite sources. As our first case study, our decomposition of NGC 6240 finds very little evidence for an AGN contribution ($\sim$2%), with *the total dust emission from NGC 6240 being powered by a starburst having mean optical depth* $\tau_V \approx 5$. We note, however, that we cannot rule out a larger contribution from a deeply embedded AGN visible only in X-rays. As our second case study, we find that *the SED of Mrk 1014 is consistent with a galaxy*

which is $> 65\%$ *AGN powered, with a* $< 35\%$ *contribution from star-formation.* Like Mrk 463, we find that Mrk 1014 has a far-IR excess (compared to the Type-1 AGN PG 0804+761), and attribute this to cold dust in the disk of its host galaxy which is heated directly by its AGN. *We also estimate that up to 50% of the detected PAH emission in Mrk 1014 may be powered by radiation from the AGN that has softened as it propagates through the galaxy disk (so that it does not destroy the fragile PAH molecules).*

The large library of fitted SEDs presented in this dissertation provide a suite of templates to aid in future studies aimed at understanding both the local dusty galaxy population and the high-redshift LIRGs and ULIRGs now being uncovered by *Spitzer*. Although some of the mysteries hidden beneath the dusty layers of the very dusty parts of the universe discussed in this dissertation have been partially unveiled, true understanding still remains largely elusive. While there is hope that additional work in the infrared will prove profitable, for many of the most heavily obscured sources, it is likely that progress will require new observations at penetrating X-ray wavelengths. This still is a challenging endeavor, although one in which progress can be made—e.g. the positive detection of X-ray emission from NGC 6240 in 8.8 ksec of integration (Lira et al. 2002). As with any scientific field worthy of study, there is still much work to be done to understand dusty galaxies.

Appendix A

Weighting of Variably Sampled Data

The sampling term, $\hat{\Lambda}$, in equation (2.3), is required to produce sensible and fair fits of non-uniformly sampled data, as is the case when coarsely sampled photometry is joined together with spectral data. If such a term is excluded (i.e. $\hat{\Lambda}_k = 1$ for all λ_k), then χ^2 will be dominated by the more finely sampled spectral data, simply because it contains many more data points. To establish a weighting scheme for non-uniformly sampled data, we define the quantity

$$n_{\mathrm{IRS}} \equiv N_{\mathrm{IRS}} / \log(\lambda^{\mathrm{IRS}}_{\mathrm{max}} / \lambda^{\mathrm{IRS}}_{\mathrm{min}}), \tag{A.1}$$

which is the number of spectral samples per logarithmic wavelength interval in an IRS spectrum. Here, N_{IRS} is the total number of spectral samples in the IRS spectrum, and $\lambda^{\mathrm{IRS}}_{\mathrm{min}} \equiv \min(\lambda_{\mathrm{IRS}})$ and $\lambda^{\mathrm{IRS}}_{\mathrm{max}} \equiv \max(\lambda_{\mathrm{IRS}})$, where λ_{IRS} is the array of wavelength points in the IRS spectrum. We then divide the full SED into N_{bins} wavelength bins (typically 10), distributed in even logarithmic wavelength intervals, with each bin $l \in [0, 1, \ldots, N_{\mathrm{bins}} - 1]$ containing minimum and maximum wavelengths

$$\lambda^{l}_{\mathrm{min}} \equiv \min(\lambda_l) = \lambda_{\mathrm{min}} \left(\frac{\lambda_{\mathrm{max}}}{\lambda_{\mathrm{min}}} \right)^{l/N_{\mathrm{bins}}} \tag{A.2}$$

and

$$\lambda^{l}_{\mathrm{max}} \equiv \max(\lambda_l) = \lambda_{\mathrm{min}} \left(\frac{\lambda_{\mathrm{max}}}{\lambda_{\mathrm{min}}} \right)^{(l+1)/N_{\mathrm{bins}}}, \tag{A.3}$$

where $\lambda_{\mathrm{min}} \equiv \min(\lambda)$ and $\lambda_{\mathrm{max}} \equiv \max(\lambda)$ are the minimum and maximum wavelength in the SED having wavelength array λ. Each bin is then assigned a total weight based upon the sampling of the IRS spectrum

$$\Lambda^{l}_{\mathrm{bins}} = n_{\mathrm{IRS}} \log \left(\frac{\lambda^{l}_{\mathrm{max}}}{\lambda^{l}_{\mathrm{min}}} \right) = \frac{N_{\mathrm{IRS}}}{N_{\mathrm{bins}}} \frac{\log(\lambda_{\mathrm{max}} / \lambda_{\mathrm{min}})}{\log(\lambda^{\mathrm{IRS}}_{\mathrm{max}} / \lambda^{\mathrm{IRS}}_{\mathrm{min}})}. \tag{A.4}$$

The weight of bins containing no data points is redistributed to the nearest bins containing data above and below, with the weight going to each bin being a linear function of the proximity to the bin with no data; i.e. for a bin l' containing no data, the weight distributed to the bins l'_+ and l'_- above and below is

$$\delta\Lambda_{\rm bins}^{l'\rightarrow l'_+} = \Lambda_{\rm bins}^{l'}\frac{l'_+ - l'}{l'_+ - l'_-} \quad \text{and} \quad \delta\Lambda_{\rm bins}^{l'\rightarrow l'_-} = \Lambda_{\rm bins}^{l'}\frac{l' - l'_-}{l'_+ - l'_-}. \tag{A.5}$$

The weighting in each bin is then distributed to the data points within that bin, so that for a data point at wavelength k which is in bin l

$$\Lambda_{k\in l} = \frac{\Lambda_{\rm bins}^{l}}{N_l}, \tag{A.6}$$

where N_l is the number of data points in bin l. Thus, the Λ_k represent the number of effective spectral samples that each data point represents so that the sampling over the entire SED is equivalent to the IRS sampling. Finally, we normalize and scale the weighting function

$$\hat{\Lambda}_k = N_{\rm tot}\frac{\Lambda_k}{\sum_k \Lambda_k}, \tag{A.7}$$

so that $\sum_k \hat{\Lambda}_k = N_{\rm tot} = N_{\rm phot} + N_{\rm IRS}$, the total number of data points in the spectral energy distribution, as would be the case if the weighting function were taken to be unity at all wavelengths (i.e. $\hat{\Lambda}_k = 1$ for all λ_k).

Appendix B

IRS Statistical Flux Density Uncertainty

We derive the statistical flux density uncertainty at each wavelength element of an IRS spectrum by differencing two spectra obtained at different nod positions of each slit. The initial estimate of the uncertainty at each wavelength is

$$\delta f_k = \frac{f_1(\lambda_k) - f_2(\lambda_k)}{(\sqrt{2})^2}, \tag{B.1}$$

where f_1 and f_2 are the observed flux densities in nod positions 1 and 2, and the two factors of $\sqrt{2}$ both correct for the introduction of noise resulting from the subtraction, and account for the reduction in noise of the final flux densities resulting from averaging the two nods. At each wavelength, this array contains a single sample of the true uncertainty drawn from the probability distribution function having standard deviation $\sigma(\lambda_k)$. We estimate the true value of the statistical uncertainty at each wavelength by calculating the standard deviation of the points in a window of width W (typically around 20 wavelength bins, with the window size decreasing near the edges of the spectrum), and assigning this value as the standard deviation of the central wavelength, i.e.

$$\sigma^2(\lambda_k) = \frac{1}{W+1} \sum_{i=k-W/2}^{k+W/2} \left[\delta f_i - \langle \delta f \rangle\right]^2, \tag{B.2}$$

where $\langle \delta f \rangle \approx 0$ is the mean value of δf for the points within the window. Since we are approximating a function which in principle should be sampled on an infinitely fine grid, our estimated σ array will always show some residuals from our finite grid size. As a result, the σ array does not always have the expected property that $\sim$68% of the δf_k are enveloped by the 1–σ contour. We therefore perform one final step, smoothing our estimated σ array with a window of width W, and scaling the

entire array until it has the expected behavior that the 1–σ error contour envelops 68% of the δf_k.

Appendix C

Starburst Decompositions

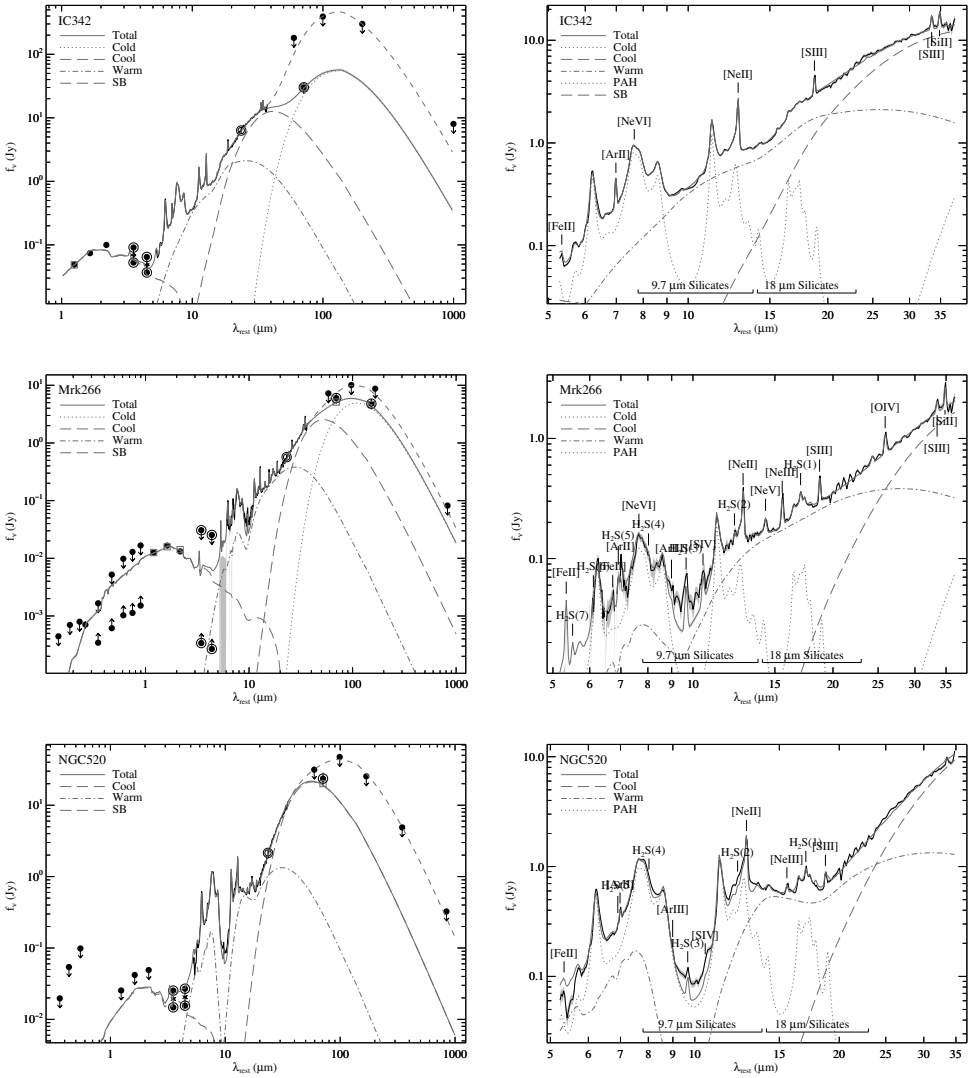

Figure C.1 Spectral decompositions of the ultraviolet to millimeter wavelength SEDs of the starburst galaxies in our sample. Labeling and annotations are as in Figs. 9.1 and 9.2.

Figure C.2 (Continued)

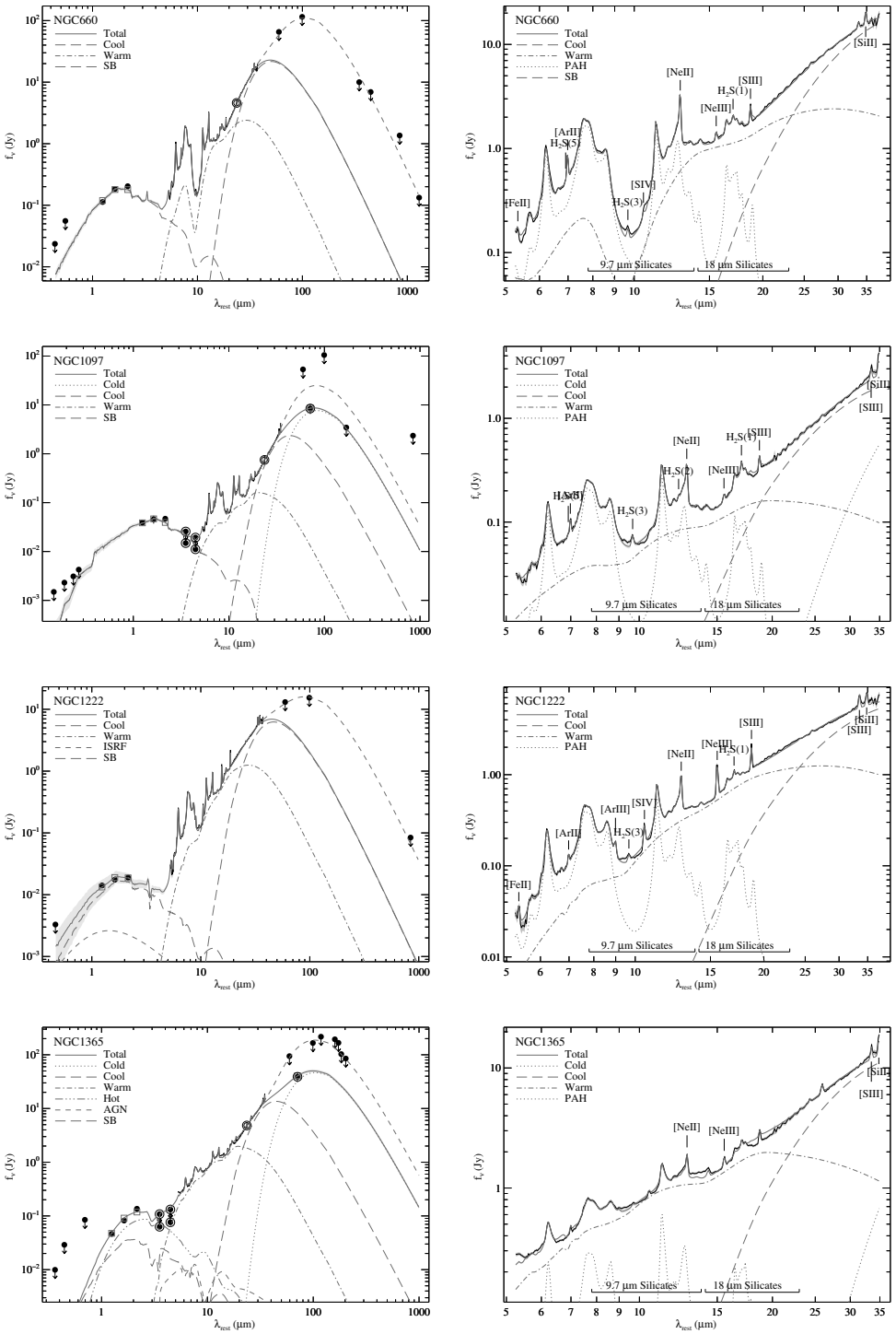

Figure C.2 (Continued)

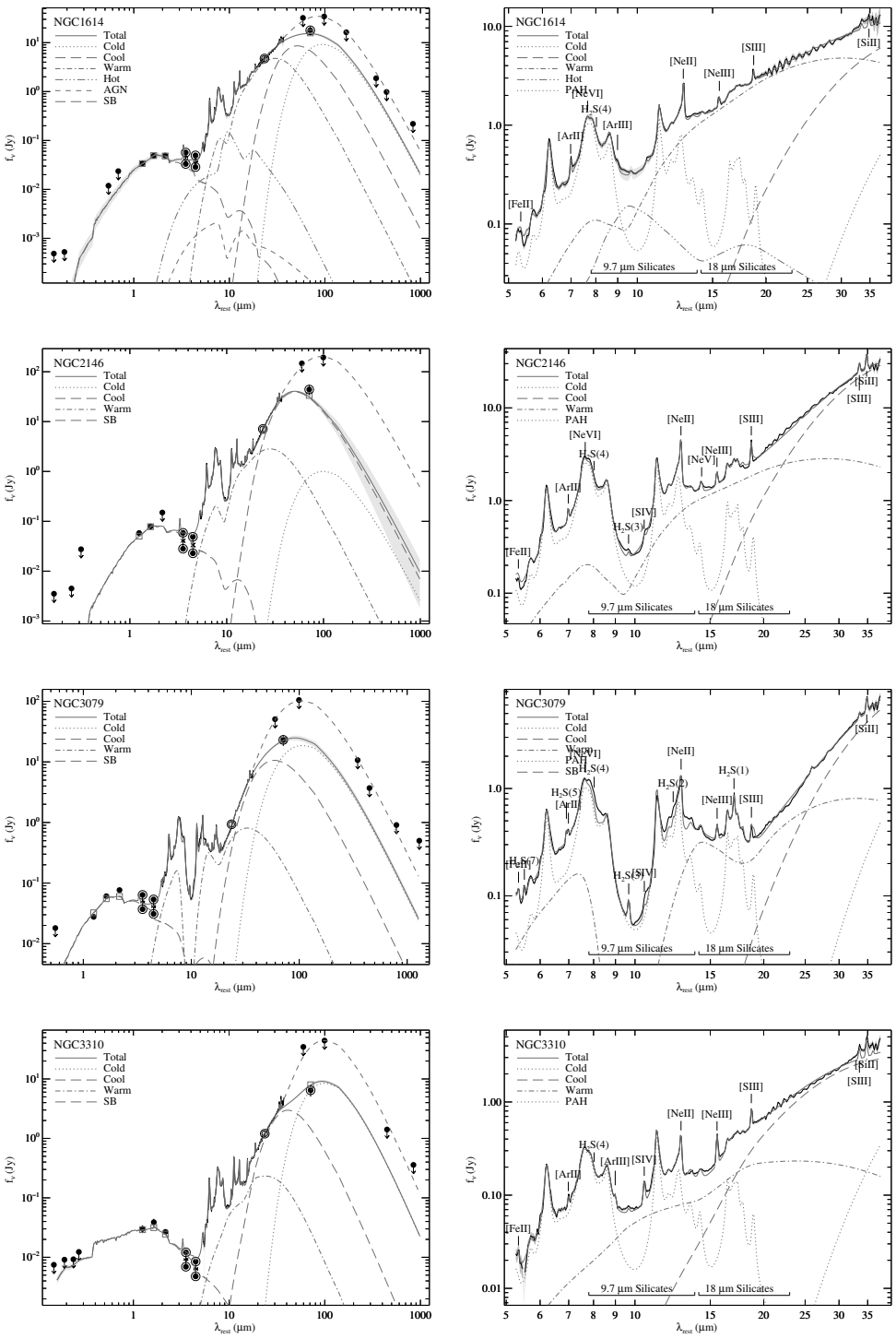

Figure C.2 (Continued)

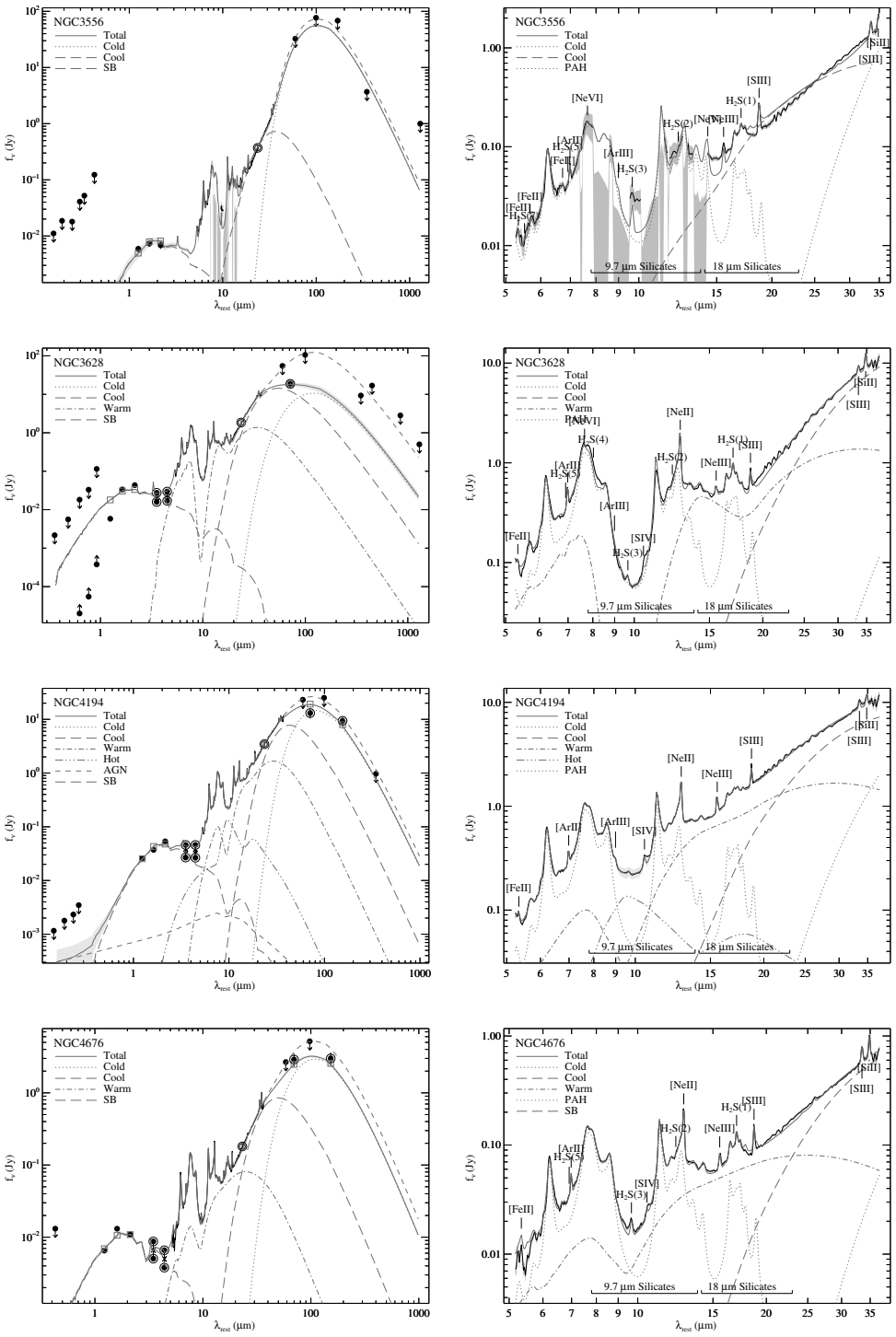

Figure C.2 (Continued)

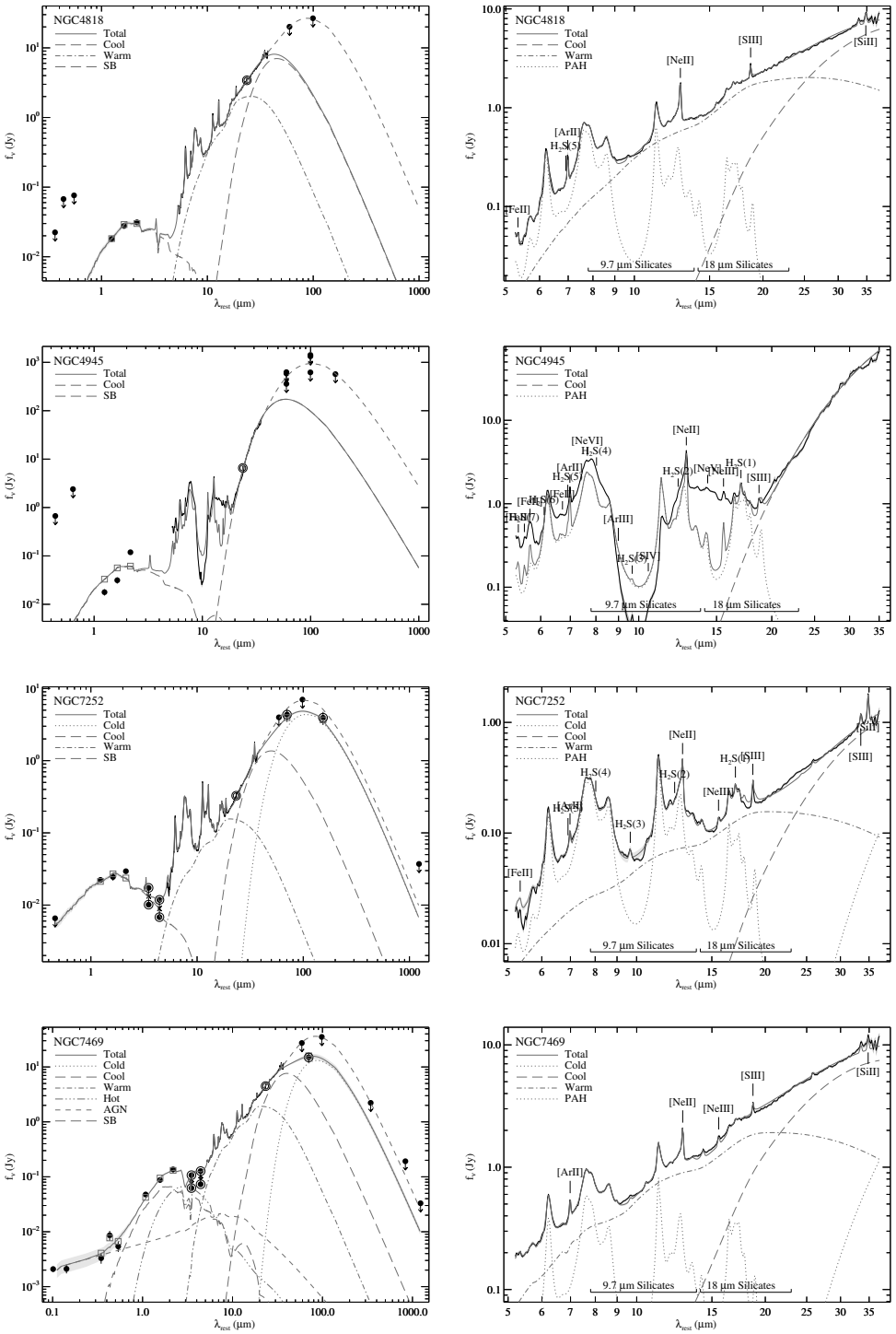

Appendix D

AGN Decompositions

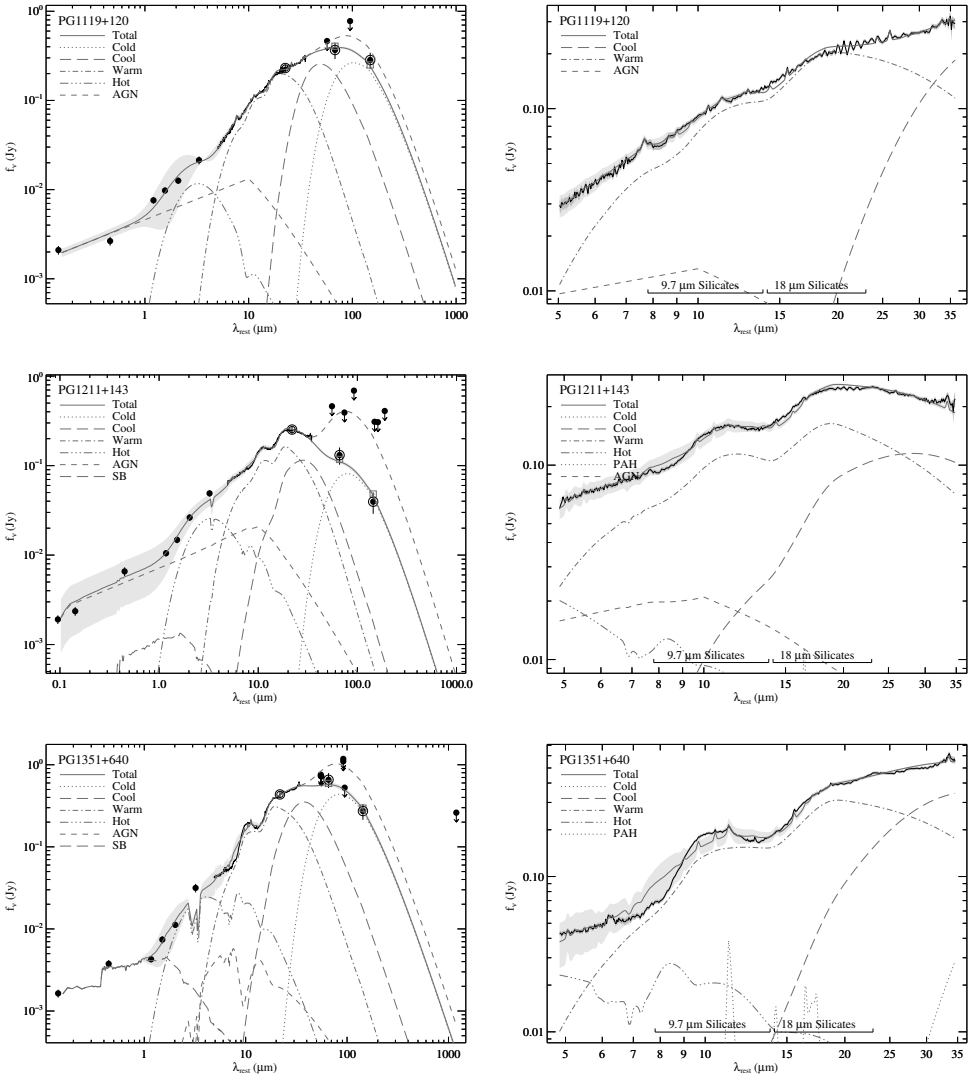

Figure D.1 Spectral decompositions of the ultraviolet to millimeter wavelength SEDs of the AGNs in our sample. Labeling and annotations are as in Figs. 9.1 and 9.2.

Figure D.2 (Continued)

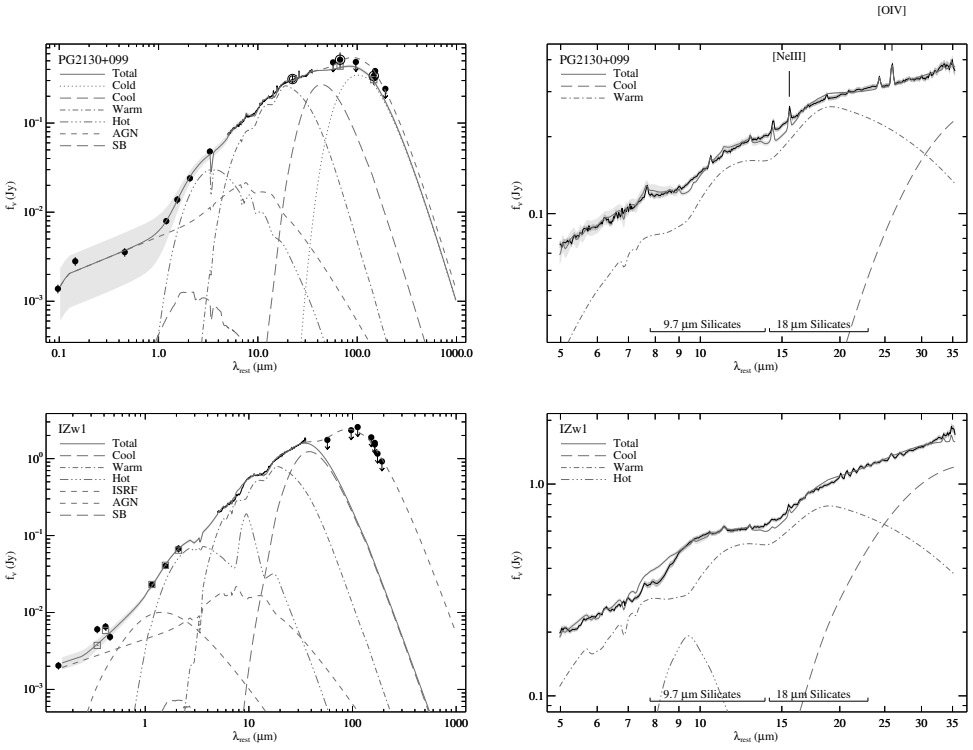

Appendix E

ULIRG Decompositions

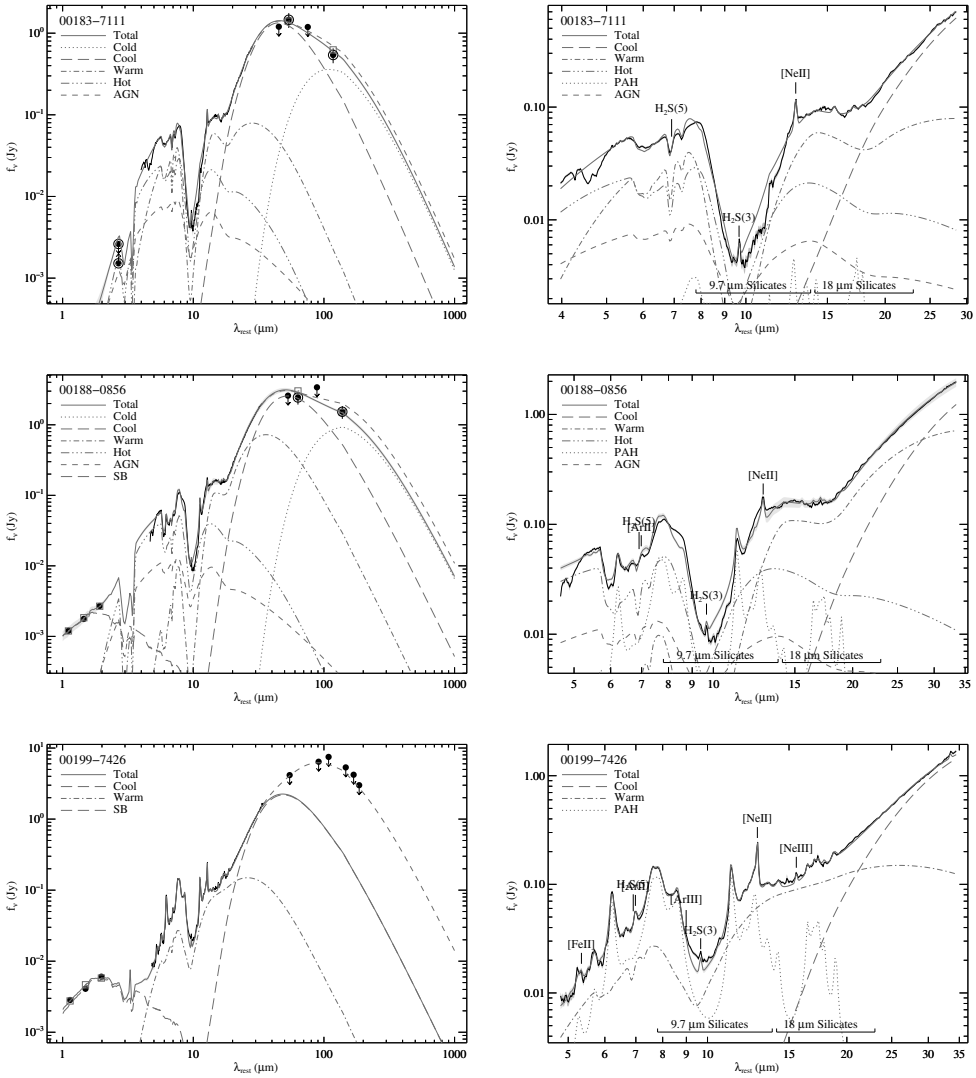

Figure E.1 Spectral decompositions of the ultraviolet to millimeter wavelength SEDs of the ULIRGs in our sample. Labeling and annotations are as in Figs. 9.1 and 9.2.

Figure E.2 (Continued)

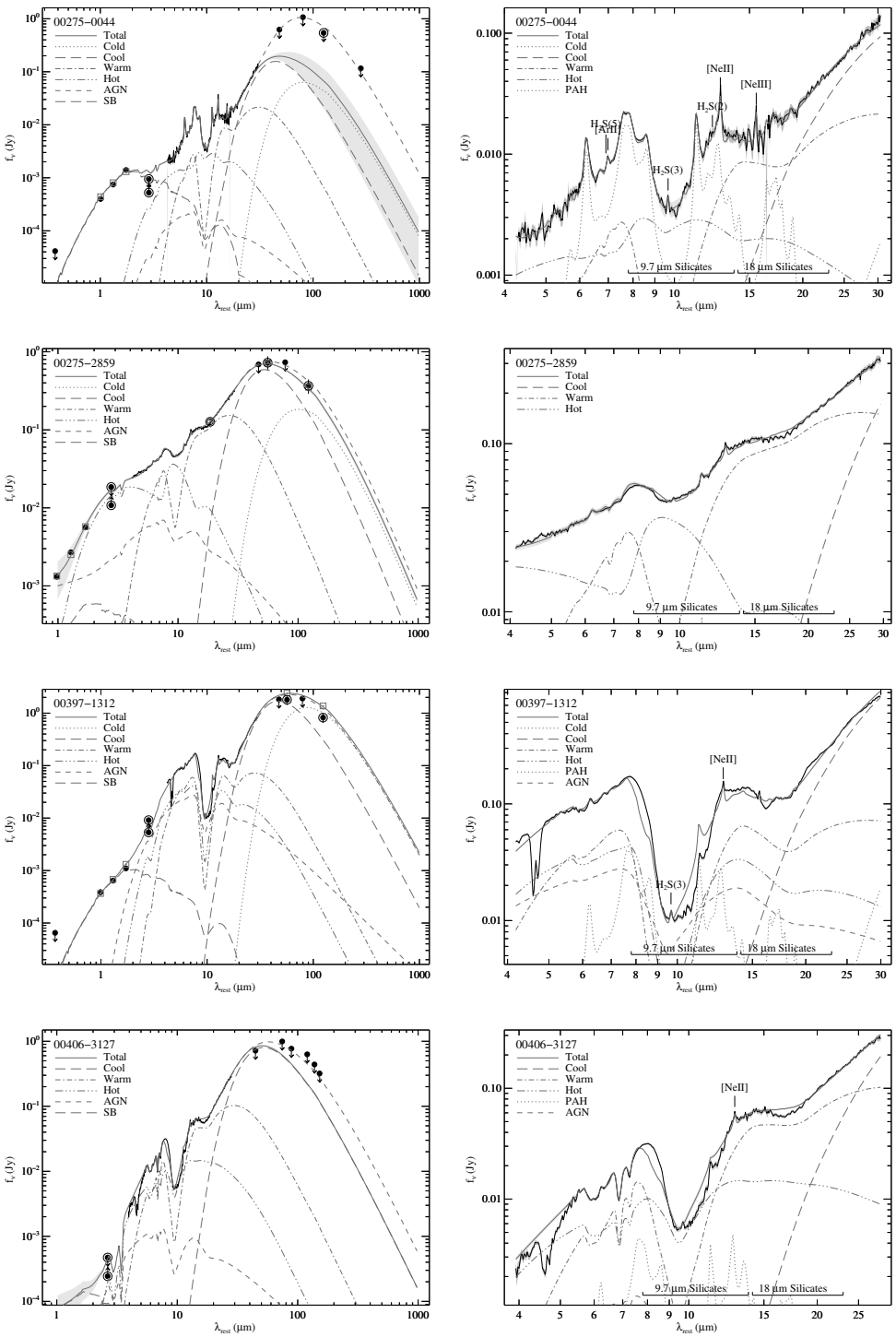

Figure E.2 (Continued)

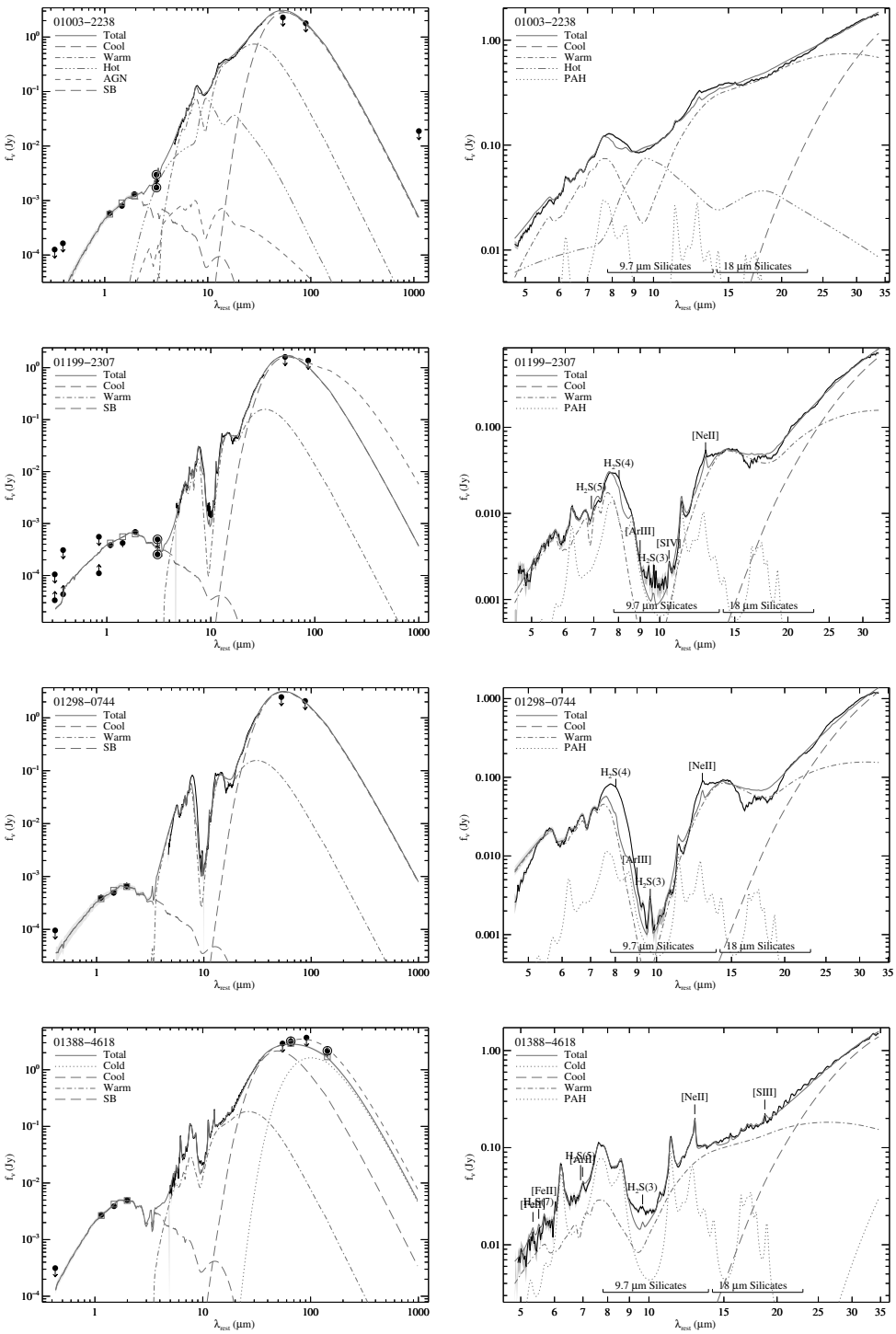

Figure E.2 (Continued)

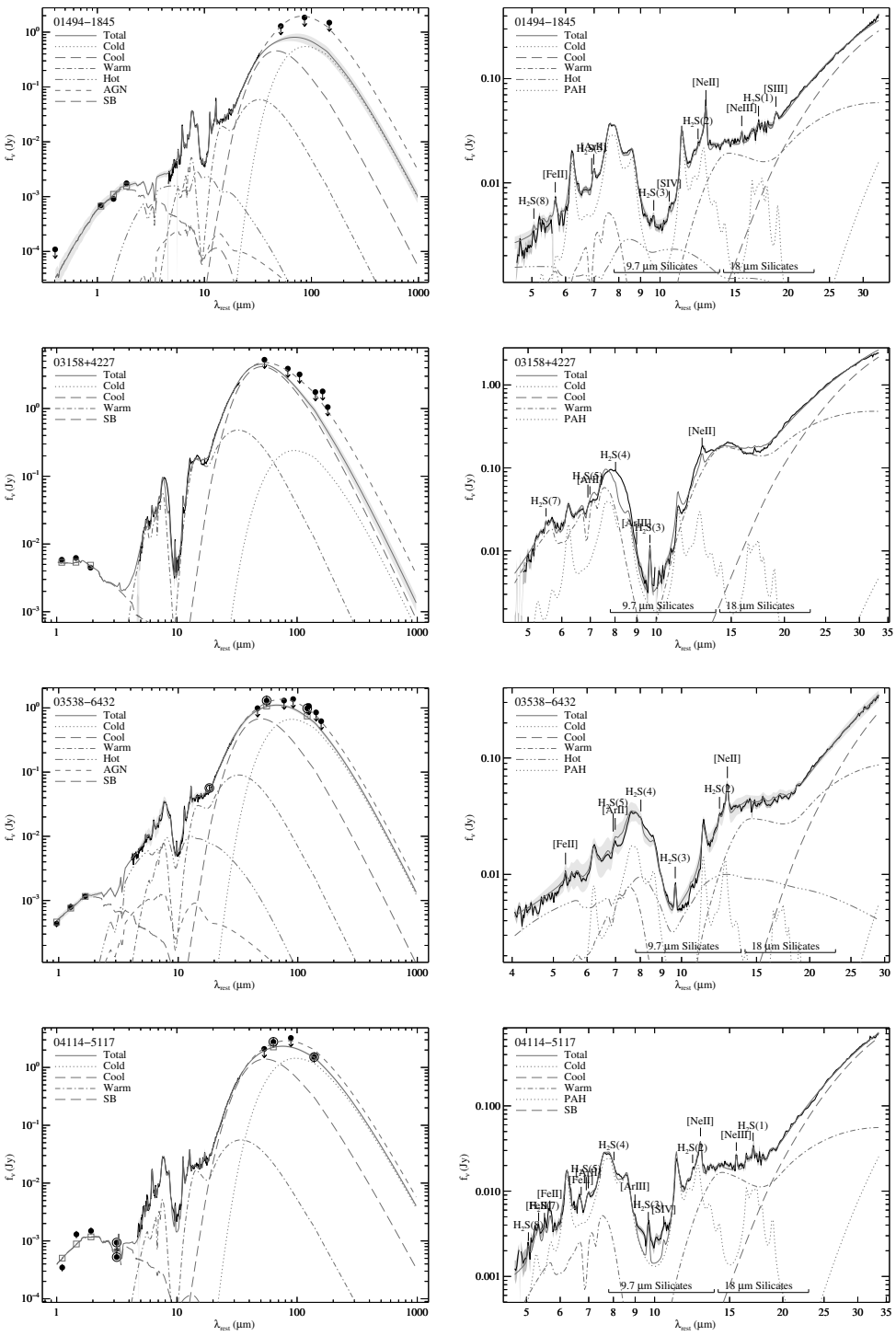

Figure E.2 (Continued)

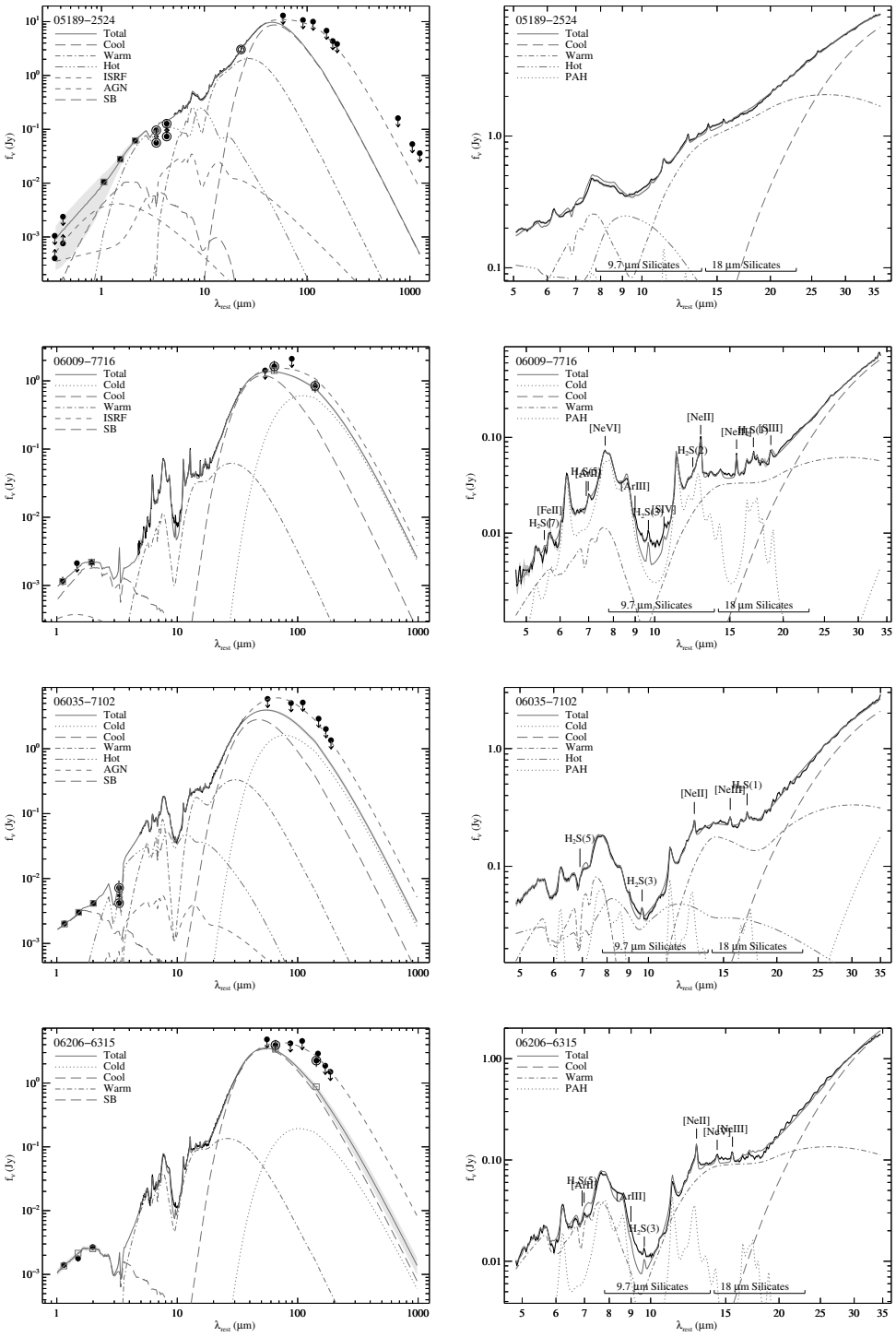

Figure E.2 (Continued)

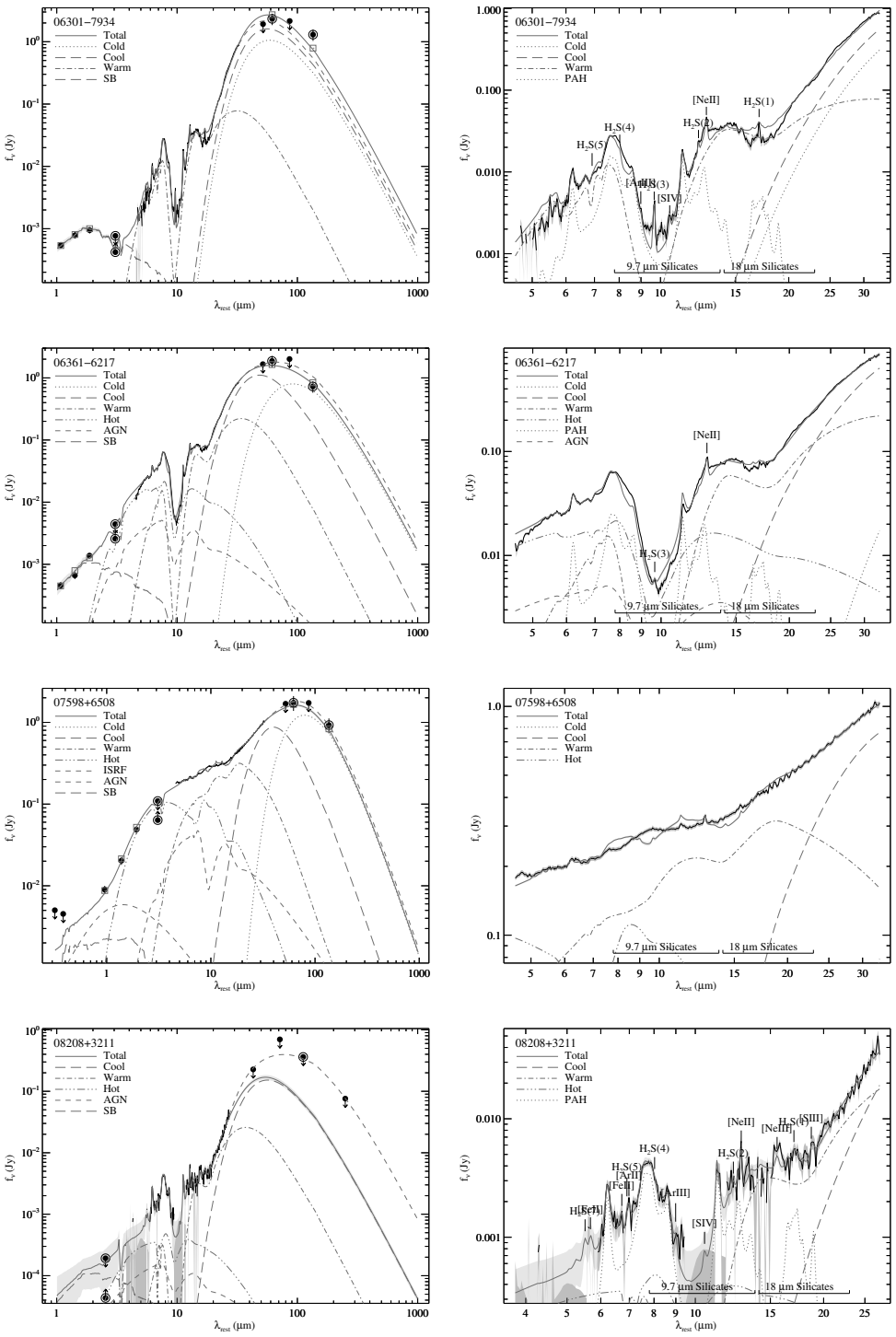

Figure E.2 (Continued)

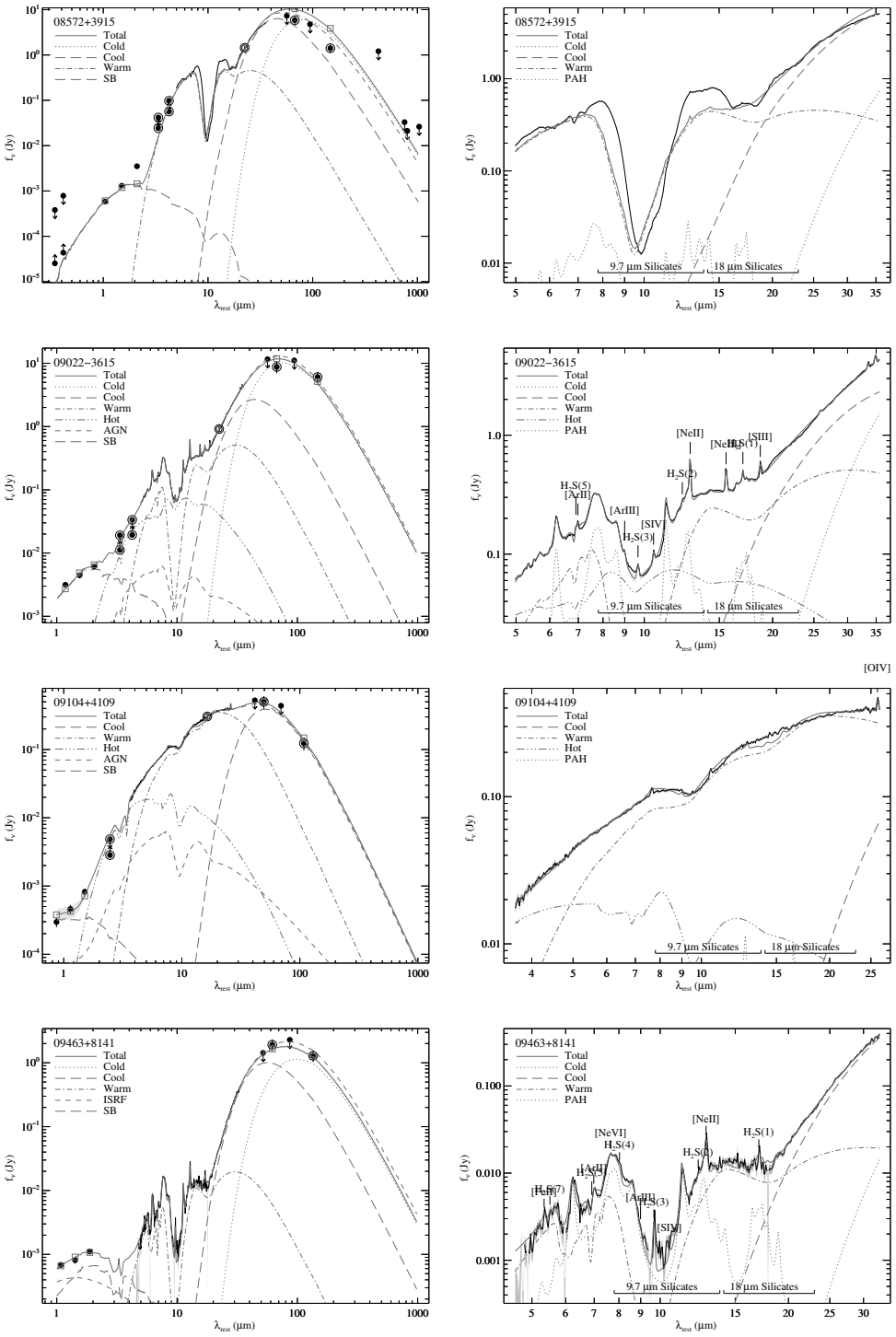

Figure E.2 (Continued)

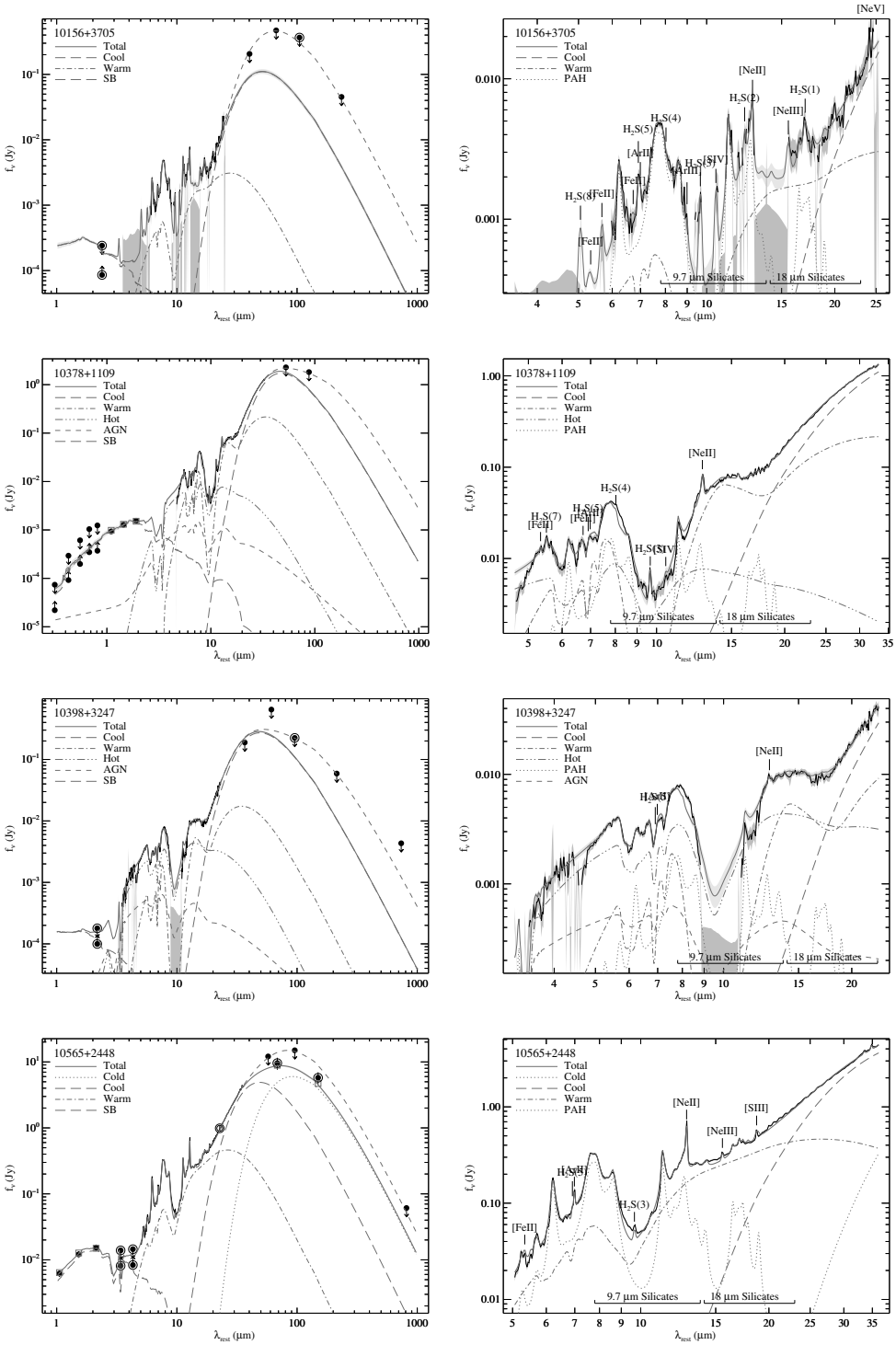

Figure E.2 (Continued)

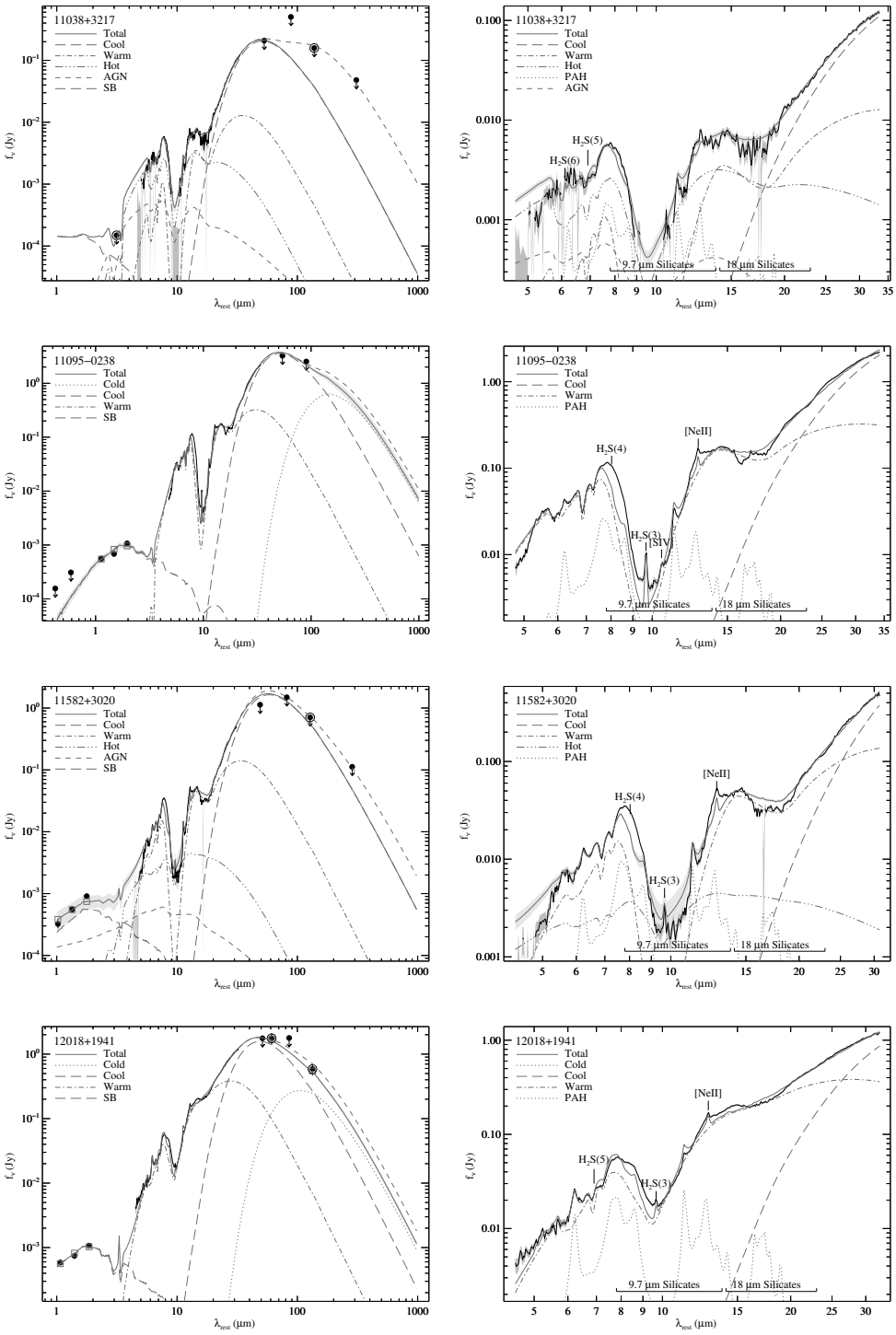

Figure E.2 (Continued)

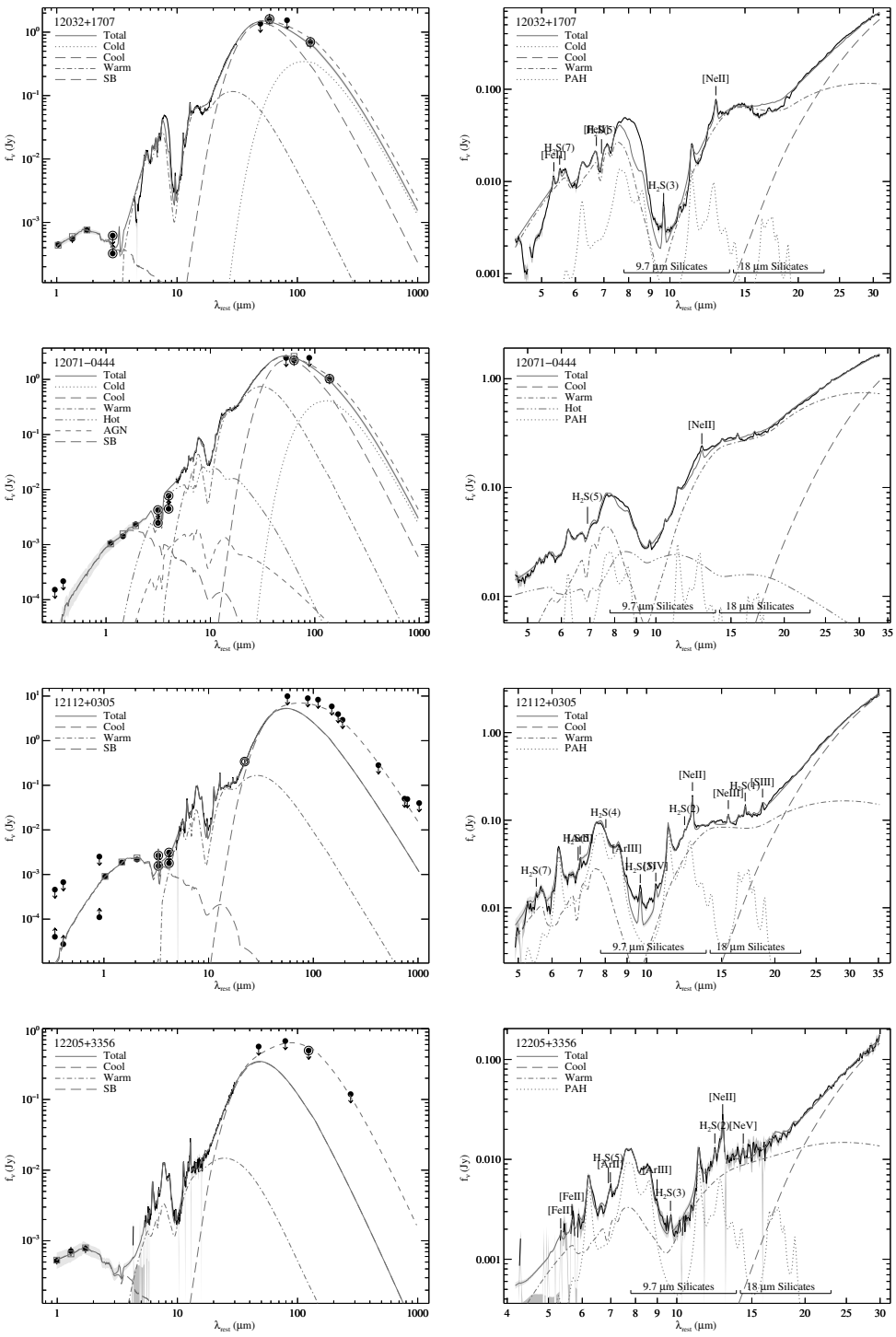

Figure E.2 (Continued)

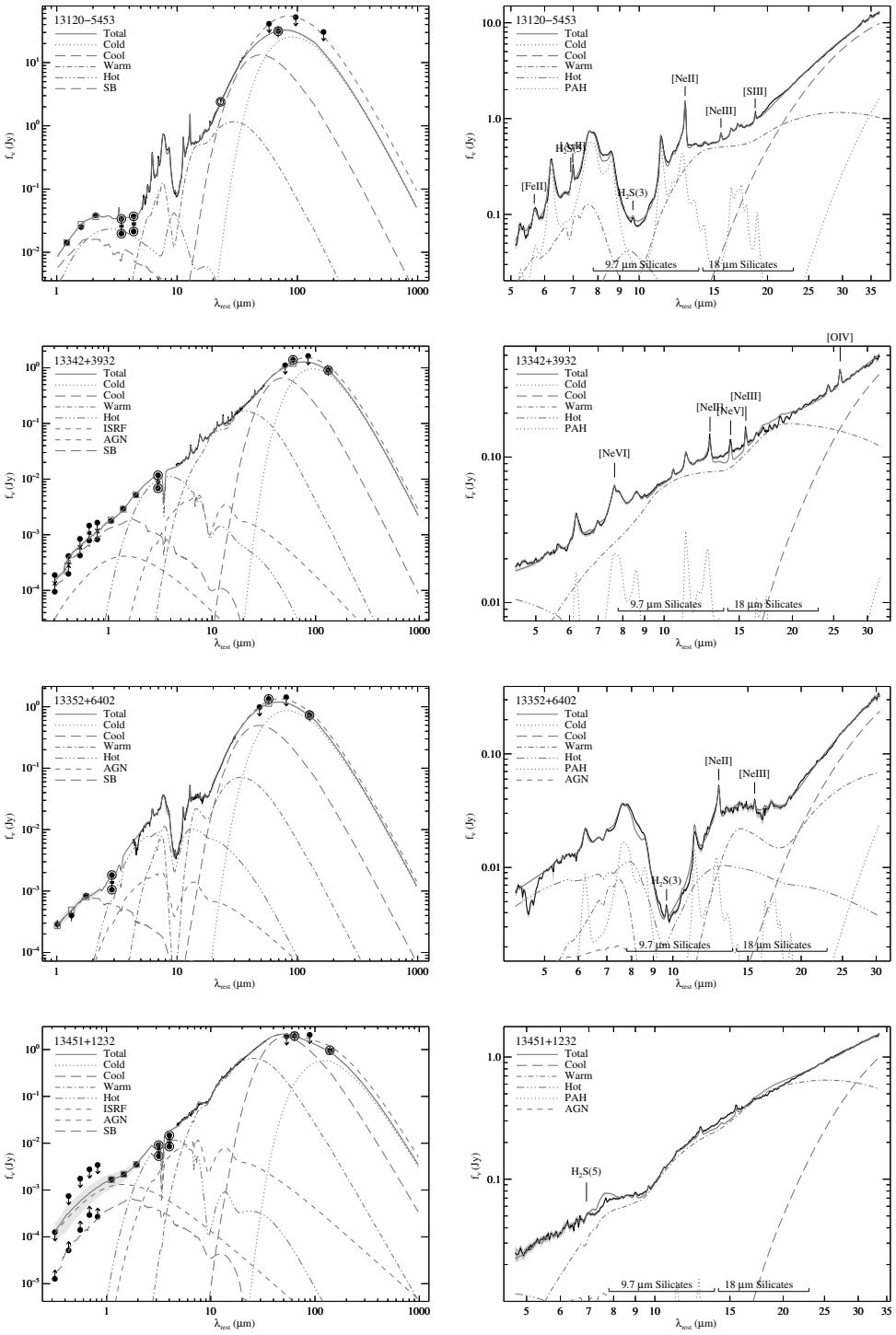

Figure E.2 (Continued)

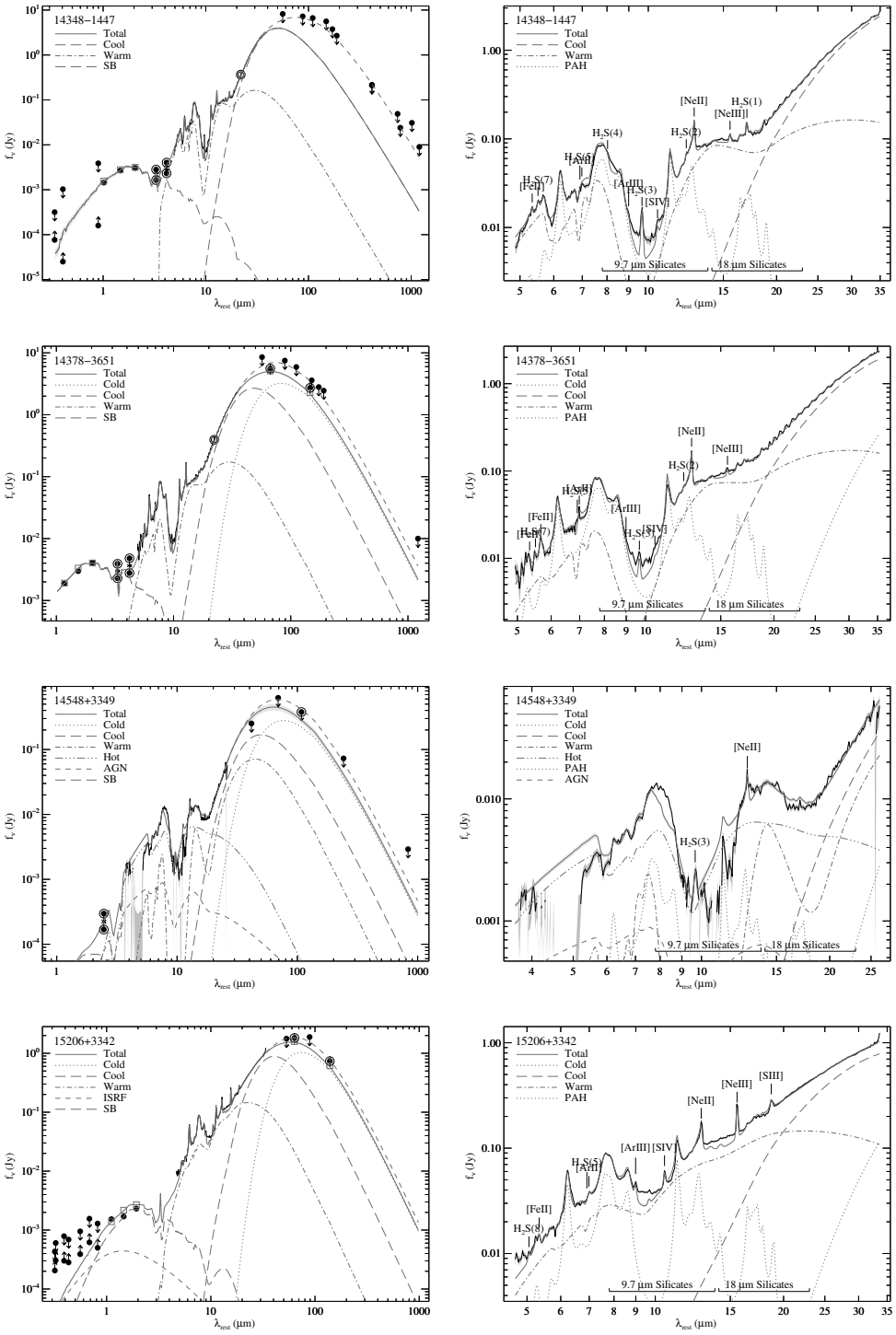

Figure E.2 (Continued)

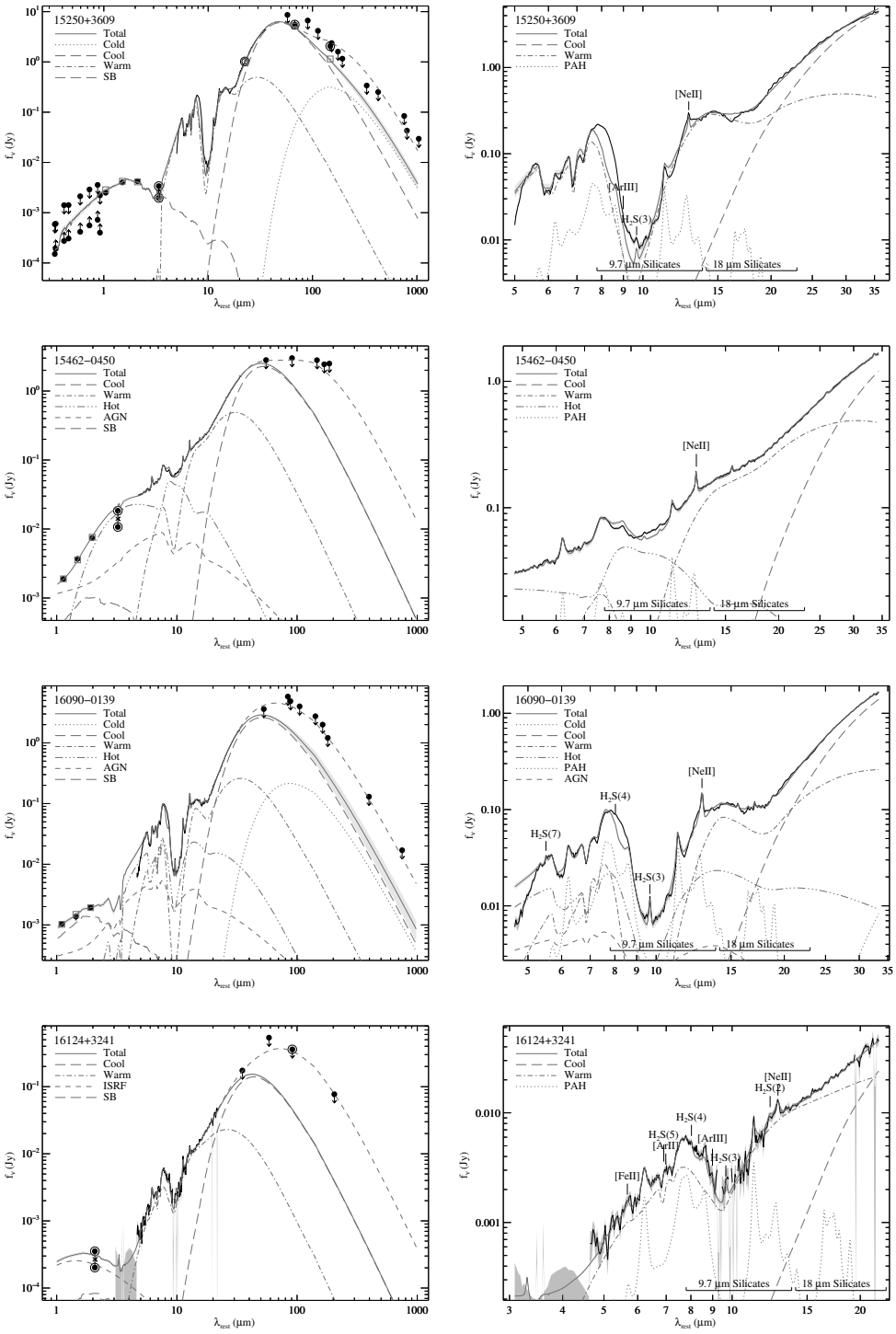

Figure E.2 (Continued)

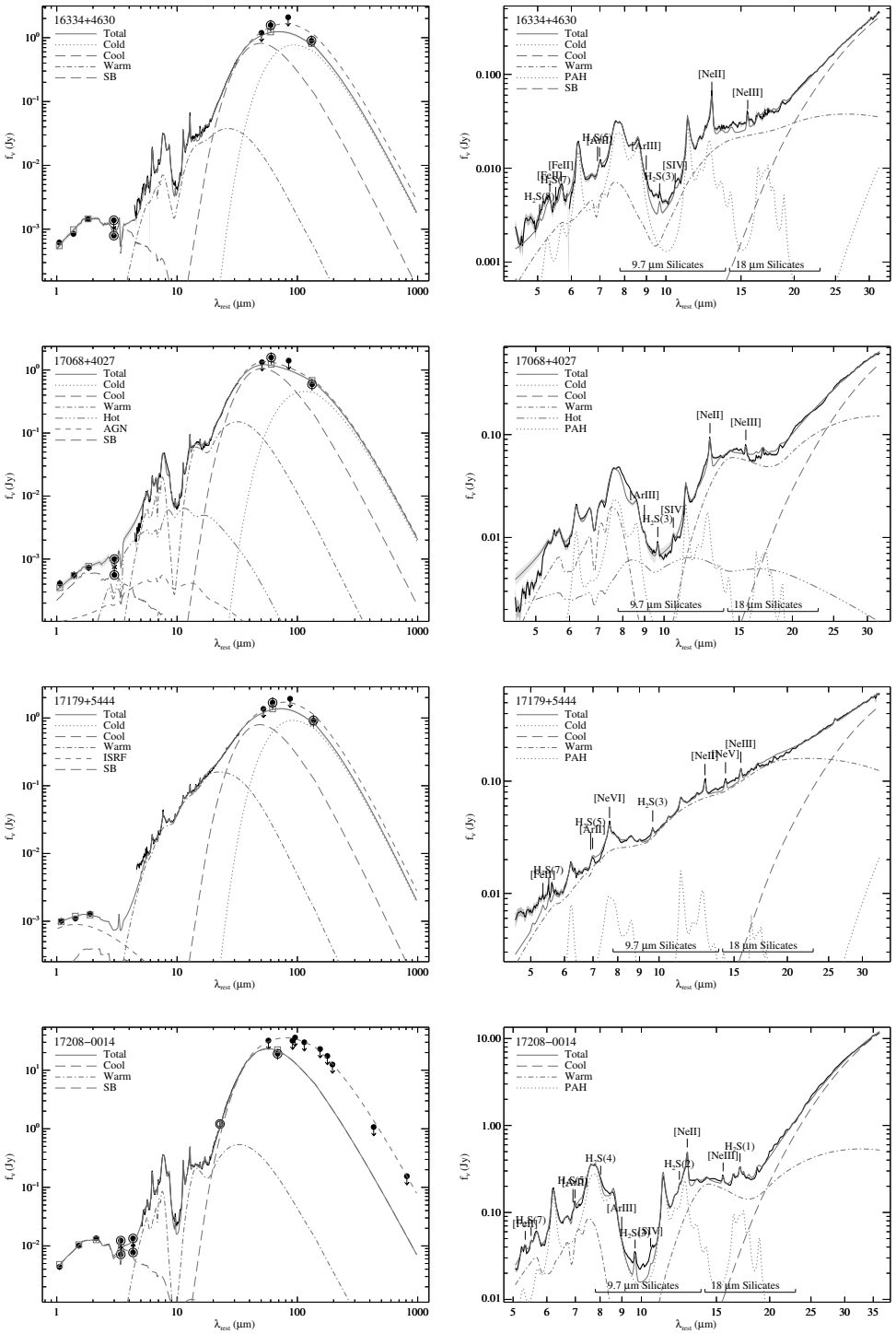

Figure E.2 (Continued)

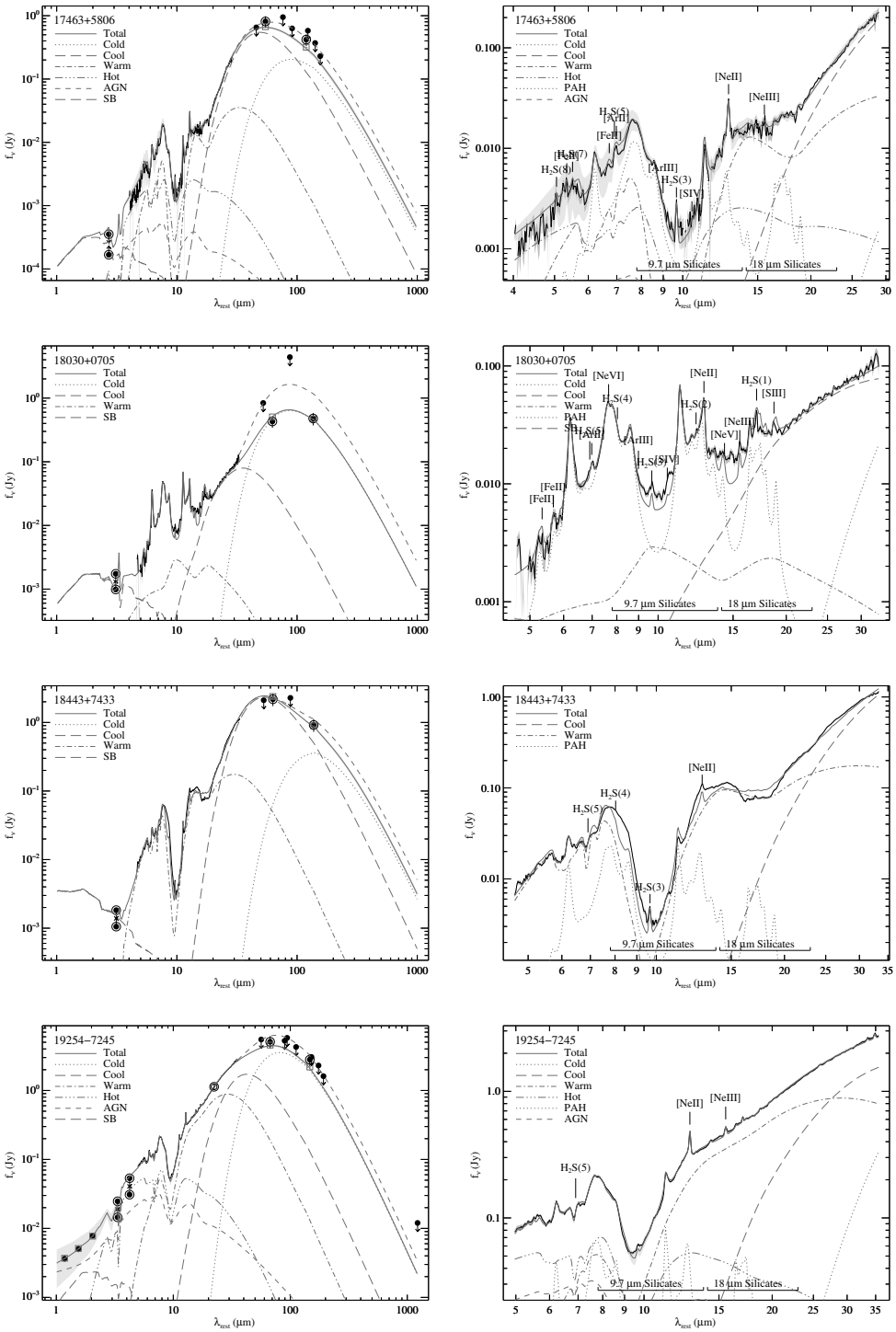

Figure E.2 (Continued)

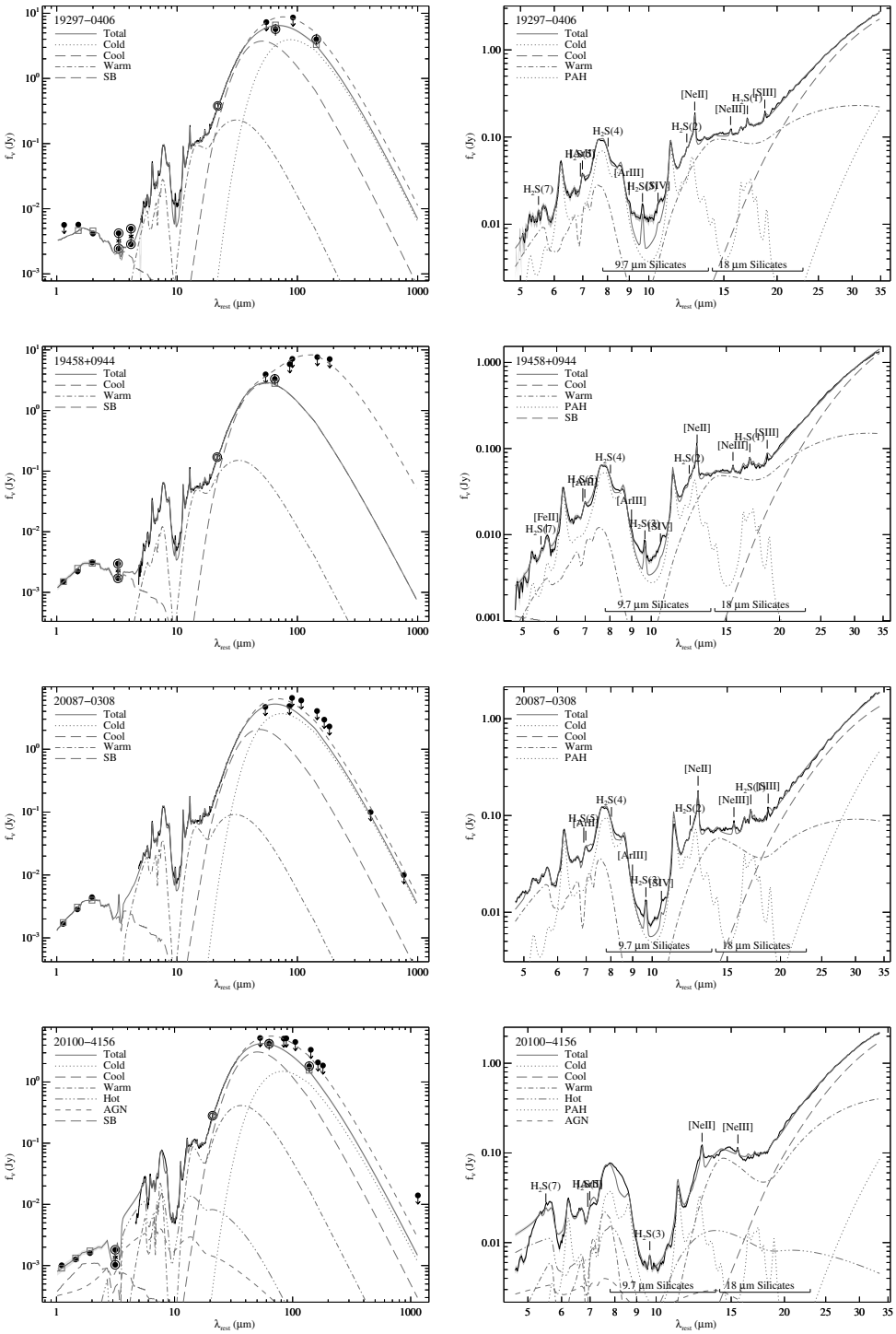

Figure E.2 (Continued)

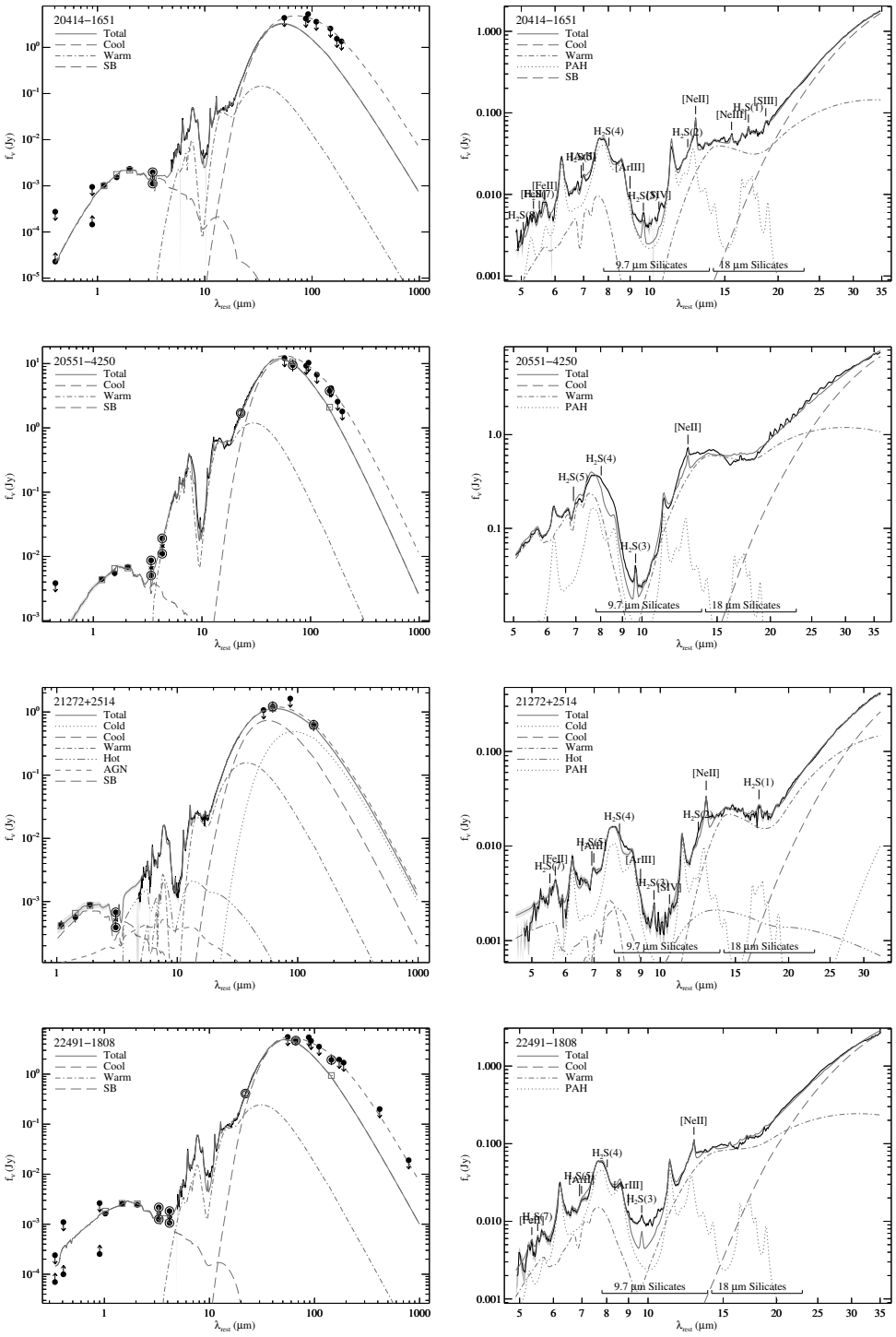

Figure E.2 (Continued)

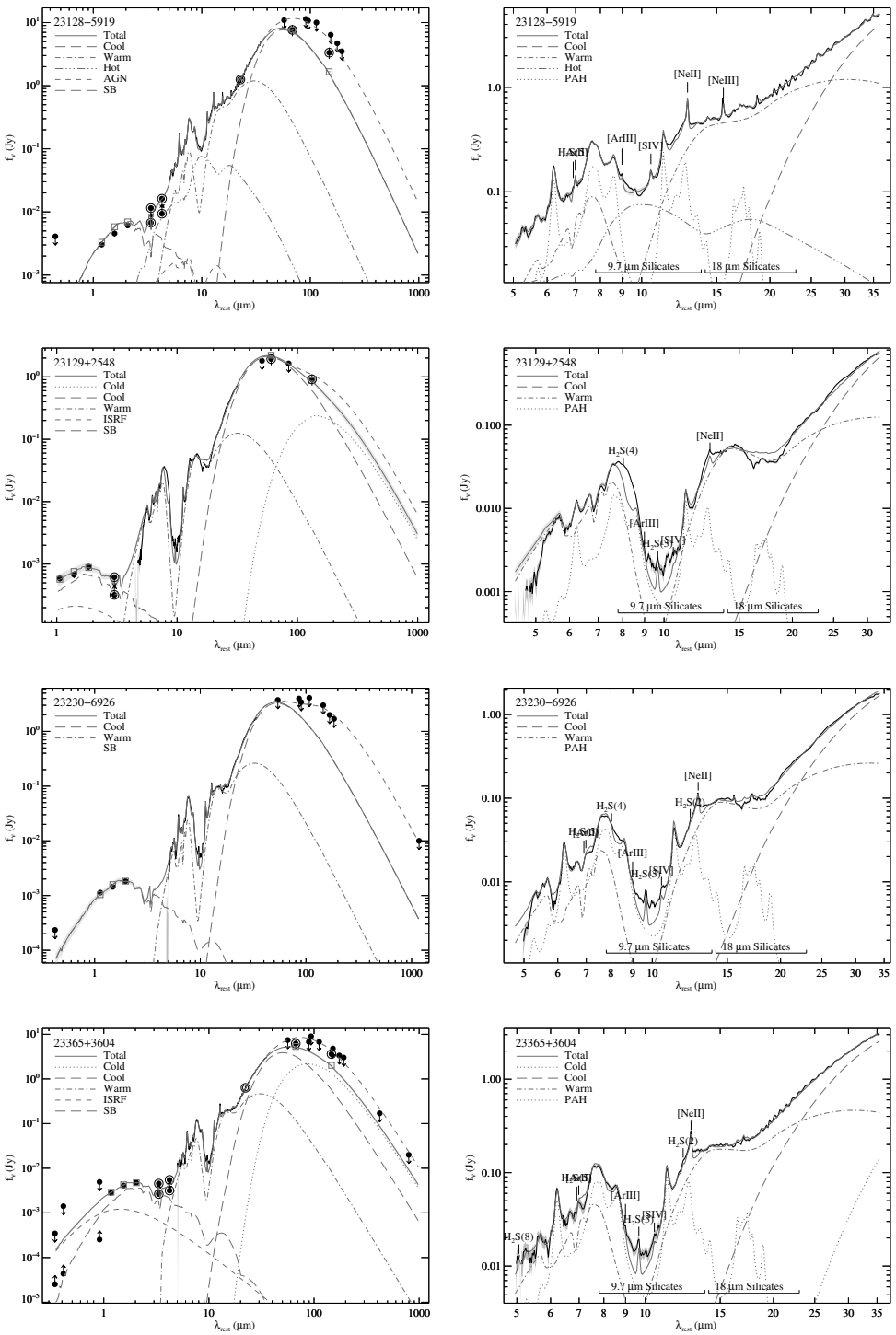

Figure E.2 (Continued)

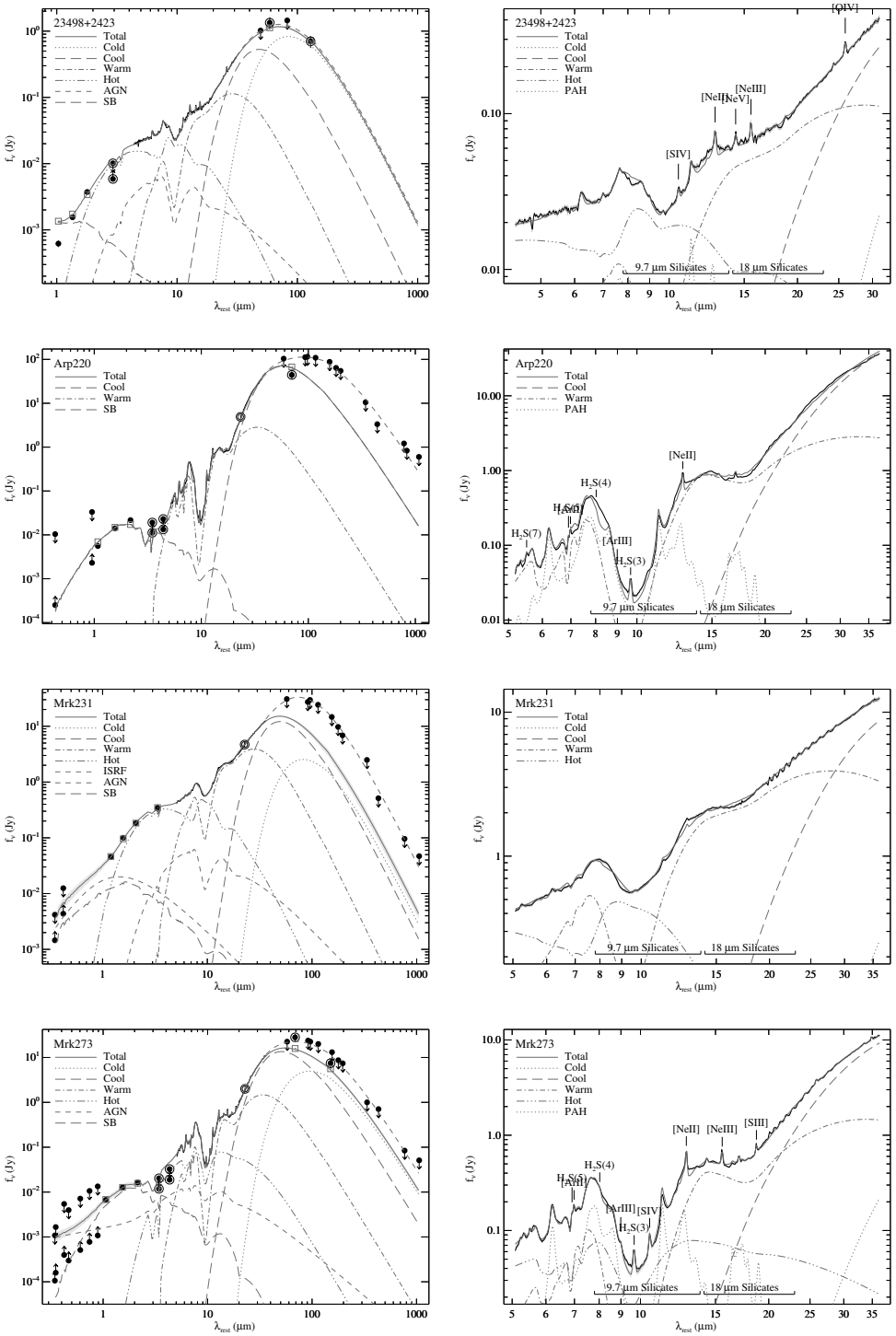

Figure E.2 (Continued)

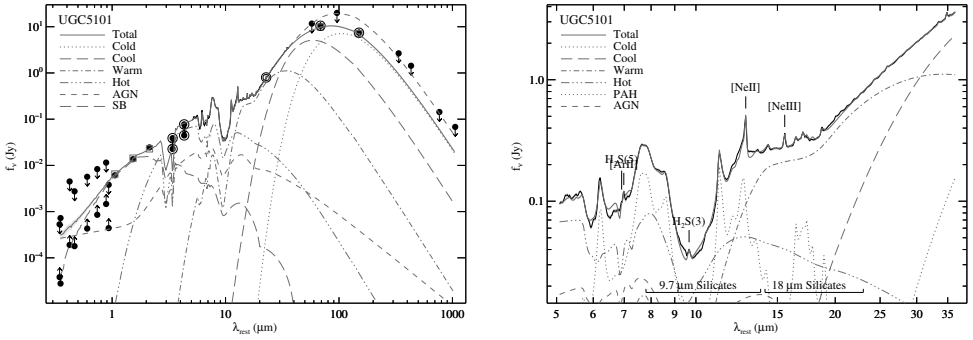

Appendix F

Starburst Imaging

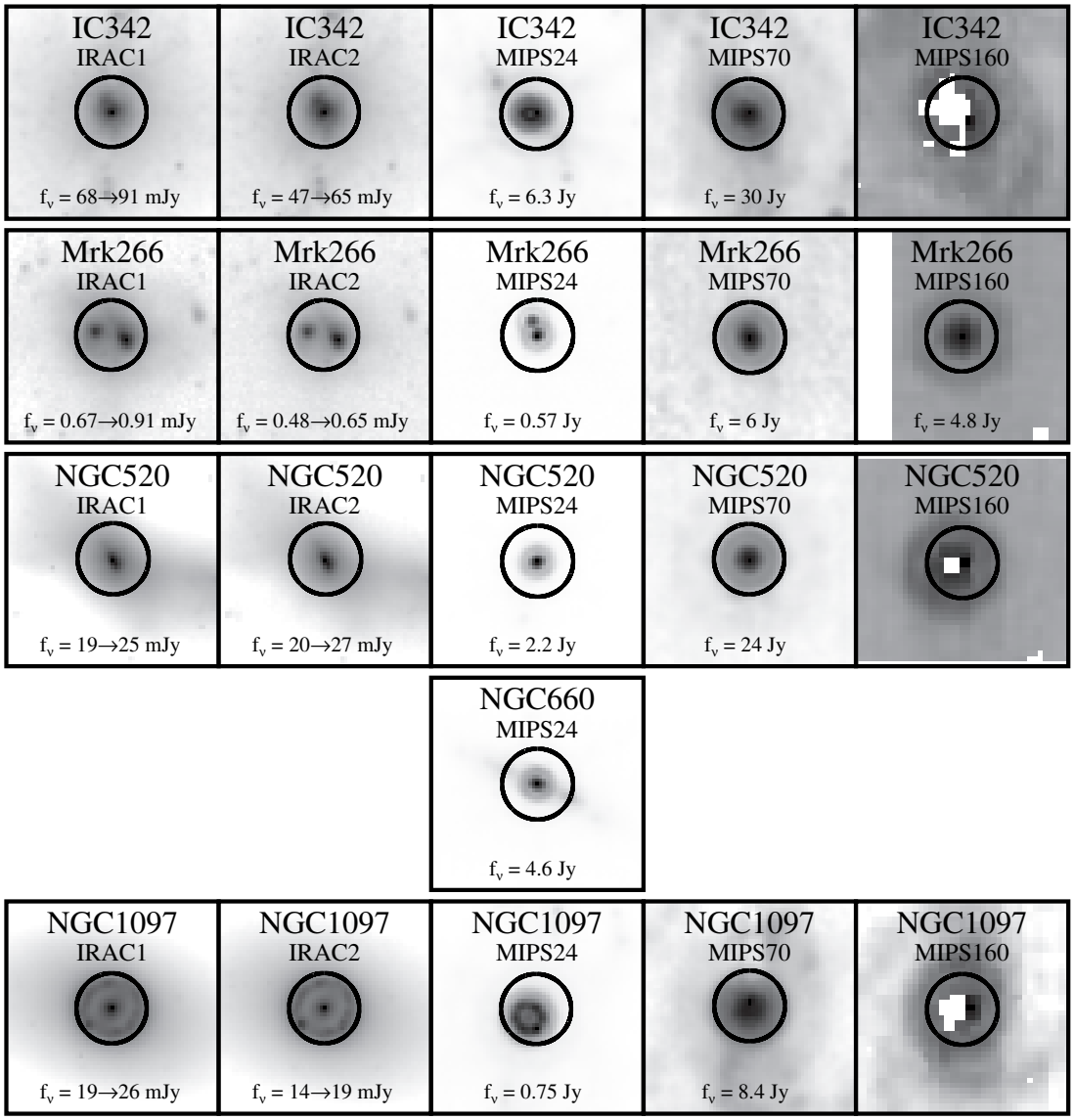

Figure F.1 IRAC and MIPS images and derived aperture photometry for the Starburst galaxies in our sample. Observed and aperture-corrected flux densities are given for the IRAC data.

Figure F.2 (Continued)

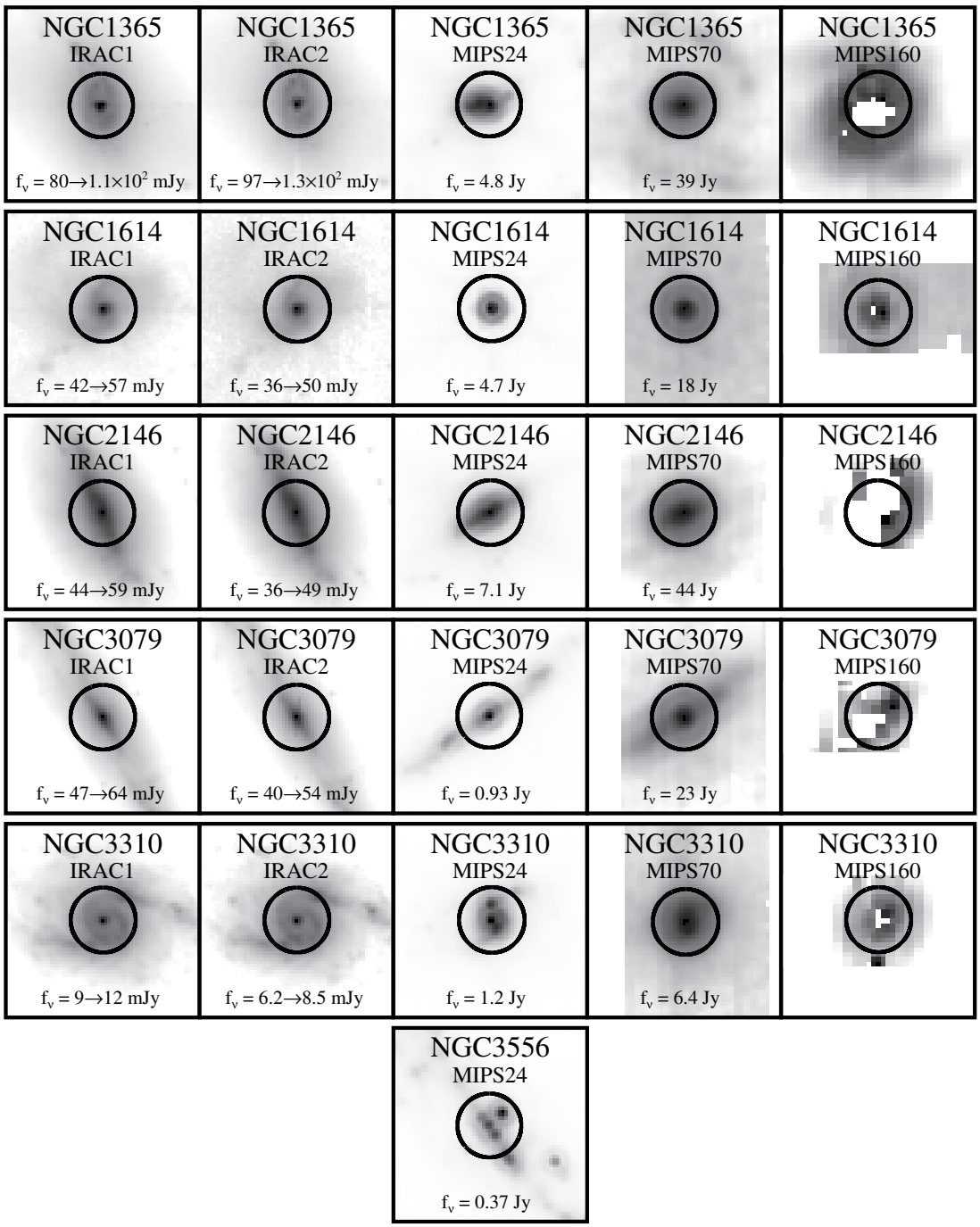

Figure F.2 (Continued)

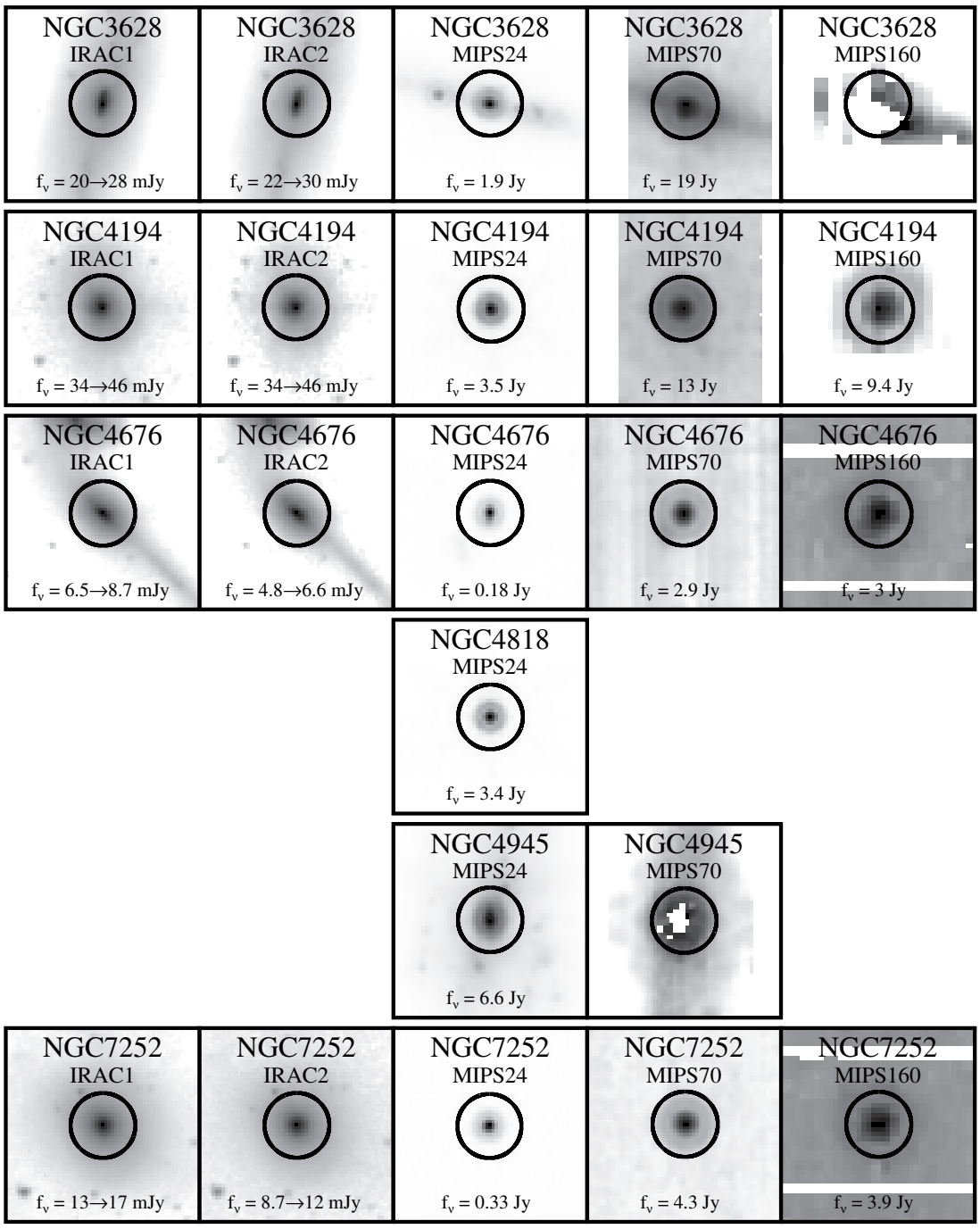

Figure F.2 (Continued)

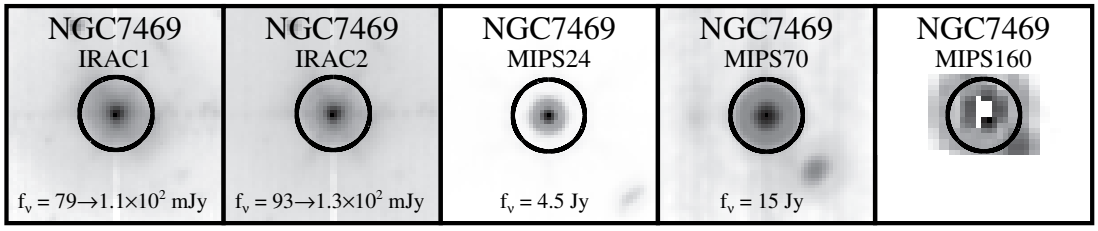

Appendix G

AGN Imaging

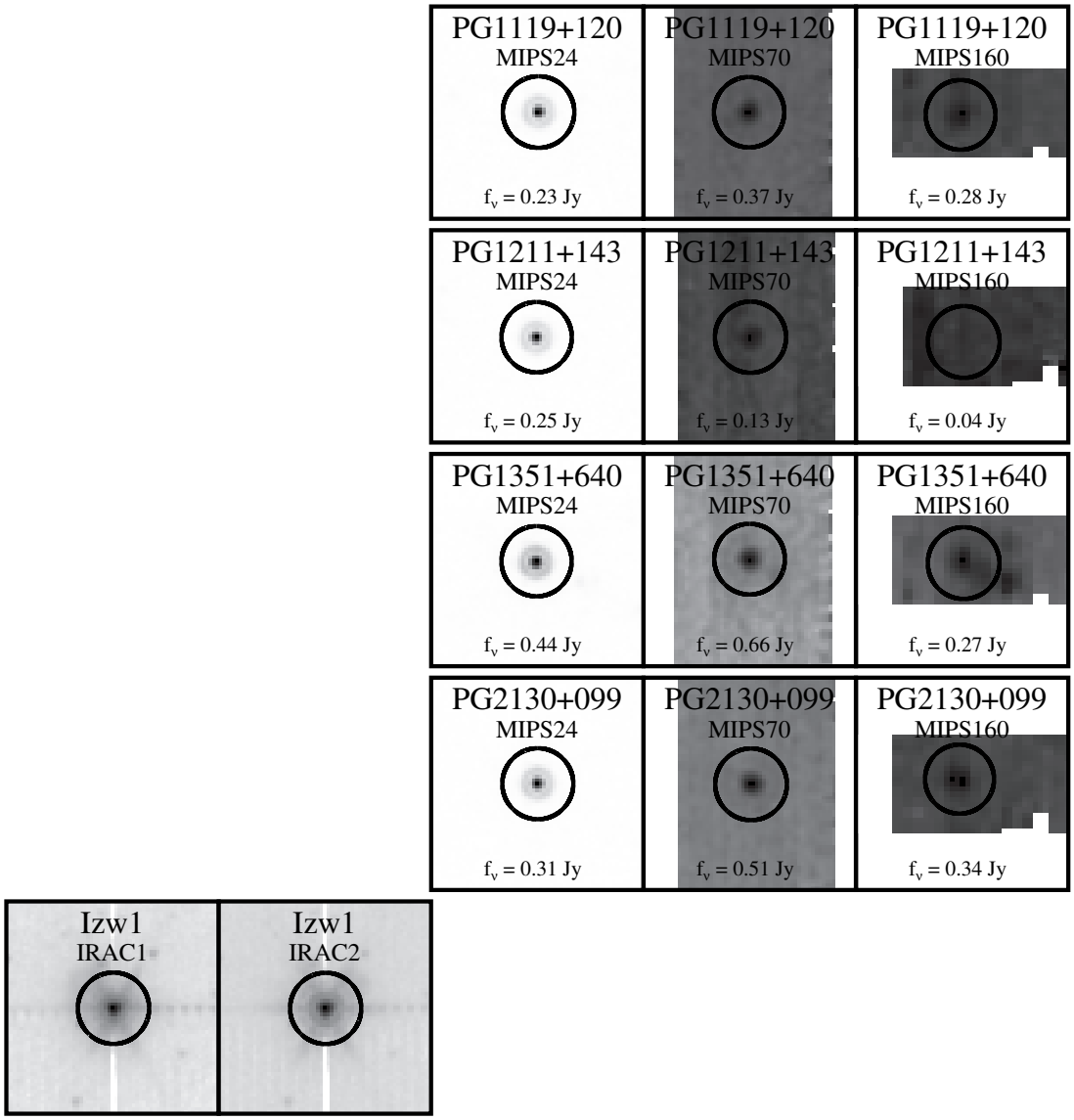

Figure G.1 IRAC and MIPS images and derived aperture photometry for the AGNs in our sample. Observed and aperture-corrected flux densities are given for the IRAC data.

Appendix H

ULIRG Imaging

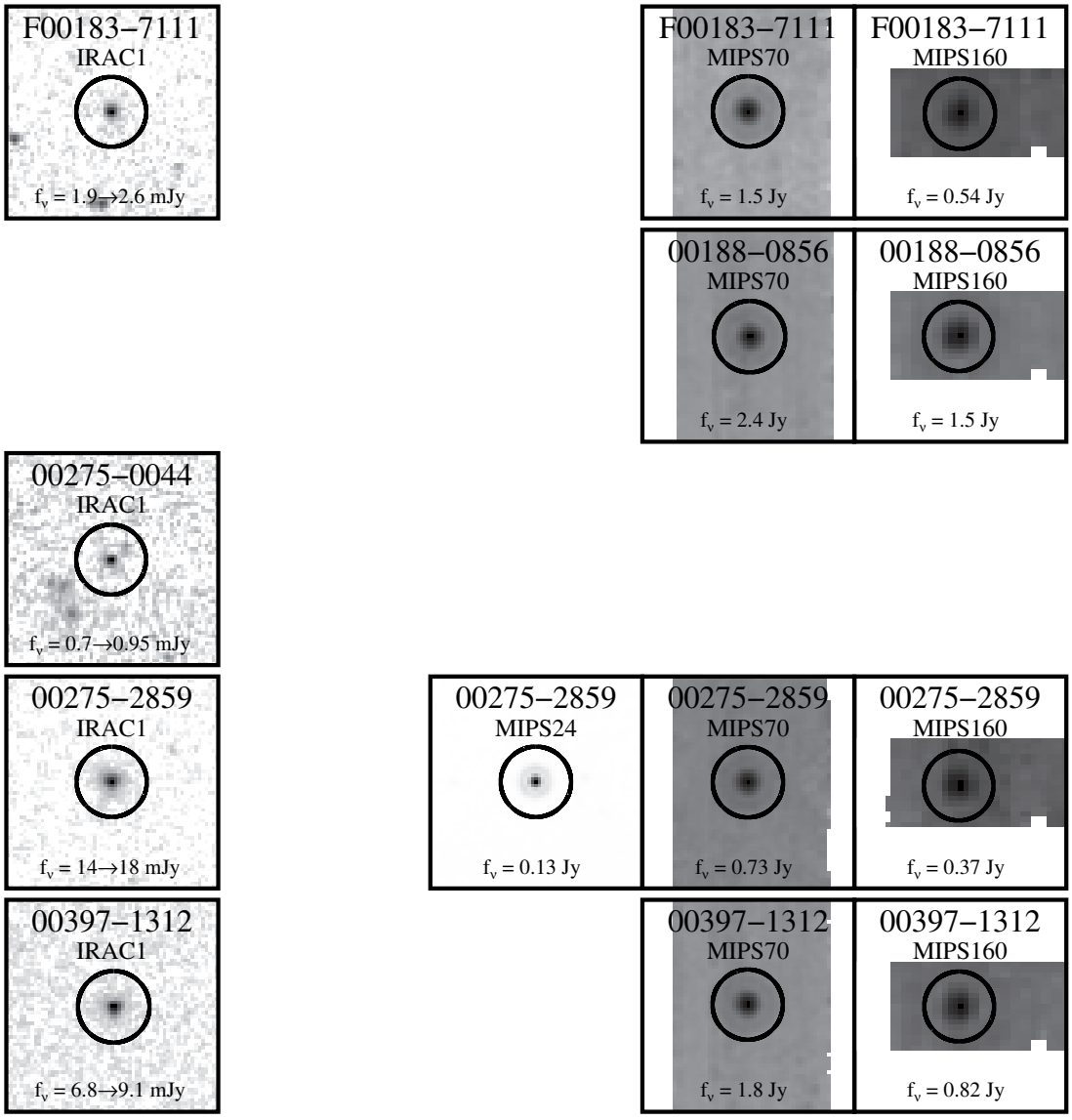

Figure H.1 IRAC and MIPS images and derived aperture photometry for the ULIRGs in our sample. Observed and aperture-corrected flux densities are given for the IRAC data.

Figure H.2 (Continued)

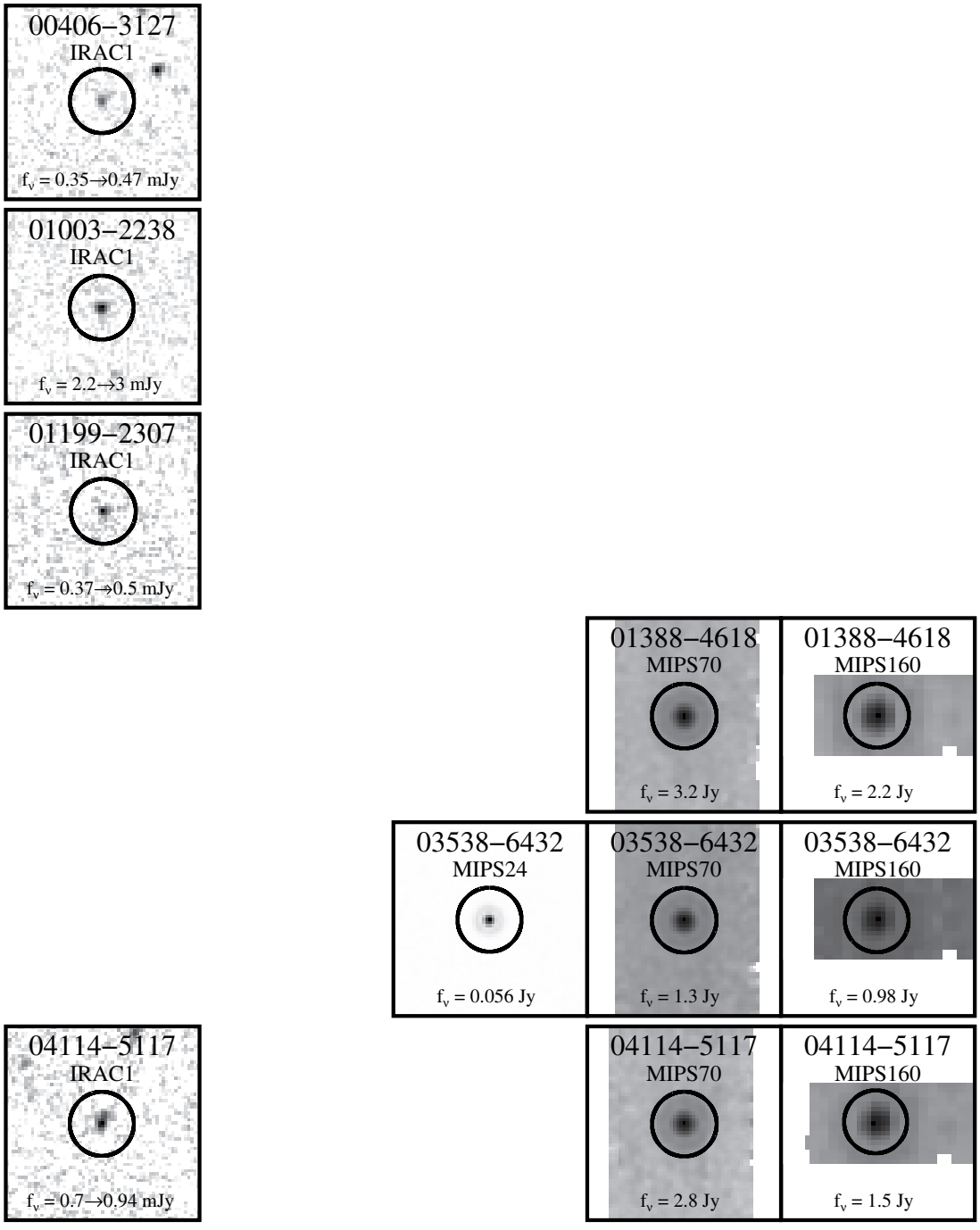

Figure H.2 (Continued)

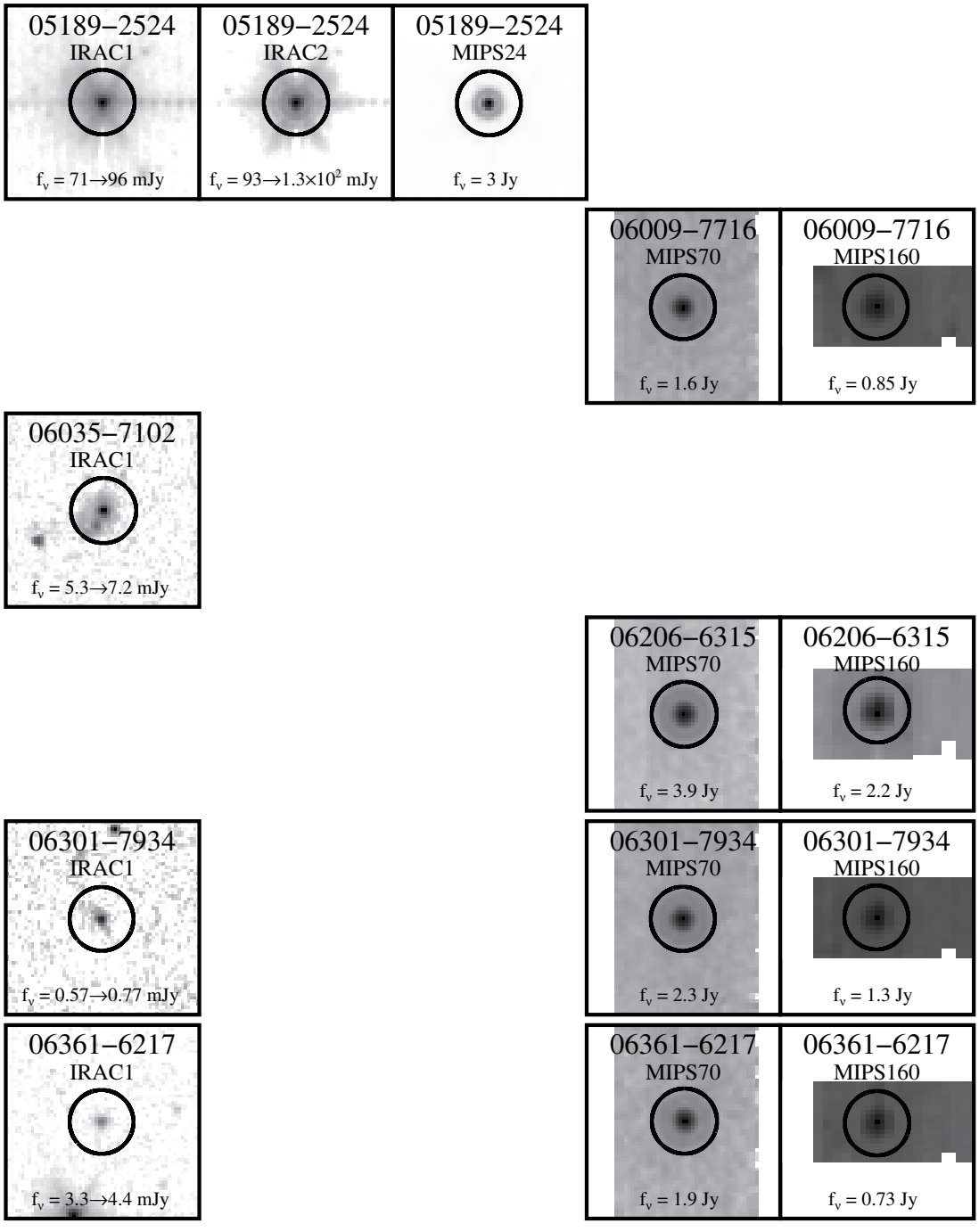

Figure H.2 (Continued)

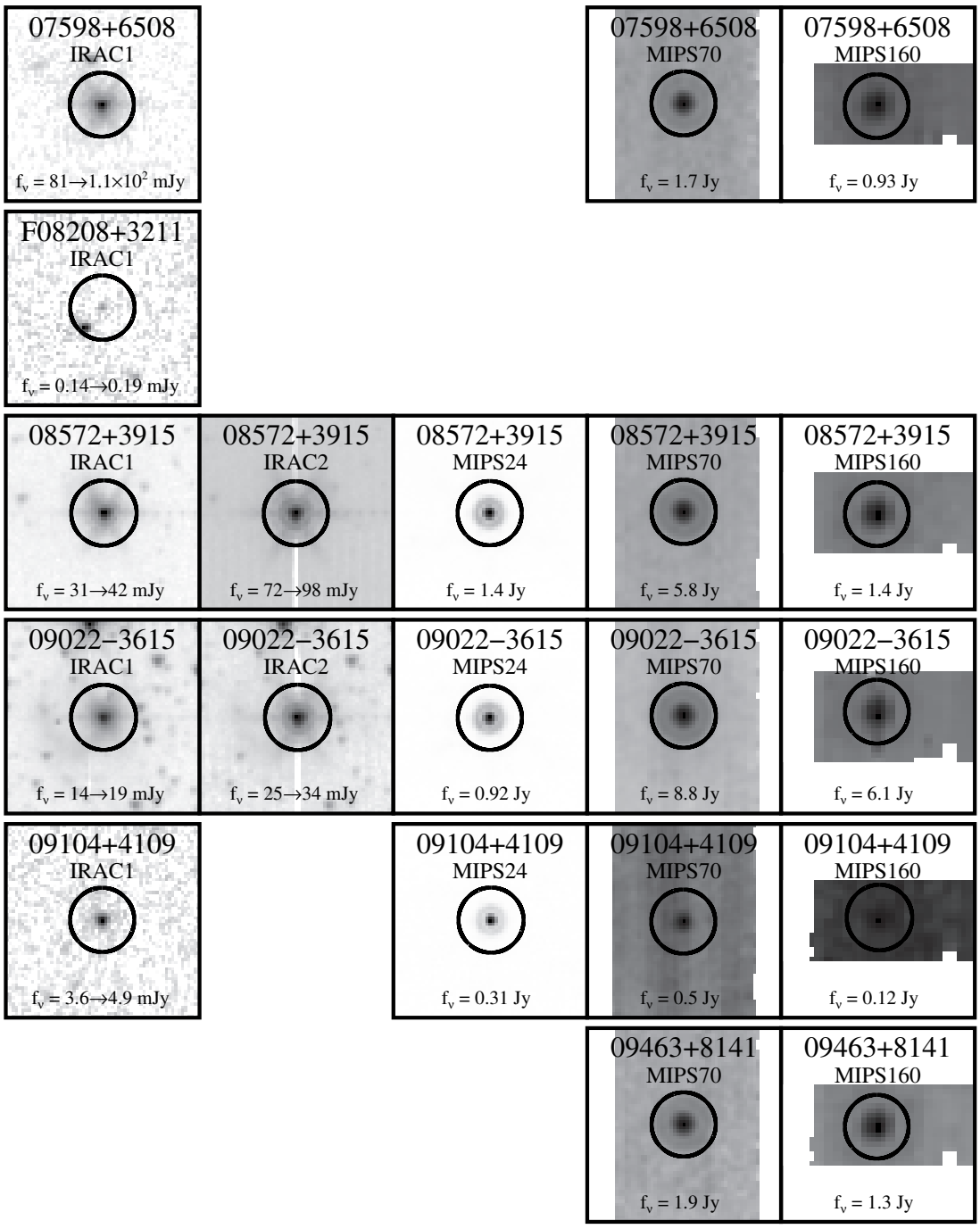

Figure H.2 (Continued)

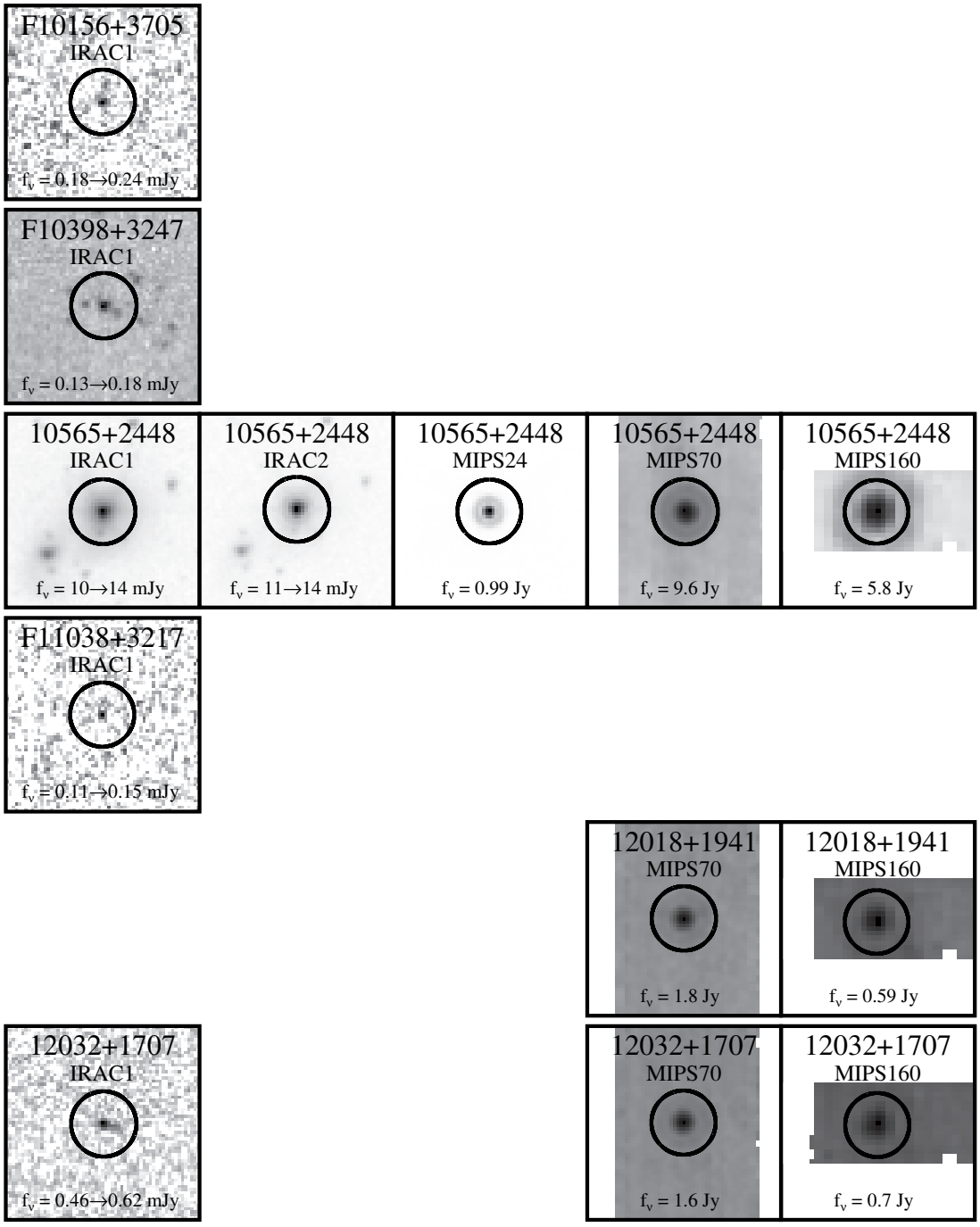

Figure H.2 (Continued)

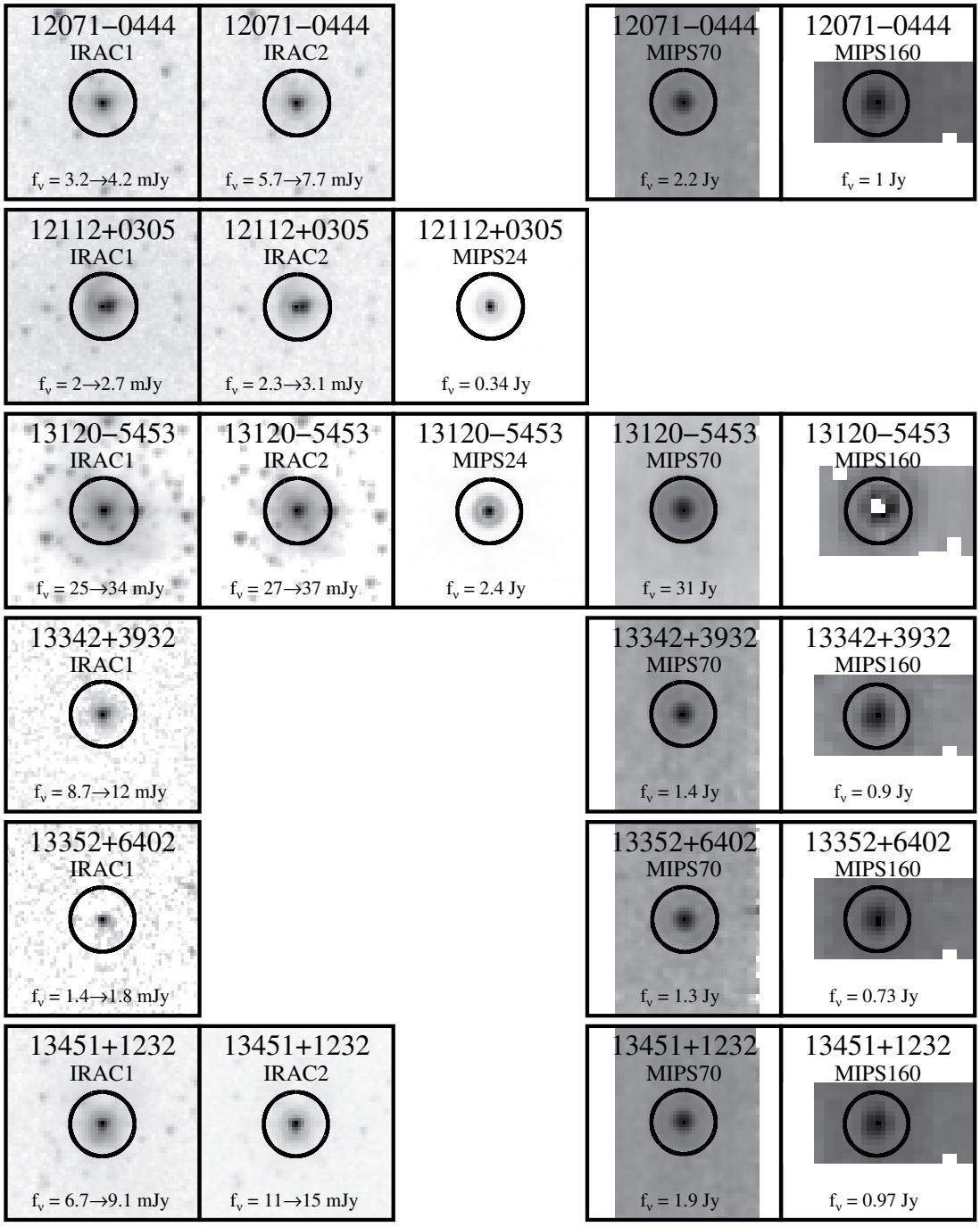

Figure H.2 (Continued)

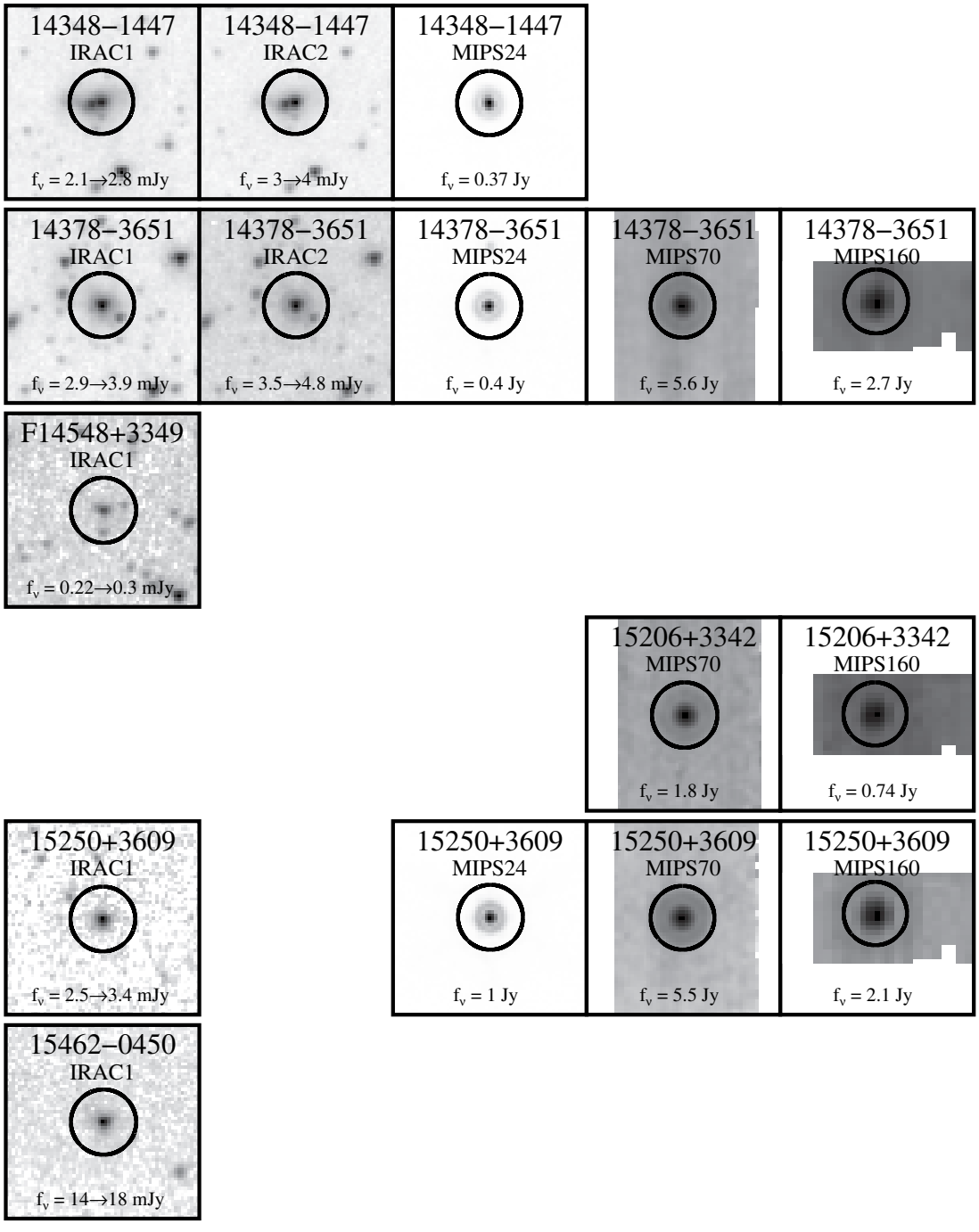

Figure H.2 (Continued)

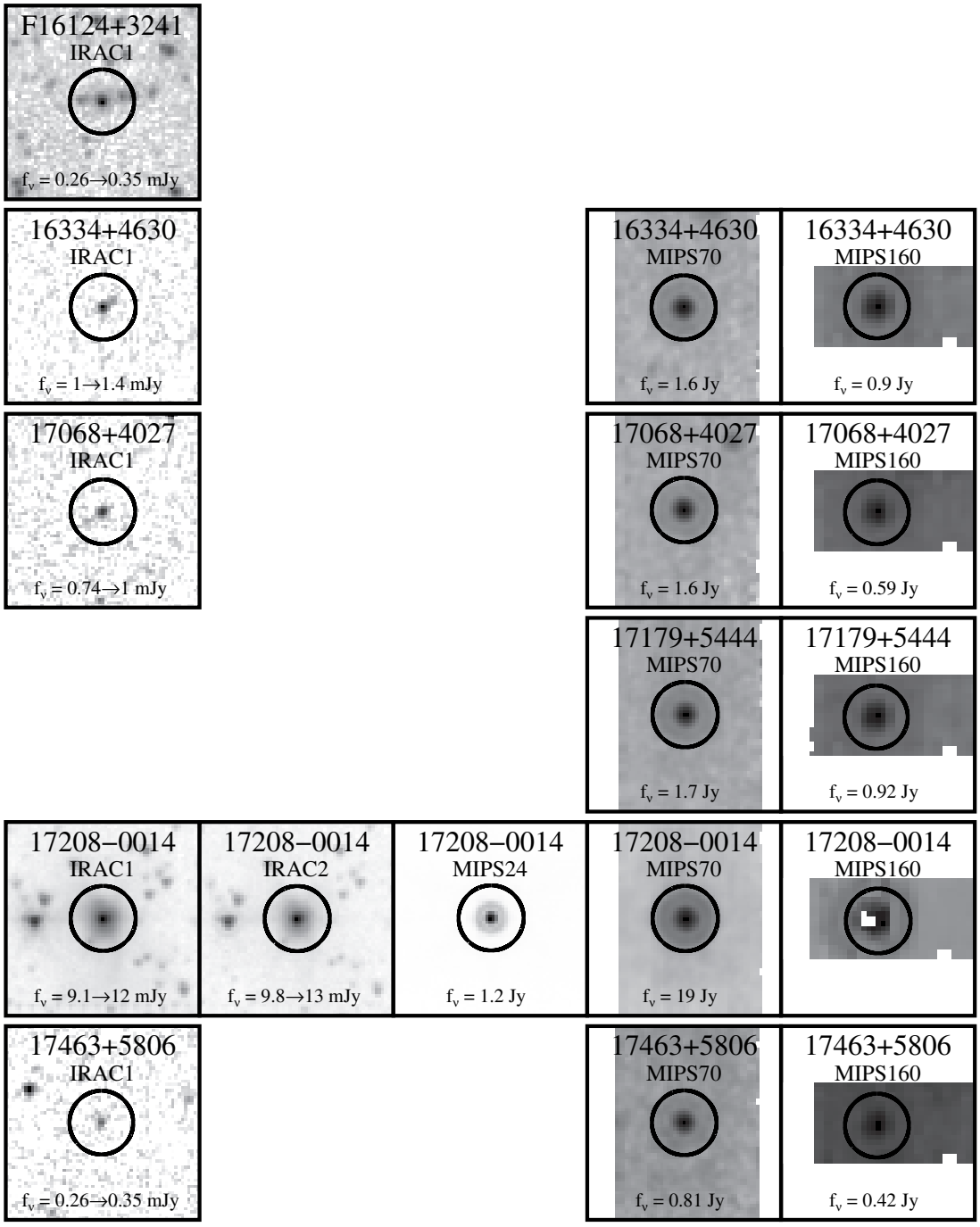

Figure H.2 (Continued)

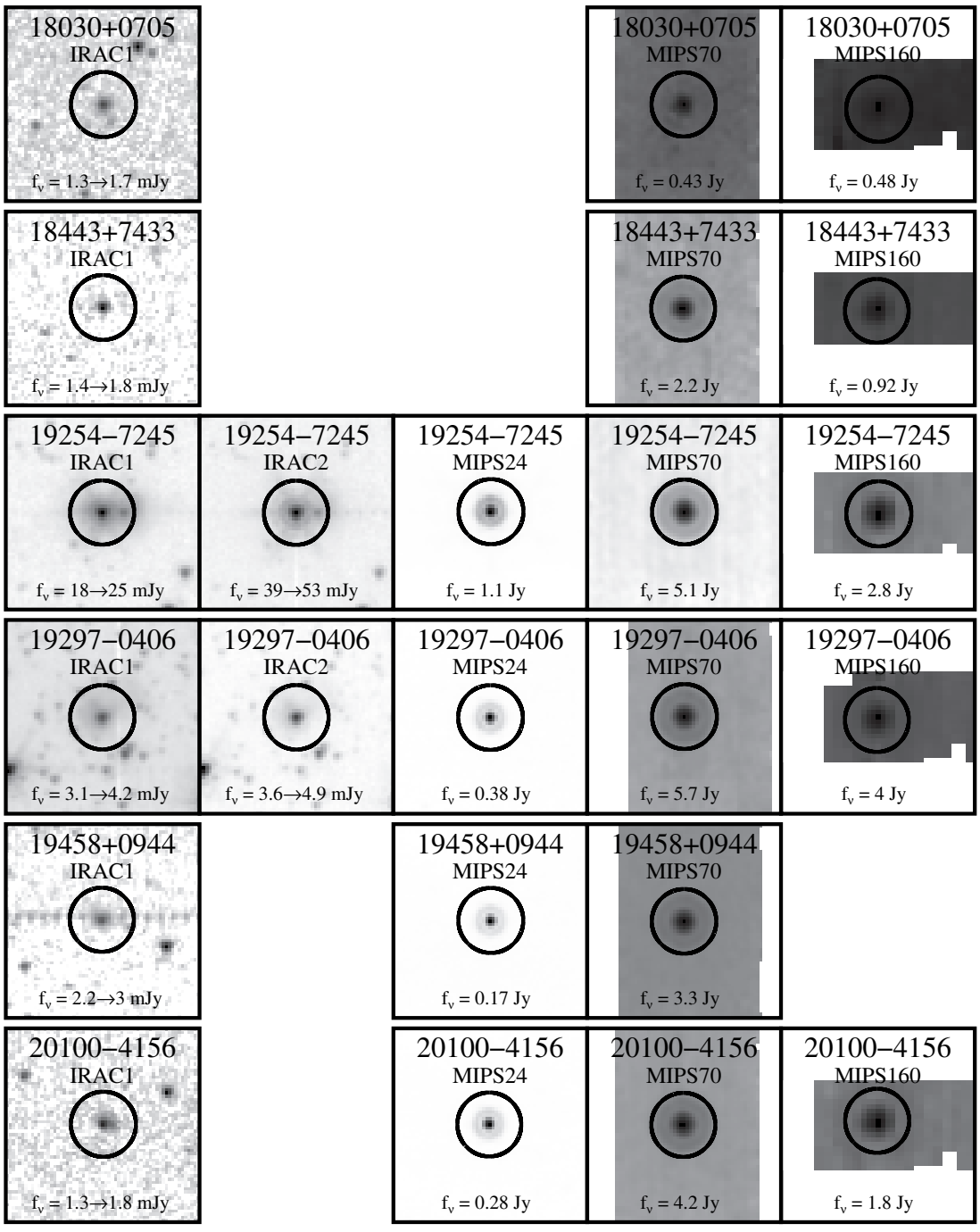

Figure H.2 (Continued)

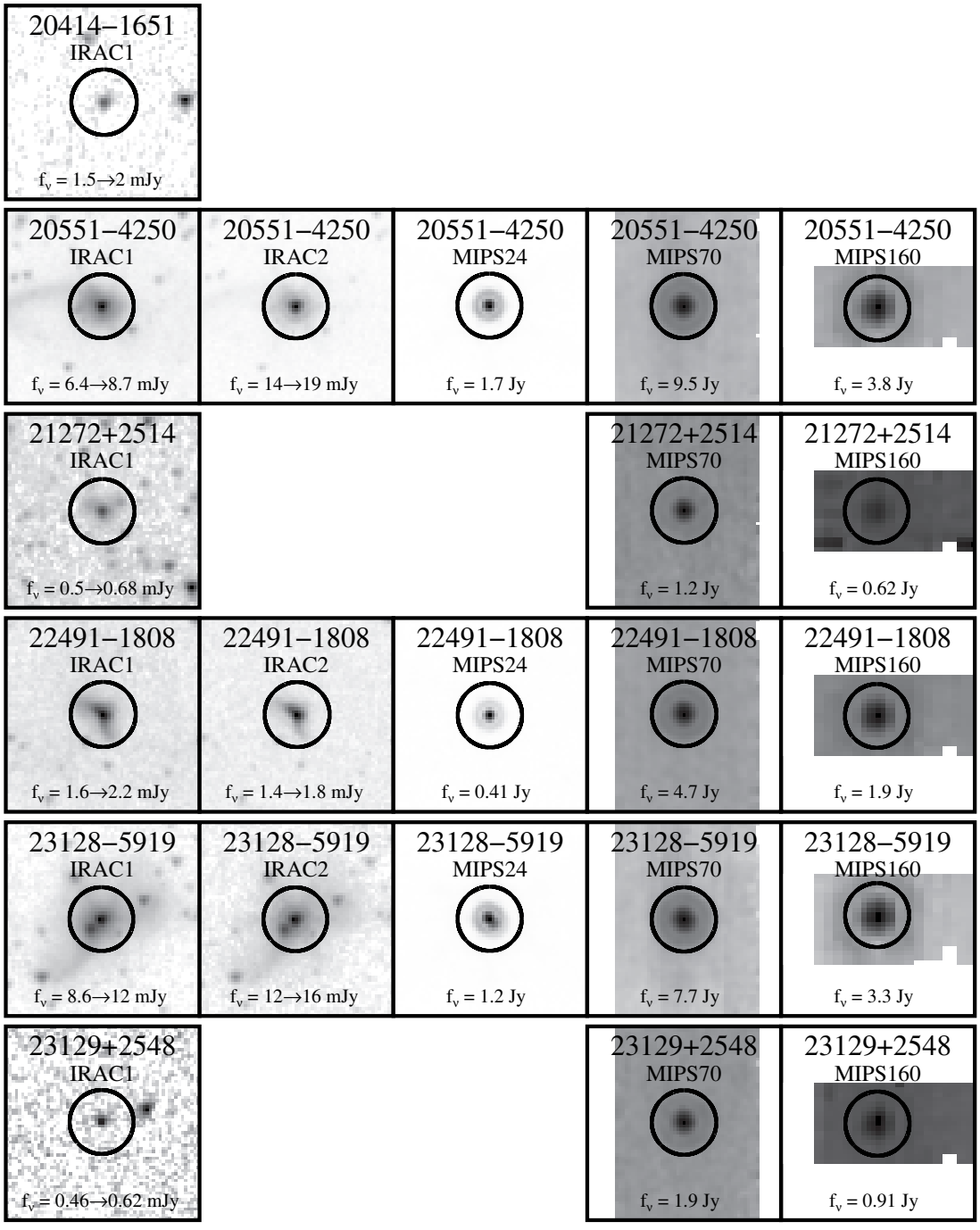

Figure H.2 (Continued)

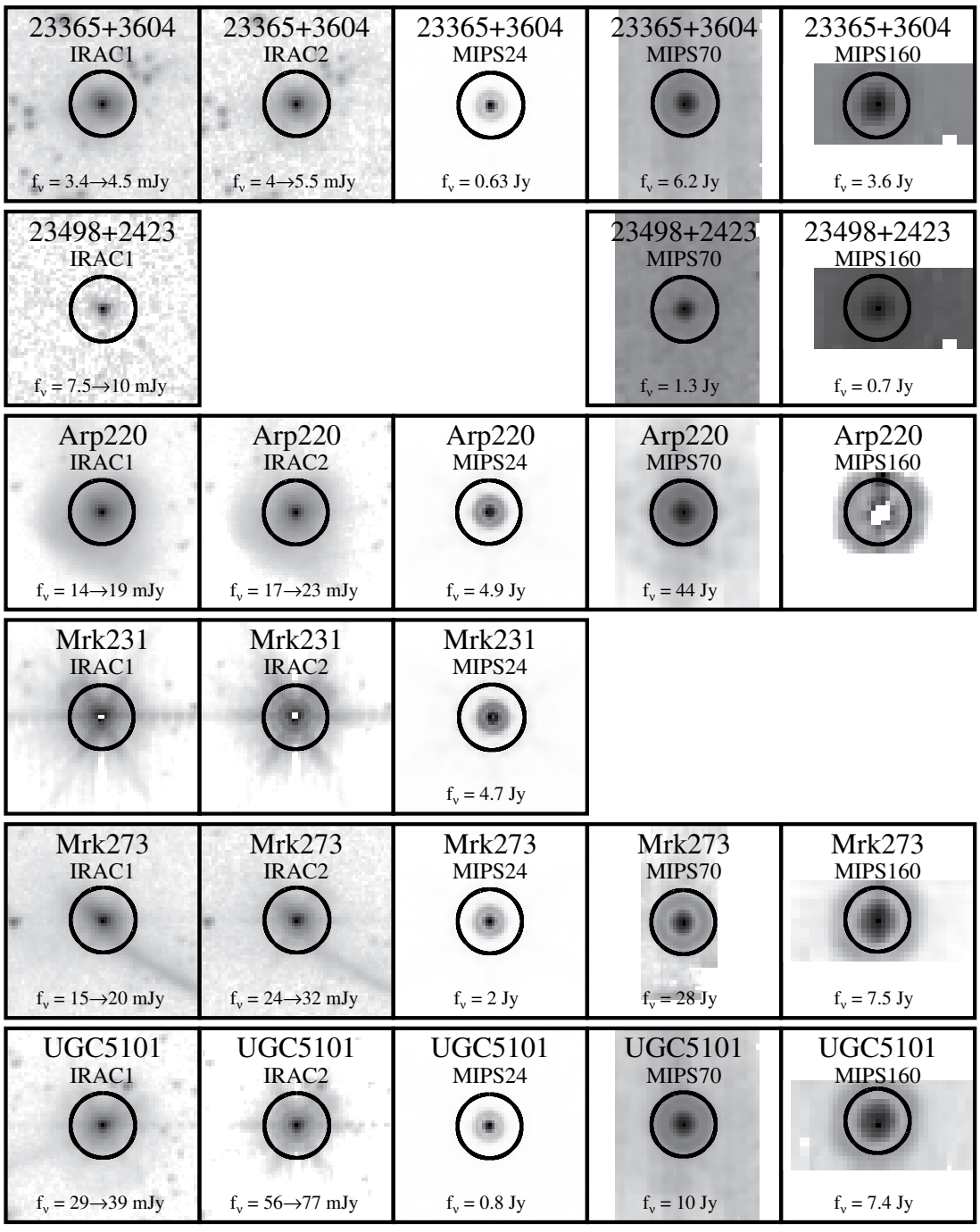

BIBLIOGRAPHY

Allamandola, L. J., Sandford, S. A., & Wopenka, B. 1987, Science, 237, 56

Allamandola, L. J., Tielens, A. G. G. M., & Barker, J. R. 1985, ApJ, 290, L25

Antonucci, R. 1993, ARA&A, 31, 473

Armus, L., Bernard-Salas, J., Spoon, H. W. W., Marshall, J. A., Charmandaris, V., Higdon, S. J. U., Desai, V., Hao, L., Teplitz, H. I., Devost, D., Brandl, B. R., Soifer, B. T., & Houck, J. R. 2006, ApJ, 640, 204

Armus, L., Charmandaris, V., Bernard-Salas, J., Spoon, H. W. W., Marshall, J. A., Higdon, S. J. U., Desai, V., Teplitz, H. I., Hao, L., Devost, D., Brandl, B. R., Wu, Y., Sloan, G. C., Soifer, B. T., Houck, J. R., & Herter, T. L. 2007, ApJ, 656, 148

Armus, L., Charmandaris, V., Spoon, H. W. W., Houck, J. R., Soifer, B. T., Brandl, B. R., Appleton, P. N., Teplitz, H. I., Higdon, S. J. U., Weedman, D. W., Devost, D., Morris, P. W., Uchida, K. I., van Cleve, J., Barry, D. J., Sloan, G. C., Grillmair, C. J., Burgdorf, M. J., Fajardo-Acosta, S. B., Ingalls, J. G., Higdon, J., Hao, L., Bernard-Salas, J., Herter, T., Troeltzsch, J., Unruh, B., & Winghart, M. 2004, ApJS, 154, 178

Armus, L., Heckman, T., & Miley, G. 1987, AJ, 94, 831

Armus, L., Heckman, T. M., & Miley, G. K. 1989, ApJ, 347, 727

Baskin, A. & Laor, A. 2005, MNRAS, 356, 1029

Benford, D. J. 1999, PhD thesis, AA(CALIFORNIA INSTITUTE OF TECHNOLOGY)

Blain, A. W., Smail, I., Ivison, R. J., Kneib, J.-P., & Frayer, D. T. 2002, Phys. Rep., 369, 111

Boller, T., Gallo, L. C., Lutz, D., & Sturm, E. 2002, MNRAS, 336, 1143

Brandl, B. R., Bernard-Salas, J., Spoon, H. W. W., Devost, D., Sloan, G. C., Guilles, S., Wu, Y., Houck, J. R., Weedman, D. W., Armus, L., Appleton, P. N., Soifer, B. T., Charmandaris, V., Hao, L., Higdon, J. A. M. S. J., & Herter, T. L. 2006, ApJ, 653, 1129

Brandl, B. R., Devost, D., Higdon, S. J. U., Charmandaris, V., Weedman, D., Spoon, H. W. W., Herter, T. L., Hao, L., Bernard-Salas, J., Houck, J. R., Armus, L., Soifer, B. T., Grillmair, C. J., & Appleton, P. N. 2004, ApJS, 154, 188

Calzetti, D., Kennicutt, Jr., R. C., Bianchi, L., Thilker, D. A., Dale, D. A., Engelbracht, C. W., Leitherer, C., Meyer, M. J., Sosey, M. L., Mutchler, M., Regan, M. W., Thornley, M. D., Armus, L., Bendo, G. J., Boissier, S., Boselli, A., Draine, B. T., Gordon, K. D., Helou, G., Hollenbach, D. J., Kewley, L., Madore, B. F., Martin, D. C., Murphy, E. J., Rieke, G. H., Rieke, M. J., Roussel, H., Sheth, K., Smith, J. D., Walter, F., White, B. A., Yi, S., Scoville, N. Z., Polletta, M., & Lindler, D. 2005, ApJ, 633, 871

Chiar, J. E., Tielens, A. G. G. M., Whittet, D. C. B., Schutte, W. A., Boogert, A. C. A., Lutz, D., van Dishoeck, E. F., & Bernstein, M. P. 2000, ApJ, 537, 749

Condon, J. J., Huang, Z.-P., Yin, Q. F., & Thuan, T. X. 1991, ApJ, 378, 65

Dale, D. A., Helou, G., Contursi, A., Silbermann, N. A., & Kolhatkar, S. 2001, ApJ, 549, 215

de Vaucouleurs, G., de Vaucouleurs, A., Corwin, Jr., H. G., Buta, R. J., Paturel, G., & Fouque, P. 1991, Third Reference Catalogue of Bright Galaxies (Volume 1-3, XII, 2069 pp. 7 figs.. Springer-Verlag Berlin Heidelberg New York)

Desert, F.-X., Boulanger, F., & Puget, J. L. 1990, A&A, 237, 215

Draine, B. T. 1995, Ap&SS, 233, 111

—. 2003, ARA&A, 41, 241

Draine, B. T. & Anderson, N. 1985, ApJ, 292, 494

Draine, B. T., Dale, D. A., Bendo, G., Gordon, K. D., Smith, J. D. T., Armus, L., Engelbracht, C. W., Helou, G., Kennicutt, R. C., Li, A., Roussel, H., Walter, F., Calzetti, D., Moustakas, J., Murphy, E. J., Rieke, G. H., Bot, C., Hollenbach, D. J., Sheth, K., & Teplitz, H. I. 2007, ApJ, in press (astro-ph/0703213)

Draine, B. T. & Lee, H. M. 1984, ApJ, 285, 89

Draine, B. T. & Li, A. 2001, ApJ, 551, 807

Draine, B. T. & Salpeter, E. E. 1979, ApJ, 231, 77

Dullemond, C. P. & van Bemmel, I. M. 2005, A&A, 436, 47

Dunne, L., Eales, S., Edmunds, M., Ivison, R., Alexander, P., & Clements, D. L. 2000, MNRAS, 315, 115

Elbaz, D. & Cesarsky, C. J. 2003, Science, 300, 270

Engelbracht, C. W., Gordon, K. D., Rieke, G. H., Werner, M. W., Dale, D. A., & Latter, W. B. 2005, ApJ, 628, L29

Farrah, D., Afonso, J., Efstathiou, A., Rowan-Robinson, M., Fox, M., & Clements, D. 2003, MNRAS, 343, 585

Förster Schreiber, N. M., Roussel, H., Sauvage, M., & Charmandaris, V. 2004, A&A, 419, 501

Furton, D. G., Laiho, J. W., & Witt, A. N. 1999, ApJ, 526, 752

Genzel, R., Lutz, D., Sturm, E., Egami, E., Kunze, D., Moorwood, A. F. M., Rigopoulou, D., Spoon, H. W. W., Sternberg, A., Tacconi-Garman, L. E., Tacconi, L., & Thatte, N. 1998, ApJ, 498, 579

Gibb, E. L., Whittet, D. C. B., Schutte, W. A., Boogert, A. C. A., Chiar, J. E., Ehrenfreund, P., Gerakines, P. A., Keane, J. V., Tielens, A. G. G. M., van Dishoeck, E. F., & Kerkhof, O. 2000, ApJ, 536, 347

Girardi, L., Bressan, A., Bertelli, G., & Chiosi, C. 2000, A&AS, 141, 371

Goodrich, R. W., Veilleux, S., & Hill, G. J. 1994, ApJ, 422, 521

Granato, G. L. & Danese, L. 1994, MNRAS, 268, 235

Greenberg, J. M. & Hong, S.-S. 1974, in IAU Symp. 60: Galactic Radio Astronomy, ed. F. J. Kerr & S. C. Simonson, 155–177

Guhathakurta, P. & Draine, B. T. 1989, ApJ, 345, 230

Haas, M., Klaas, U., Müller, S. A. H., Bertoldi, F., Camenzind, M., Chini, R., Krause, O., Lemke, D., Meisenheimer, K., Richards, P. J., & Wilkes, B. J. 2003, A&A, 402, 87

Hao, L., Spoon, H. W. W., Sloan, G. C., Marshall, J. A., Armus, L., Tielens, A. G. G. M., Sargent, B., van Bemmel, I. M., Charmandaris, V., Weedman, D. W., & Houck, J. R. 2005a, ApJ, 625, L75

Hao, L., Strauss, M. A., Fan, X., Tremonti, C. A., Schlegel, D. J., Heckman, T. M., Kauffmann, G., Blanton, M. R., Gunn, J. E., Hall, P. B., Ivezić, Ž., Knapp, G. R., Krolik, J. H., Lupton, R. H., Richards, G. T., Schneider, D. P., Strateva, I. V., Zakamska, N. L., Brinkmann, J., & Szokoly, G. P. 2005b, AJ, 129, 1795

Helou, G. 1986, ApJ, 311, L33

Higdon, S. J. U., Devost, D., Higdon, J. L., Brandl, B. R., Houck, J. R., Hall, P., Barry, D., Charmandaris, V., Smith, J. D. T., Sloan, G. C., & Green, J. 2004, PASP, 116, 975

Hollenbach, D. J. & Tielens, A. G. G. M. 1997, ARA&A, 35, 179

Houck, J. R., Roellig, T. L., van Cleve, J., Forrest, W. J., Herter, T., Lawrence, C. R., Matthews, K., Reitsema, H. J., Soifer, B. T., Watson, D. M., Weedman, D., Huisjen, M., Troeltzsch, J., Barry, D. J., Bernard-Salas, J., Blacken, C. E., Brandl, B. R., Charmandaris, V., Devost, D., Gull, G. E., Hall, P., Henderson, C. P., Higdon, S. J. U., Pirger, B. E., Schoenwald, J., Sloan, G. C., Uchida, K. I., Appleton, P. N., Armus, L., Burgdorf, M. J., Fajardo-Acosta, S. B., Grillmair, C. J., Ingalls, J. G., Morris, P. W., & Teplitz, H. I. 2004, ApJS, 154, 18

Houck, J. R., Soifer, B. T., Neugebauer, G., Beichman, C. A., Aumann, H. H., Clegg, P. E., Gillett, F. C., Habing, H. J., Hauser, M. G., Low, F. J., Miley, G., Rowan-Robinson, M., & Walker, R. G. 1984, ApJ, 278, L63

Houck, J. R., Soifer, B. T., Weedman, D., Higdon, S. J. U., Higdon, J. L., Herter, T., Brown, M. J. I., Dey, A., Jannuzi, B. T., Le Floc'h, E., Rieke, M., Armus, L., Charmandaris, V., Brandl, B. R., & Teplitz, H. I. 2005, ApJ, 622, L105

Imanishi, M., Dudley, C. C., & Maloney, P. R. 2006, ApJ, 637, 114

Jaffe, W., Meisenheimer, K., Röttgering, H. J. A., Leinert, C., Richichi, A., Chesneau, O., Fraix-Burnet, D., Glazenborg-Kluttig, A., Granato, G.-L., Graser, U., Heijligers, B., Köhler, R., Malbet, F., Miley, G. K., Paresce, F., Pel, J.-W., Perrin, G., Przygodda, F., Schoeller, M., Sol, H., Waters, L. B. F. M., Weigelt, G., Woillez, J., & de Zeeuw, P. T. 2004, Nature, 429, 47

Jones, A. P., Tielens, A. G. G. M., Hollenbach, D. J., & McKee, C. F. 1994, ApJ, 433, 797

Kessler, M. F. 1999, in ESA Special Publication, Vol. 427, The Universe as Seen by ISO, ed. P. Cox & M. Kessler, 23

Kim, D.-C., Sanders, D. B., Veilleux, S., Mazzarella, J. M., & Soifer, B. T. 1995, ApJS, 98, 129

Kim, S.-H., Martin, P. G., & Hendry, P. D. 1994, ApJ, 422, 164

Kinney, A. L., Bohlin, R. C., Calzetti, D., Panagia, N., & Wyse, R. F. G. 1993, ApJS, 86, 5

Klaas, U., Haas, M., Müller, S. A. H., Chini, R., Schulz, B., Coulson, I., Hippelein, H., Wilke, K., Albrecht, M., & Lemke, D. 2001, A&A, 379, 823

Kleinmann, D. E. & Low, F. J. 1970a, ApJ, 161, L203+

—. 1970b, ApJ, 159, L165+

Komossa, S., Burwitz, V., Hasinger, G., Predehl, P., Kaastra, J. S., & Ikebe, Y. 2003, ApJ, 582, L15

Kroupa, P. 2001, MNRAS, 322, 231

Krugel, E. & Siebenmorgen, R. 1994, A&A, 282, 407

Krugel, E., Siebenmorgen, R., Zota, V., & Chini, R. 1998, A&A, 331, L9

Lançon, A., Goldader, J. D., Leitherer, C., & Delgado, R. M. G. 2001, ApJ, 552, 150

Laor, A. & Draine, B. T. 1993, ApJ, 402, 441

Laurent, O., Mirabel, I. F., Charmandaris, V., Gallais, P., Madden, S. C., Sauvage, M., Vigroux, L., & Cesarsky, C. 2000, A&A, 359, 887

Leger, A. & Puget, J. L. 1984, A&A, 137, L5

Leitherer, C. 1990, ApJS, 73, 1

Levenson, N. A., Sirocky, M. M., Hao, L., Spoon, H. W. W., Marshall, J. A., Elitzur, M., & Houck, J. R. 2007, ApJ, 654, L45

Li, A. 2005, Penetrating Bars Through Masks of Cosmic Dust, Block et al. (eds.), Springer, 535 (astro-ph/0503571)

Li, A. & Draine, B. T. 2001, ApJ, 554, 778

—. 2002, ApJ, 576, 762

Lira, P., Ward, M. J., Zezas, A., & Murray, S. S. 2002, MNRAS, 333, 709

Low, J. & Kleinmann, D. E. 1968, AJ, 73, 868

Lutz, D., Kunze, D., Spoon, H. W. W., & Thornley, M. D. 1998, A&A, 333, L75

Lutz, D., Valiante, E., Sturm, E., Genzel, R., Tacconi, L. J., Lehnert, M. D., Sternberg, A., & Baker, A. J. 2005, ApJ, 625, L83

MacKenty, J. W. & Stockton, A. 1984, ApJ, 283, 64

Mathis, J. S., Mezger, P. G., & Panagia, N. 1983, A&A, 128, 212

Mazzarella, J. M., Soifer, B. T., Graham, J. R., Neugebauer, G., Matthews, K., & Gaume, R. A. 1991, AJ, 102, 1241

Mezger, P. G., Mathis, J. S., & Panagia, N. 1982, A&A, 105, 372

Mihos, J. C. & Hernquist, L. 1996, ApJ, 464, 641

Miller, J. S. & Goodrich, R. W. 1990, ApJ, 355, 456

Moshir, M. & et al. 1990, in IRAS Faint Source Catalogue, version 2.0 (1990), 0

Murphy, Jr., T. W., Armus, L., Matthews, K., Soifer, B. T., Mazzarella, J. M., Shupe, D. L., Strauss, M. A., & Neugebauer, G. 1996, AJ, 111, 1025

Nenkova, M., Ivezić, Ž., & Elitzur, M. 2002, ApJ, 570, L9

Neugebauer, G., Green, R. F., Matthews, K., Schmidt, M., Soifer, B. T., & Bennett, J. 1987, ApJS, 63, 615

Neugebauer, G., Habing, H. J., van Duinen, R., Aumann, H. H., Baud, B., Beichman, C. A., Beintema, D. A., Boggess, N., Clegg, P. E., de Jong, T., Emerson, J. P., Gautier, T. N., Gillett, F. C., Harris, S., Hauser, M. G., Houck, J. R., Jennings, R. E., Low, F. J., Marsden, P. L., Miley, G., Olnon, F. M., Pottasch, S. R., Raimond, E., Rowan-Robinson, M., Soifer, B. T., Walker, R. G., Wesselius, P. R., & Young, E. 1984, ApJ, 278, L1

Neugebauer, G. & Matthews, K. 1999, AJ, 118, 35

Peeters, E., Spoon, H. W. W., & Tielens, A. G. G. M. 2004, ApJ, 613, 986

Pier, E. A. & Krolik, J. H. 1992, ApJ, 401, 99

Purcell, E. M. 1976, ApJ, 206, 685

Puxley, P. J. & Brand, P. W. J. L. 1994, MNRAS, 266, 431

Risaliti, G., Gilli, R., Maiolino, R., & Salvati, M. 2000, A&A, 357, 13

Sanders, D. B., Mazzarella, J. M., Kim, D.-C., Surace, J. A., & Soifer, B. T. 2003, AJ, 126, 1607

Sanders, D. B. & Mirabel, I. F. 1996, ARA&A, 34, 749

Sanders, D. B., Phinney, E. S., Neugebauer, G., Soifer, B. T., & Matthews, K. 1989, ApJ, 347, 29

Sanders, D. B., Soifer, B. T., Elias, J. H., Madore, B. F., Matthews, K., Neugebauer, G., & Scoville, N. Z. 1988a, ApJ, 325, 74

Sanders, D. B., Soifer, B. T., Elias, J. H., Neugebauer, G., & Matthews, K. 1988b, ApJ, 328, L35

Schartmann, M., Meisenheimer, K., Camenzind, M., Wolf, S., & Henning, T. 2005, A&A, 437, 861

Schmitt, H. R., Antonucci, R. R. J., Ulvestad, J. S., Kinney, A. L., Clarke, C. J., & Pringle, J. E. 2001, ApJ, 555, 663

Schweitzer, M., Lutz, D., Sturm, E., Contursi, A., Tacconi, L. J., Lehnert, M. D., Dasyra, K. M., Genzel, R., Veilleux, S., Rupke, D., Kim, D.-C., Baker, A. J., Netzer, H., Sternberg, A., Mazzarella, J., & Lord, S. 2006, ApJ, 649, 79

Scoville, N. Z., Evans, A. S., Thompson, R., Rieke, M., Hines, D. C., Low, F. J., Dinshaw, N., Surace, J. A., & Armus, L. 2000, AJ, 119, 991

Smith, A. M., Hill, R. S., Vrba, F. J., & Timothy, J. G. 1992, ApJ, 391, L81

Smith, J. D. T., Draine, B. T., Dale, D. A., Moustakas, J., Kennicutt, Jr., R. C., Helou, G., Armus, L., Roussel, H., Sheth, K., Bendo, G. J., Buckalew, B. A.,

Calzetti, D., Engelbracht, C. W., Gordon, K. D., Hollenbach, D. J., Li, A., Malhotra, S., Murphy, E. J., & Walter, F. 2007, ApJ, 656, 770

Soifer, B. T., Neugebauer, G., Helou, G., Lonsdale, C. J., Hacking, P., Rice, W., Houck, J. R., Low, F. J., & Rowan-Robinson, M. 1984a, ApJ, 283, L1

Soifer, B. T., Neugebauer, G., Matthews, K., Egami, E., Weinberger, A. J., Ressler, M., Scoville, N. Z., Stolovy, S. R., Condon, J. J., & Becklin, E. E. 2001, AJ, 122, 1213

Soifer, B. T., Rowan-Robinson, M., Houck, J. R., de Jong, T., Neugebauer, G., Aumann, H. H., Beichman, C. A., Boggess, N., Clegg, P. E., Emerson, J. P., Gillett, F. C., Habing, H. J., Hauser, M. G., Low, F. J., Miley, G., & Young, E. 1984b, ApJ, 278, L71

Spoon, H. W. W., Armus, L., Cami, J., Tielens, A. G. G. M., Chiar, J. E., Peeters, E., Keane, J. V., Charmandaris, V., Appleton, P. N., Teplitz, H. I., & Burgdorf, M. J. 2004, ApJS, 154, 184

Spoon, H. W. W., Keane, J. V., Tielens, A. G. G. M., Lutz, D., Moorwood, A. F. M., & Laurent, O. 2002, A&A, 385, 1022

Stecher, T. P. & Donn, B. 1965, ApJ, 142, 1681

Struck, C. 1999, Phys. Rep., 321, 1

Surace, J. A. & Sanders, D. B. 2000, AJ, 120, 604

Taylor, V. A., Jansen, R. A., Windhorst, R. A., Odewahn, S. C., & Hibbard, J. E. 2005, ApJ, 630, 784

Teplitz, H. I., Armus, L., Soifer, B. T., Charmandaris, V., Marshall, J. A., Spoon, H., Lawrence, C., Hao, L., Higdon, S., Wu, Y., Lacy, M., Eisenhardt, P. R., Herter, T., & Houck, J. R. 2006, ApJ, 638, L1

Tielens, A. G. G. M., McKee, C. F., Seab, C. G., & Hollenbach, D. J. 1994, ApJ, 431, 321

Tran, Q. D., Lutz, D., Genzel, R., Rigopoulou, D., Spoon, H. W. W., Sturm, E., Gerin, M., Hines, D. C., Moorwood, A. F. M., Sanders, D. B., Scoville, N., Taniguchi, Y., & Ward, M. 2001, ApJ, 552, 527

Veilleux, S., Goodrich, R. W., & Hill, G. J. 1997, ApJ, 477, 631

Weedman, D. W., Hao, L., Higdon, S. J. U., Devost, D., Wu, Y., Charmandaris, V., Brandl, B., Bass, E., & Houck, J. R. 2005, ApJ, 633, 706

Weingartner, J. C. & Draine, B. T. 2001, ApJ, 548, 296

Werner, M. W., Roellig, T. L., Low, F. J., Rieke, G. H., Rieke, M., Hoffmann, W. F., Young, E., Houck, J. R., Brandl, B., Fazio, G. G., Hora, J. L., Gehrz, R. D., Helou, G., Soifer, B. T., Stauffer, J., Keene, J., Eisenhardt, P., Gallagher, D., Gautier, T. N., Irace, W., Lawrence, C. R., Simmons, L., Van Cleve, J. E., Jura, M., Wright, E. L., & Cruikshank, D. P. 2004, ApJS, 154, 1

Wickramasinghe, N. C. & Guillaume, C. 1965, Nature, 207, 366

Wright, G. S., James, P. A., Joseph, R. D., & McLean, I. S. 1990, Nature, 344, 417

Wu, Y., Charmandaris, V., Hao, L., Brandl, B. R., Bernard-Salas, J., Spoon, H. W. W., & Houck, J. R. 2006, ApJ, 639, 157

Yan, L., Chary, R., Armus, L., Teplitz, H., Helou, G., Frayer, D., Fadda, D., Surace, J., & Choi, P. 2005, ApJ, 628, 604